Bottle Micro-Resonator Engineering with Surface Nanoscale Axial Photonics

VICTOR VASSILIEV

Doctor of Philosophy

ASTON UNIVERSITY

November 2023

To Victor Vassiliev, my grandfather and the first among many who inspired me to pursue the study of physics, I dedicate this work with gratitude and admiration.

"Light is a symbol of hope and guidance, and the beauty of its presence can be found in the midst of the darkest of times."

— Martin Luther King Jr.

Acknowledgements

When the goal is quite literally to catch light~~ning~~ in a bottle, the magnitude of the challenge can be overwhelming. However, with the tireless support of inspiring mentors, colleagues, friends, and family, even the most intimidating of tasks can be overcome. Here I would like to thank the remarkable people who illuminated my path, encouraged me to push the boundaries of knowledge and made the process so rewarding.

I would like to begin by extending my sincerest thanks and deepest appreciation to my supervisor, Prof. Misha Sumetsky, for his persistent guidance, reassurance, and belief in my abilities. His expertise, enthusiasm, and commitment to my growth as a researcher have been invaluable in helping me navigate this complex and fascinating field.

I am profoundly grateful to the members of my research team, Sajid Zaki, Dr Yong Yang, Dr Manuel Crespo, Dr Nikita Toropov, Dr Gabriella Gardosi and Dr Kirill Tokmakov, for their camaraderie, collaboration, and dedication. Their insights, feedback, and unique perspectives have enriched my understanding of the subject matter and contributed significantly to my development as a scientist.

My sincere thanks go to the MOCCA consortium for enabling this doctorate, in particular Prof. Sergei Turitsyn, Prof. Sergey Sergeyev, Nataliia Manuilovich and Aston University, Dr Stephan Suckow, Nour Negm and AMO GmbH, Dr Alfredo De Rossi, Dr Fabrice Raineri and C2N-CNRS, Prof. Stefan Wabnitz and Sapienza University and of course my fellow Early-Stage Researchers: Avinash Kumar, Loredana Massaro and Francesco Talenti for their collaboration, constructive criticism, and valuable suggestions. Their expertise and input have greatly enhanced my research quality and helped me delve deeper into the intricate world

of photonics.

I deeply appreciate the friendship and support of my fellow graduate students, Karina, Marta, Daniel, Anastasia, Paulami, Igor, Vlad, Marie, Alex, Eugene, Nasir, Juan Marcello and Dmitrii. Their companionship has made the long hours in the lab more enjoyable, and their shared experiences have provided a sense of community throughout this journey.

I cannot express enough gratitude to my loving family and friends, Luba, Ivan, Inna, Marta, Elisa, Daniel, Carmen, Nelson, Monse, Lucas, Alexandre, Vlad, Pablo and Oleg, for their unwavering support, understanding, and encouragement. Their confidence in me has been my guiding light, and their love has given me the strength to persevere through the most challenging moments.

Lastly, I thank European Union's Horizon 2020 Research and Innovation Programme under the Marie Skłodowska-Curie Actions for providing the financial support and resources necessary to undertake this research.

My work has been made possible by the collective effort of these incredible individuals. I am forever grateful for their contributions to my personal and professional growth during this unforgettable chapter of my life.

Declaration

I, Victor Vassiliev, declare that this thesis, entitled "Bottle Micro-Resonator Engineering with Surface Nanoscale Axial Photonics" is a product of my original research, conducted under the supervision of Prof. Misha Sumetsky at the Institute of Photonic Technologies, Aston University. I affirm that no part of this thesis has been submitted for a degree or any other qualification at this or any other university.

All sources of information and materials used in the research and writing of this thesis have been duly acknowledged and referenced. Any collaborative work conducted during this research has been clearly indicated, and I have provided full acknowledgement of the contributions made by my collaborators.

Furthermore, I confirm that any experiments and investigations conducted during this research have adhered to the ethical guidelines and safety protocols established by Aston University and the broader scientific community. All procedures involving equipment, materials, and data use have been carried out with the proper authorisation and in compliance with relevant regulations.

Lastly, I declare that the copyright for this thesis is held by the author, and that any quotation from this thesis or information obtained from it cannot be published without appropriate acknowledgment and the author's prior written permission.

Signature	*Date*

Abstract

Bottle Micro-Resonator Engineering with Surface Nanoscale Axial Photonics

Whispering gallery mode (WGM) micro-resonators have attracted significant attention in recent years due to their diverse applications in sensing, optical communications, and frequency comb generation. The Surface Nanoscale Axial Photonics (SNAP) platform has risen as a notable technique for creating photonic structures with ultra-low loss, characterized by extraordinary precision to the tune of 0.1 angstroms. This thesis presents two novel and complementary approaches for fabricating WGM-based bottle micro-resonators.

The first approach involves a permanent deformation method, wherein SNAP micro-resonators are fabricated using a heat treatment process with a butane flame. The second approach introduces a reversible deformation technique based on elastic bending, offering tunability and adaptability for various applications. The non-disruptive nature of this second method allows for its integration with other fabrication techniques. Both methods provide angstrom-precise control over fabrication, resulting in stable and high-quality bottle resonators.

We thoroughly investigate and experimentally validate these fabrication approaches, demonstrating high fabrication precision and quality factors. A comparison of the advantages and limitations of each method contributes to a deeper understanding of SNAP-based micro-resonator fabrication and paves the way for future advancements in the rapidly evolving field of photonics.

Keywords— Photonics - Bottle resonator - Tunability

List of Figures

List of Tables

List of Abbreviations

1D ..... One Dimension

2D ..... Two Dimensions

AFM ..... Atomic Force Microscopy

CO_2 ..... Carbon Dioxide

CW ..... Cutoff wavelength

ERV ..... Effective radius variation

FSR ..... Free Spectral Range

FWHM ..... Full Width Half Maximum

HF ..... Hydrofluoric Acid

MF ..... Micro Fiber

OSA ..... Optical Spectrum Analyzer

Q ..... Quality Factor

SMF ..... Single Mode Fiber

SMR ..... SNAP microresonator

SNAP ..... Surface Nanoscale Axial Photonics

TF ..... Tapered Fiber

WGM ..... Whispering Gallery Modes

List of Publications

The following list represents the scholarly contributions made during my doctoral research, including publications and collaborations. While each entry has contributed to my academic and research development, not all have directly influenced the outcomes presented in this thesis:

Journal Articles

1. **Victor Vassiliev**, Michael Sumetsky. (2023). High Q-factor reconfigurable microresonators induced in side-coupled optical fibres. *Light: Science & Applications*. 12, 197.

2. Michael Sumetsky, **Victor Vassiliev**. (2022). Angstrom-precise fabrication of surface nanoscale axial photonics (SNAP) microresonators with a flame. *Laser Physics Letters*. 19, 056202. DOI 10.1088/1612-202X/ac61d4

3. V. Gordienko, Á.D. Szabó, M.F.C. Stephens, **Victor Vassiliev**, C.B. Gaur, N.J. Doran. (2021). Limits of broadband fiber optic parametric devices due to stimulated Brillouin scattering. *Optical Fiber Technology*, 66, 102646. https://doi.org/10.1016/j.yofte.2021.102646

Conference Presentations

1. **Victor Vassiliev**, Michael Sumetsky. Reconfigurable microresonators created by touching straight and bent optical fibers. In: *2023 Conference on Lasers and Electro-Optics (CLEO)*. San Jose, CA, USA, 07-12 May 2023.

Table of Contents

1 | Introduction

1.1 Motivation

Why photonics?

In our ever-evolving world of discovery and progress, we have come to expect technologies to be outpaced by their cheaper, faster and more efficient successors. Yet, photonics stands to shatter this paradigm, leveraging the unchallenged speed of nature's most fundamental currency for exchanging energy and information: the photon. As the science of generating, manipulating, and detecting light, the applications of photonics permeate every facet of our lives, spanning from commonplace experiences to the most cutting-edge scientific research. From agriculture to art analysis, from communications and computing to sensing and medicine, the applications of photonics are already everywhere, awaiting advancements in standardisation and fabrication to unlock their true potential as the final frontier of innovation.

Three main obstacles are often cited to be holding back the photonics industry:

- Integration and miniaturisation: Combining photonic parts with electronic systems and compact devices continues to be difficult. This requires innovative approaches to design, fabrication, and packaging.

- Efficiency and power consumption: Photonic devices, especially those involving active components like lasers, often have high power consumption and low energy efficiency. Improving these factors would lead to more competitive and environmentally friendly devices.

- Material limitations: The choice of materials used in photonic devices can im-

pact their performance, cost, and scalability. Developing new materials and optimising existing ones to overcome these limitations is an ongoing challenge.

A solution ?

To address these issues, whispering gallery mode (WGM) micro-resonators have emerged as a prominent area of research within photonics due to their unique properties and diverse applications. WGM micro-resonators stand out by their ability to confine light along the circumference of a dielectric structure, resulting in low loss and high-quality factor resonances. These properties make WGM micro-resonators highly attractive for various applications, such as frequency comb generation, a key technology for optical frequency metrology, spectroscopy, and ultrafast signal processing. Proposed in 2011, a SNAP resonator works by confining light within a cylindrically symmetric dielectric structure through an effective radius variation (ERV) which is determined by multiplying the structure's radius with the material's refractive index

$$\text{reff}(z) = r(z)n(z) \tag{1.1}$$

where r represents the structure's radius and n denotes its refractive index.
The ERVs required for efficient optical confinement are typically on the scale of tens of nanometers and can be introduced by altering either the radius or refractive index.

The straightforward fabrication requirements and the ultra-low losses make SNAP highly competitive.

Table 1.1: Photonics platforms comparison

Platform	**Illustration**	**Loss**	**Precision**	**Footprint**
Photonic crystals	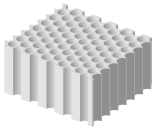	0.01 dB/cm	10 nm	1 μm
Planar photonics	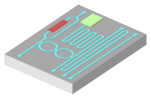	0.1 dB/cm	10 nm	100 μm
Micro resonators		0.0001 dB/cm	100 nm	10 μm
SNAP	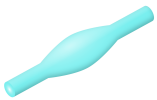	0.0001 dB/cm	0.1 nm	10 μm

Why bottle resonators ?

Bottle micro-resonators, a specific type of WGM micro-resonator, have gained considerable interest because they offer unique advantages over other micro-resonator geometries. Their axial light confinement allows for highly sensitive and selective mode coupling, essential for frequency comb generation and sensing applications. However, the fabrication of high-quality bottle micro-resonators with the required precision and control remains a challenge, necessitating the development of advanced fabrication methods.

fabrication challenge

The Surface Nanoscale Axial Photonics (SNAP) platform has emerged as a promising solution. SNAP allows for the creation of ultralow loss photonic structures with unprecedented precision on the order of 0.1 angstroms. The platform relies

on the precise manipulation of the axial geometry of optical fibres, enabling the fabrication of micro-resonators with exceptional performance characteristics. By harnessing the potential of the SNAP platform, researchers can push the boundaries of micro-resonator engineering and unlock new possibilities in photonics applications.

Our solution

We present two novel fabrication methods for WGM-based bottle micro-resonators using the SNAP platform. The first approach involves a permanent deformation method, where SNAP micro-resonators are fabricated through a heat treatment process using a butane flame. The second approach introduces a reversible deformation based on elastic bending providing tunability and adaptability. The non-destructive nature of this method enables its use in combination with other fabrication techniques, further expanding the potential of SNAP-based micro-resonator engineering. Both ways create stable, high-quality bottle resonators with Angstrom-precise control over fabrication processes.

What impact ?

The development and investigation of these two fabrication methods represent a significant contribution to the field of photonics and pave the way for future advancements in the rapidly evolving domain of micro-resonator technology. By exploring the capabilities of the SNAP platform for bottle micro-resonator fabrication, this research aims to advance our understanding of WGM micro-resonator engineering and expand the potential applications of these versatile devices in sensing, optical communications, and photonic devices.

1.2 Aim and Objectives

This thesis aims to establish a framework for fabricating WGM-based bottle micro-resonators using the SNAP platform. The specific objectives are:

a. Develop a permanent deformation method for fabricating SNAP micro-resonators using a heat treatment process with a butane flame.

b. Introduce a reversible deformation technique based on elastic bending for tunability and adaptability in various applications.

c. Investigate both fabrication methods' advantages, limitations, and potential applications.

d. Advance our understanding of WGM micro-resonator engineering and expand the potential applications of these versatile devices in sensing, optical communications, and photonic devices.

1.3 Thesis Outline

This thesis explores innovative fabrication techniques within Surface Nanoscale Axial Photonics (SNAP) for engineering high-precision Whispering Gallery Mode (WGM) micro-resonators, offering significant advancements for photonics applications. The thesis is organized as follows:

Chapter 1 — Introduction

This chapter provides an overview of photonics, WGM micro-resonators, and the motivation behind the research. The aim and objectives of the thesis are also presented.

Chapter 2 — SNAP Platform

This chapter provides a comprehensive overview of the Surface Nanoscale Axial Photonics (SNAP) platform, detailing its foundational principles, including total internal reflection, evanescent fields, and frustrated total internal reflection. It introduces SNAP resonators, emphasizing their significance in photonics, and elaborates on the methods and theoretical underpinnings necessary for SNAP device fabrication and characterization.

Chapter 3 — Method 1 - Thermal Sculpting

The focus is on a novel method for fabricating whispering gallery mode (WGM) micro-resonators using thermal sculpting. This approach employs heat treatment to induce permanent deformation in SNAP micro-resonators, highlighting the precision and quality achieved in resonator construction. The chapter outlines the experimental setup, fabrication processes, and characterizes the resonators, discussing the implications of this method on the field of photonics.

Chapter 4 — Method 2 - Side-coupled Optical Fibres

This chapter introduces a second innovative fabrication technique using side-coupled optical fibers for reversible deformation, offering tunability and adaptability in various applications. It covers the significance of this method, experimental results, and provides a thorough comparison with existing techniques, demonstrating the advantages of side-coupled fibers in the fabrication of SNAP devices.

Chapter 5 — Conclusions

The concluding chapter summarizes the achievements and methodologies presented in the thesis, discusses significant discoveries, and outlines future directions in SNAP fabrication techniques. It explores the potential applications of WGM micro-resonators in sensing, optical communications, and highlights the impact of novel fabrication techniques on the field of photonics.

2 | SNAP platform

This chapter presents the SNAP platform and the required concepts for the experimental studies and findings discussed in subsequent chapters. After a concise introduction to the fundamental principles of evanescent coupling, the WGM resonators and how the platform combines the two, we delve into the theoretical aspects of light propagation in cylindrical step-profile structures, drawing parallels to Quantum Mechanics, and elaborate on light behaviour within SNAP resonators and prevalent fabrication techniques. Lastly, we touch upon SNAP spectrograms, an efficient data display method in SNAP.

2.1 TIR-related effects in SNAP

People are often familiar with total internal reflection (TIR) as an essential phenomenon for guiding waves. Yet, there's more to it, with related phenomena that are just as important. More than just intriguing theory, these phenomena sit at the core of the Surface Nanoscale Axial Photonics (SNAP) platform and play a critical role in my research. In particular, the concept of frustrated TIR and the evanescent field. They are essential tools in our understanding and application of light within SNAP.

2.1.1 Total internal reflection

Total Internal Reflection (TIR) plays a vital role in optical fibres and resonators. In optical fibres, it allows light to be confined within the fibre core, effectively guiding it along the fibre's length while minimising attenuation. For resonators, TIR is crucial for sustaining high-quality resonances. When light is trapped within resonant cavities, such as in whispering gallery mode (WGM) microresonators, it

ensures that the light circulates multiple times within the cavity. TIR is a special case of the law of refraction.

$$\frac{\sin(\theta_1)}{\sin(\theta_2)} = \frac{v_1}{v_2} = \frac{n_2}{n_1} \tag{2.1}$$

Total reflection occurs when a wave passes to a medium that allows a higher phase velocity v_2. As per the law, the beam is expected to refract at an angle θ_2 larger than its incident angle, θ_1. Consequently, for a range of incident angles exceeding a critical angle θ_c, the beam would have to refract at an angle greater than $90°$.

$$\theta_c = \arcsin(\frac{n_1}{n_2}) \tag{2.2}$$

In such a scenario, refraction does not occur, and the partial reflection at the interface of the two mediums becomes total. In standard optical fibres, light is guided along the fibre's axis via total internal reflection at the core-cladding interface. This is made possible by a higher refractive index of the core than the cladding, which confines the light within the core and facilitates its propagation over large distances with minimal loss.

In contrast, the SNAP platform employs a significantly different approach. Here, light travels within the cladding of the fibre, tracing a circular path thanks to total internal reflection at the cladding-air interface. This unique light path, unlike the linear one in traditional fibres, gives rise to a standing wave pattern known as a Whispering Gallery Mode (WGM). We discuss the SNAP setup and its unique opportunities for photonics applications later in this dissertation.

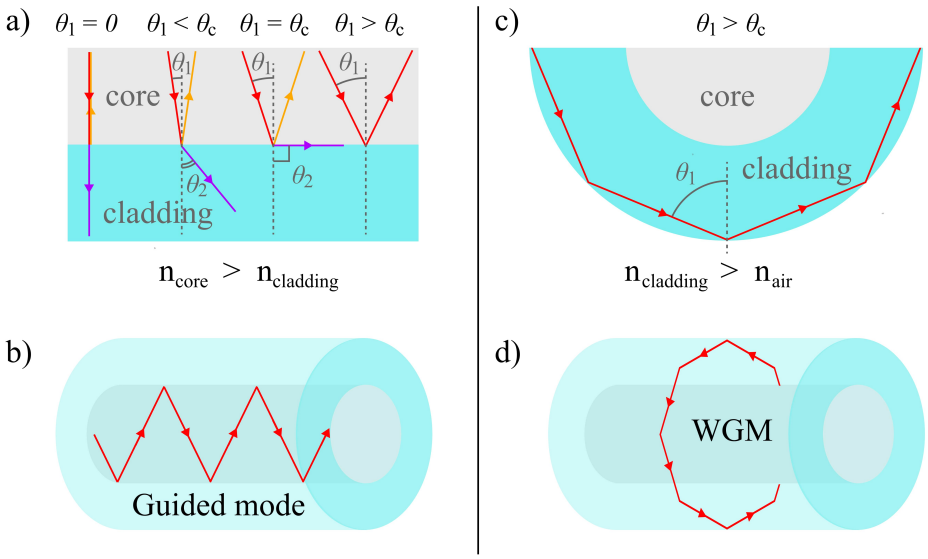

Figure 2.1: **(a)** The reflection and refraction at the interface between a high refractive index core and a lower refractive index cladding. Four distinct incident angles θ are shown. **(b)** Light beam's propagation within the core of an optical fibre, undergoing a series of TIR events as it travels along the fibre. **(c)** Cross-sectional view of an optical fibre with the light beam circulating around the cladding-air interface. As the beam encounters the cladding-air interface with an even lower refractive index, it experiences TIR, resulting in the formation of WGMs. **(d)** Alternative perspective of the WGMs within the optical fibre in **(c)**.

2.1.2 Evanescent field

Although total internal reflection implies no continuous power flow across the interface between the two media, an evanescent wave is carried by the external medium, traveling along the interface with an amplitude that decreases exponentially as it moves away from the interface.

This possibly prompts questions regarding the distribution of energy among the incident beam, reflected beam, and evanescent waves present in the region beyond the interface. If all the light undergoes reflection at the interface, what energy source forms the electromagnetic fields in the region immediately adjacent

to it? To address this, one must distinguish between two states of the system: the transient state and the steady state. The transient state arises immediately after the initiation of the light source. During this phase, a portion of the incident energy contributes to the formation of the evanescent waves, which are established promptly and persist as long as the system remains undisturbed.

Subsequently, the system enters the steady state, where the waves have fully propagated. In this state, if we were to calculate the perpendicular component of the Poynting vector for the evanescent field, we would observe that the electric and magnetic components are out of phase by 90 degrees. This phase difference results in zero energy being carried away from the interface by the evanescent waves.

In the context of the Surface Nanoscale Axial Photonics (SNAP) platform, both the launch and sensing of light within the resonator are achieved through evanescent coupling, a mechanism that prominently features the evanescent field. This field is generated when a tapered fibre, a fibre whose diameter has been strategically reduced, is connected to a light source. The tapered design enables the establishment of an evanescent field, an electromagnetic field that decays exponentially with distance from the fibre's surface. This field envelopes the tapered region of the fibre and plays an instrumental role in the evanescent coupling process, providing the necessary medium for light interaction. Thus, in the SNAP platform, the evanescent field is not merely a byproduct of TIR; rather, it forms the backbone of the system's light manipulation capabilities, paving the way for sophisticated photonics applications.

The tapering technique is quite simple for a standard 125um commercial optical fibre. This process involves applying heat to an uncoated section of an optical fibre, typically raising the temperature to around 1400 degrees Celsius. This application of heat renders the fibre malleable and primed for shaping. Following the

heating phase, force is gently applied to each end of the fibre, inducing a gradual tapering.

As the fibre is drawn out and its diameter decreases, a narrowed 'waist' forms. This tapered region has both core and cladding considerably thinner than the original fibre and can now facilitate the evanescent field, setting the stage for effective evanescent coupling. The precise control over the tapering process allows us to tailor the properties of the evanescent field, and by extension, the performance of the SNAP platform, to specific applications.

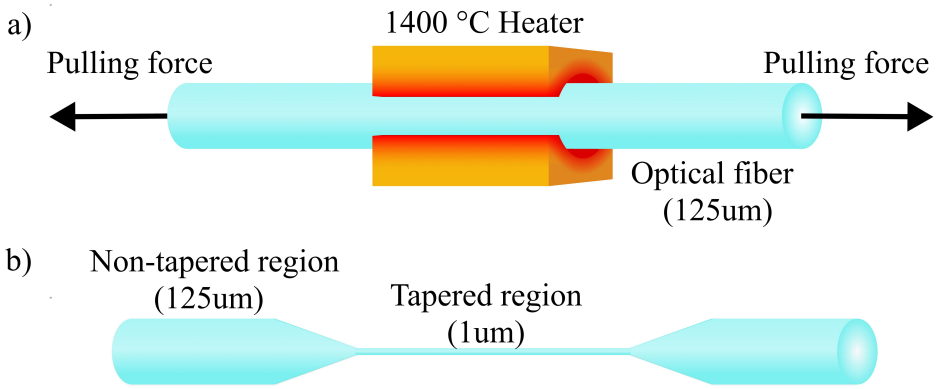

Figure 2.2: Tapering process and outcome. **(a)** Depicts the tapering process, where a compact fibre furnace is utilized to heat a specific portion of the optical fibre, rendering it malleable. Force is applied to either end of the fibre to instigate gradual tapering. **(b)** Displays the result of the tapering process: a fibre featuring a distinct tapered region, the critical site for generating and maintaining the evanescent field.

In a tapered optical fiber, the evanescent field originates from the principles of total internal reflection and changes in optical waveguide modes. Light introduced into the fiber propagates within the core due to the refractive index difference between the core and the cladding. As the fiber tapers, decreasing the diameter of both the core and cladding, guided light modes can extend into the cladding, forming an evanescent wave that decays exponentially with distance from the fiber surface.

This phenomenon, determined by taper geometry and refractive index contrasts, creates an evanescent field sensitive to changes in the surrounding medium's refractive index, a characteristic exploited in various applications such as refractive index sensors and optical tweezers.

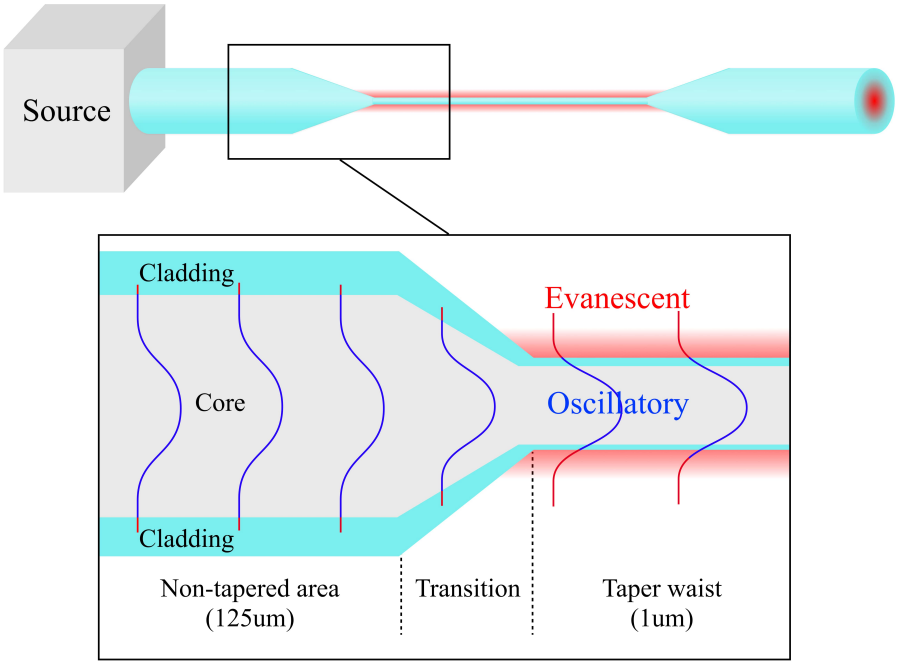

Figure 2.3: Evanescent Field in a Tapered Fibre. The figure provides a cross-sectional depiction of a tapered optical fibre. The oscillatory light modes within the fibre core and cladding are visible, illustrating how these guided modes extend to form an evanescent field around the taper. This evanescent field, represented in red, decays exponentially beyond the fibre boundary, this results from the wave nature of light and the changing refractive index contrast from core to cladding and surrounding medium.

2.1.3 Frustrated TIR

Total reflection is indeed complete if the external medium is lossless, continuous, and infinitely extensive; however, it can be noticeably less than total if the evanescent wave is absorbed by a lossy external medium or redirected by the external

medium's outer boundary or objects within it.

Frustrated Total Internal Reflection (FTIR) is a phenomenon that occurs when a wave travelling in a medium encounters a boundary with a second medium of lower refractive index, and a third medium with higher refractive index is placed very close to the boundary.

In typical Total Internal Reflection (TIR), if the angle of incidence of light exceeds the critical angle (determined by the refractive indices of the two media), the light is completely reflected back into the first medium, with an evanescent wave present at the boundary. However, when a third medium with a higher refractive index is brought close to this boundary (within the range of the evanescent wave), the "total" internal reflection can become "frustrated."

The evanescent wave, which usually decays rapidly with distance from the boundary, can now "tunnel" into the third medium. This phenomenon is called "tunneling" because the light seems to bypass or tunnel through the second medium (the barrier) into the third medium. This is akin to some of the energy "leaking" into the third medium, which is usually observed as a transmitted beam in that medium.

FTIR is a critical principle behind many technologies, including certain types of sensors, thin-film optics, and even some touch-screen technologies.

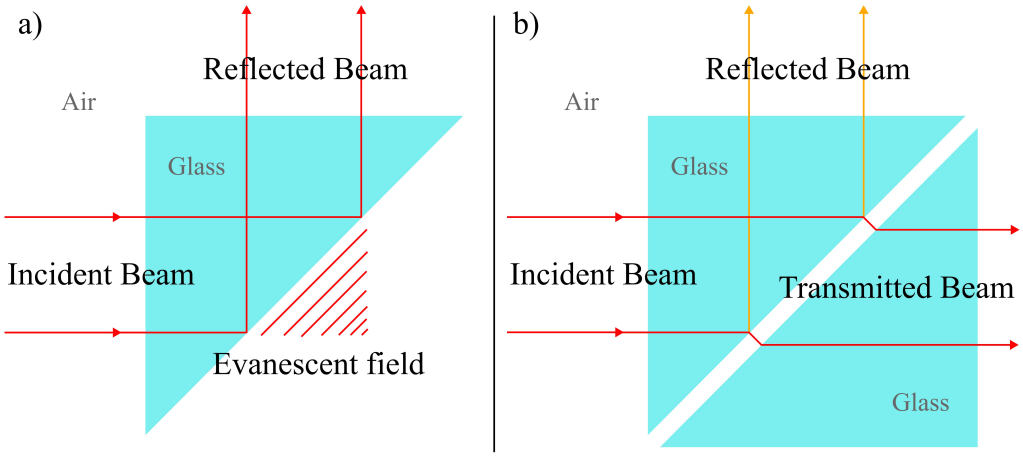

Figure 2.4: **(a)** Illustrates total internal reflection (TIR) within a prism, where an incident light ray is fully internally reflected due to its angle of incidence.**(b)** Depicts frustrated TIR in the presence of a second prism. Instead of complete reflection, some light tunnels into the adjacent prism, disrupting the typical TIR behavior.

In a distinct scenario of frustrated TIR, one doesn't merely observe diminished reflection but rather a complete absence of it. This phenomenon hinges on two factors: the precise distance between the prisms and the frequency of the incoming light. Let's consider a textbook example of this phenomenon. Glass hemispheres have replaced the prisms to let the angle of incidence vary. The width Δ of the air gap is also variable.

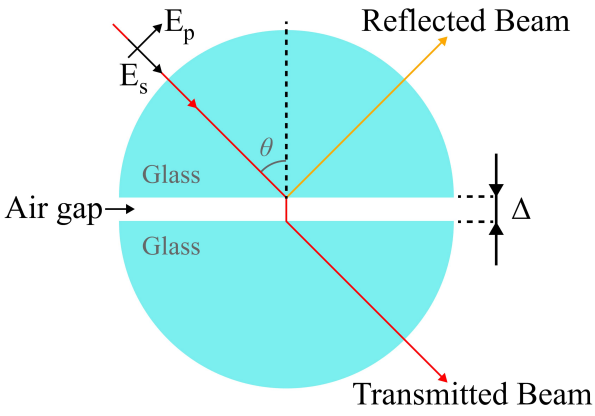

Figure 2.5: Two glass hemispheres with an intervening air space can serve as a model to illustrate frustrated TIR. A consistent light beam targets the top hemisphere's center at an angle θ. The distance Δ of this air gap can be modified.

In the figure, the distinctions between s and p polarizations are crucial. The reflection coefficients for these polarizations differ, especially near Brewster's angle where p-polarized light shows no reflection, unlike s-polarized. Additionally, during total internal reflection, their phase changes vary. This discrepancy is particularly significant near critical angles and in studies like interferometry and evanescent waves. Thus, distinguishing them offers a clearer picture of the underlying optics.

The subsequent figure presents calculated graphs comparing amplitude reflection coefficients $|r_p|$ and $|r_s|$ against the angle of incidence θ, considering three separate values of Δ.

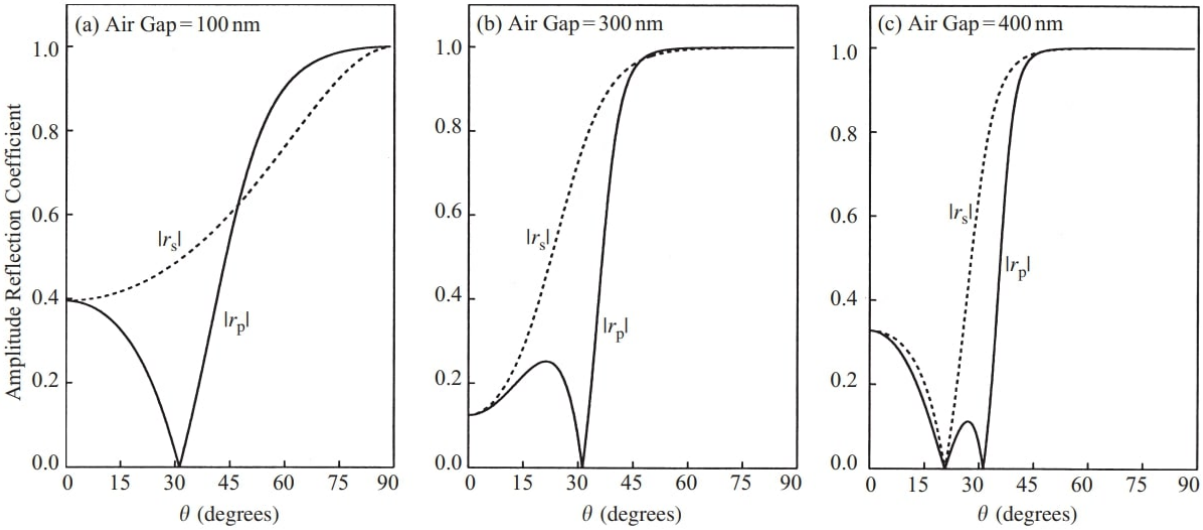

Figure 2.6: The figure displays calculated amplitude reflection coefficients, $|r_p|$ and $|r_s|$, corresponding to p- and s-polarized illumination within the setup shown in Figure 27.5. The hemispheres possess a refractive index n = 1.65. The employed beam has a wavelength λ= 650 nm, and the air gap widths are set at **(a)** 100 nm, **(b)** 300 nm, and **(c)** 400 nm. Courtesy of [1]

For the given values of Δ at 100 and 300, the reflection coefficient's change with θ is as anticipated. With the perpendicular polarization, the reflection gradually rises as the angle of incidence increases. The parallel polarization shows a similar pattern, but notably, there's no reflection around Brewster's angle.

However for Δ set at 400, there's a stark contrast from the expected smooth change. Notably, when θ is 20.7, both rp and rs drop to zero. This anomaly is the special case of frustrated TIR we are interested in, when the thickness of a transparent layer coincides exactly with an integer multiple of half the light's wavelength, its influence on the interplay of multiple beams is neutralized, essentially rendering the layer non-contributive to the optical behavior.

Frustrated Total Internal Reflection (TIR) plays a pivotal role in manipulating light propagation. The SNAP platform uses it to channel light from a tapered fiber directly into its resonators, enhancing the overall efficiency of the setup.

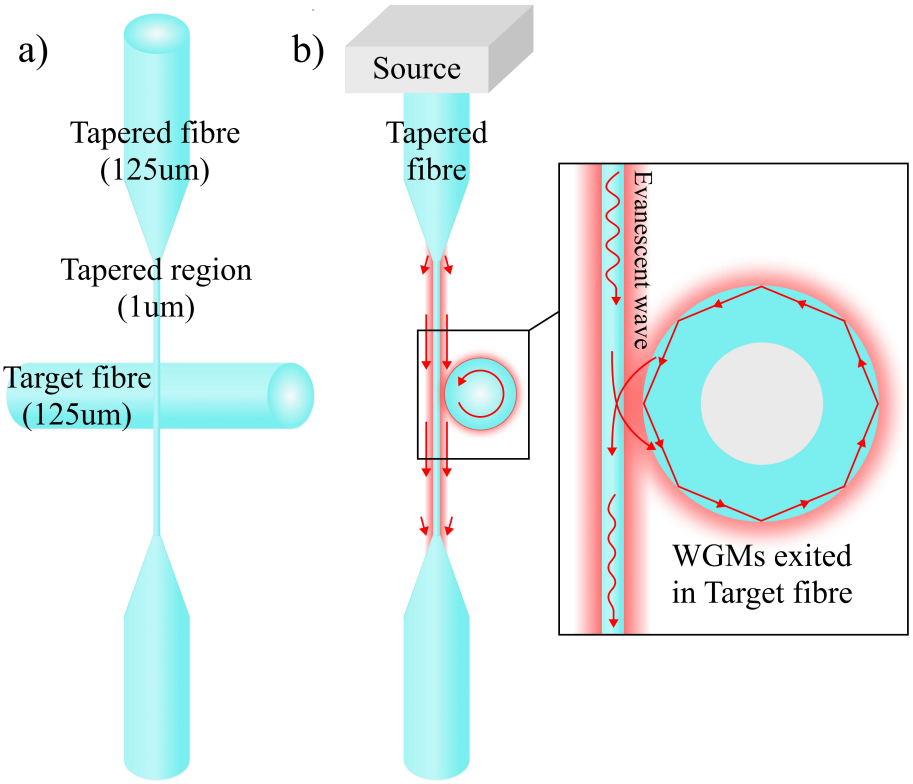

Figure 2.7: **(a)** Side view of a tapered fiber aligned to excite whispering gallery modes in an untapered fiber. **(b)** Front view of the same arrangement where the tapered fiber is now connected to a light source. The trajectory of the light is illustrated with red arrows, indicating its path through the system.

2.2 SNAP resonators

So we have created light waves that circulate or "whisper" around the fibre's cylindrical structure's periphery with 125 μm of outer diameter. In this Whispering gallery mode (WGM) the light is largely confined close to the external circumference or boundary of the fiber's cladding.

However, commercial fibers are designed to guide light longitudinally down their length so while there's strong confinement radially due to the cladding-air refractive index difference, there's no inherent mechanism in a straight fiber to confine the light axially. Therefore, the light spreads out along the fiber's axis, potentially diminishing the WGM properties we're trying to explore.

Here's where innovation and technique come into play. To create a resonator effect in a fiber, we must introduce feedback mechanisms to confine the light axially.

2.2.1 Localizing the Light to Form a Resonator

Some natural ideas to restrict light along the axial direction can be:

Loop Resonator: bending the fiber into a loop and coupling light back into the same fiber. If done precisely, this can lead to the formation of a resonant cavity.

External Reflectors: Using external mirrors or other reflective surfaces at specific positions along the fiber can help create a localized resonant cavity.

External Mechanisms: Wrapping the fiber around a dielectric or introducing a medium with a different refractive index around specific sections of the cladding can alter the total internal reflection conditions and can be used to introduce resonances or localize the cladding modes.

Refractive Index Perturbations: Just as with Fiber Bragg Gratings for core modes, introducing periodic refractive index variations in the cladding might be a way to reflect certain wavelengths of WGMs, thereby creating a resonant structure. This is more challenging to implement than standard FBGs.

Following the refractive index variation idea lead to a method that stood out by its implementation simplicity and precision.

2.2.2 Axial localisation by effective radius variation

The resonance conditions of WGMs are intricately tied to the radius of curvature and the refractive index of the medium they propagate through. Consequently, tiny changes in either the radius or the refractive index can lead to significant shifts in the resonance frequencies of these modes. From the perspective of the WGMs, radius variations and refractive index changes can be perceived interchangeably in terms of their effect on the light's propagation conditions.

This has led to conceptualising an "effective radius variation," which combines the individual contributions from radius and refractive index variations. Considering this parameter, one can design and control resonant structures with impressive precision, enabling light confinement axially with effective radius variations on the scale of mere angstroms. This sensitivity highlights the precision and control WGM-based systems offer and underpins their potential for ultra-sensitive sensing and detection applications.

Taking into account the variation of the effective radius with respect to z, the effective refractive index can be expressed as:

$$\Delta r_{\text{eff}}(z) = r_0 n_f(z) + n_{f0} \Delta r(z) \tag{2.3}$$

In typical optical fibres, the light of wavelength λ travels along the fibre's core and the propagation constant for this light is:

$$\beta_0(\lambda) = \frac{2\pi n_{f_0}}{\lambda} \tag{2.4}$$

However, due to this direction of light propagation in SNAP, the axial progression is inherently sluggish ($\beta << \beta_0(\lambda)$) and restricted to the region of the radius

variation.

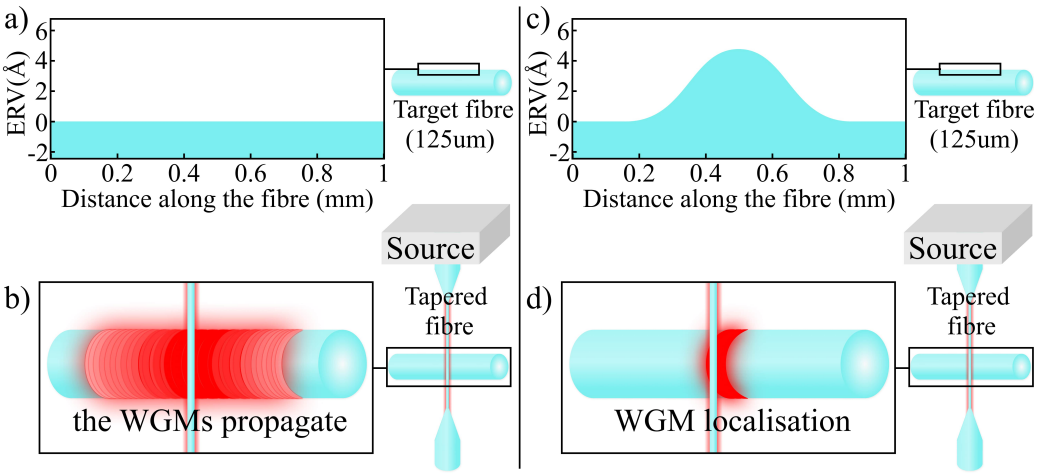

Figure 2.8: Illustration of ERV localisation. On the left, **(a)** provides a side profile of a 125 μm diameter fiber with a perfectly flat surface spanning 1 mm. Directly beneath it, **(b)** illustrates the SNAP setup exciting WGMs in the fiber from **(a)** without any axial localization. **(c)** shows a fiber surface with a distinct effective radius variation structure. Its counterpart, **(d)**, displays the result of this structural change, showing clear axial localization.

2.3 Characterisation in SNAP

In the study of SNAP resonators, it is essential to utilize effective tools for precise characterization. Among these, the SNAP spectrogram stands out as a fundamental instrument. This plot maps the resonant frequencies within a SNAP bottle resonator to specific positions along its primary axis, providing a comprehensive view of the resonator's behaviour. In this section, we will explain how it is built.

2.3.1 Evanescent Spectroscopy

Unlike the example with prisms, achieving efficient coupling between a tapered fiber and a resonator can be challenging and often requires careful experimental

alignment and precise control over the resonator and fiber properties. However, once optimized, this approach offers a powerful method for interrogating and controlling resonator properties. The main parameters for a good evanescent coupling are:

Resonance Condition: An optical resonator can only support specific frequencies of light known as its resonance frequencies. The physical and geometrical properties of the resonator determine these resonance frequencies. If the light launched from the tapered fiber has a frequency matching one of these resonance frequencies, it will couple into the resonator. If not, it will largely continue its path in the fiber.

Phase matching: It coordinates the phase velocities of the modes in the resonator and the tapered fiber for effective evanescent coupling. If the modes are not phase-matched, the efficient coupling will not take place even with the resonance condition respected.

Polarisation Dependence: The modes supported by optical resonators and fibers are typically polarisation-dependent. This means that the orientation of the electric field of the incoming light (i.e., its polarisation) has to match the orientation of the mode it's trying to excite in the resonator. If the polarisation of the incoming light doesn't match the polarisation of any of the resonator's modes, the light won't couple effectively into the resonator.

Spatial Mode Matching: Beyond just the frequency and polarization, the spatial profile (or mode shape) of the light in the tapered fiber must also match the spatial profile of the modes in the resonator. The tapering process can help with this, by allowing for a transformation of the mode profile as it moves down the taper, potentially matching the profile of one of the resonator's modes.

Coupling Strength: The evanescent field of the light in the tapered fiber needs to

overlap with the evanescent field of the resonator modes. This overlap is typically stronger when the tapered fiber is closer to the resonator. If the fiber is too far from the resonator, even light at the correct frequency and polarization might not couple into the resonator efficiently.

External Perturbations: Any external factors that alter the properties of the resonator or the fiber can affect the coupling efficiency. This includes temperature fluctuations, mechanical vibrations, or other environmental factors.

Depending on all these criteria, when light is launched into the tapered fiber, it either couples into the resonator or continues through the tapered fiber. Placing a detector at the output of the tapered fiber provides an invaluable tool for characterizing the interaction between the light and the resonator.

By comparing the source data (input light) with the detector data (output light) with and without coupling to a resonator, one can ascertain the amount of light removed due to coupling into the resonator. This drop in intensity at specific frequencies indicates the resonance frequencies of the resonator. Moreover, by analyzing the polarization state and phase of the output light, one can deduce the resonator's polarization dependence and phase-matching conditions. The linewidth and depth of the resonances give information about the resonator's quality factor (Q-factor) and its internal losses.

Any dynamic changes or shifts in the resonance frequencies can also indicate external perturbations or intrinsic properties of the resonator, such as thermal effects or nonlinear interactions. Thus, a comprehensive understanding of the resonator's properties and interaction with light can be obtained by carefully comparing the source and detector data.

2.3.2 LUNA optical vector analyser

The primary instrument facilitating this characterization technique in my research is the Luna OVA 5100, which integrates a source, detector, and analysis software. It is particularly suitable for the burgeoning fields of silicon photonics and other integrated photonics devices, as it offers both high resolution and rapid device characterization.

The OVA uses an interferometric method, offering thorough analyses with a single scan, allowing for simultaneous loss, polarization, dispersion, phase, and time domain response measurements. This approach facilitates the direct measurement of the linear transfer function, or the Jones Matrix, capturing its four complex elements across every wavelength under examination. Drawing from this rich dataset, the system extracts all standard linear parameter measurements, encompassing Insertion Loss, Return Loss, Group Delay, Chromatic Dispersion, Polarization Mode Dispersion, and Polarization Dependent Loss.

Figure 2.9: An image of the Luna OVA device next to a laptop displaying its analysis software interface.

2.3.3 Insertion Loss

For resonator engineering, Insertion Loss (IL) is the most pivotal parameter measured by the LUNA optical spectrum analyzer, as it directly gives a fundamental benchmark for the resonator's overall performance. It provides insight into the efficiency and quality of light coupling between the input and output of the resonator. By studying the wavelength dependence of the IL, one can discern resonance conditions, mode profiles, and other critical parameters.

Insertion loss refers to the reduction in power intensity (attenuation) of an optical signal when it passes through a device or component in an optical system, such as a coupler, splitter, connector, or any other integrated optical device. It is generally expressed in decibels (dB) and represents the logarithmic ratio between the input power (P_{in}) and the output power (P_{out}) of the device or component. The formula to calculate insertion loss in dB is:

$$IL(dB) = 10 \times \log_{10}\left(\frac{P_{in}}{P_{out}}\right) \tag{2.5}$$

A higher insertion loss indicates that more optical power is lost (or absorbed, scattered, etc.) as the signal traverses the device or component. In fibre optic communications and photonics, it's preferable to have members with low insertion loss to ensure efficient transmission and minimal signal degradation.

In the context of SNAP, peaks in insertion loss adopt a unique significance, providing insights into the resonator's behaviour. Since we monitor the insertion loss of the taper used to launch light inside the resonator, a noticeable dip in intensity at particular frequencies signifies the resonance frequencies of the resonator.

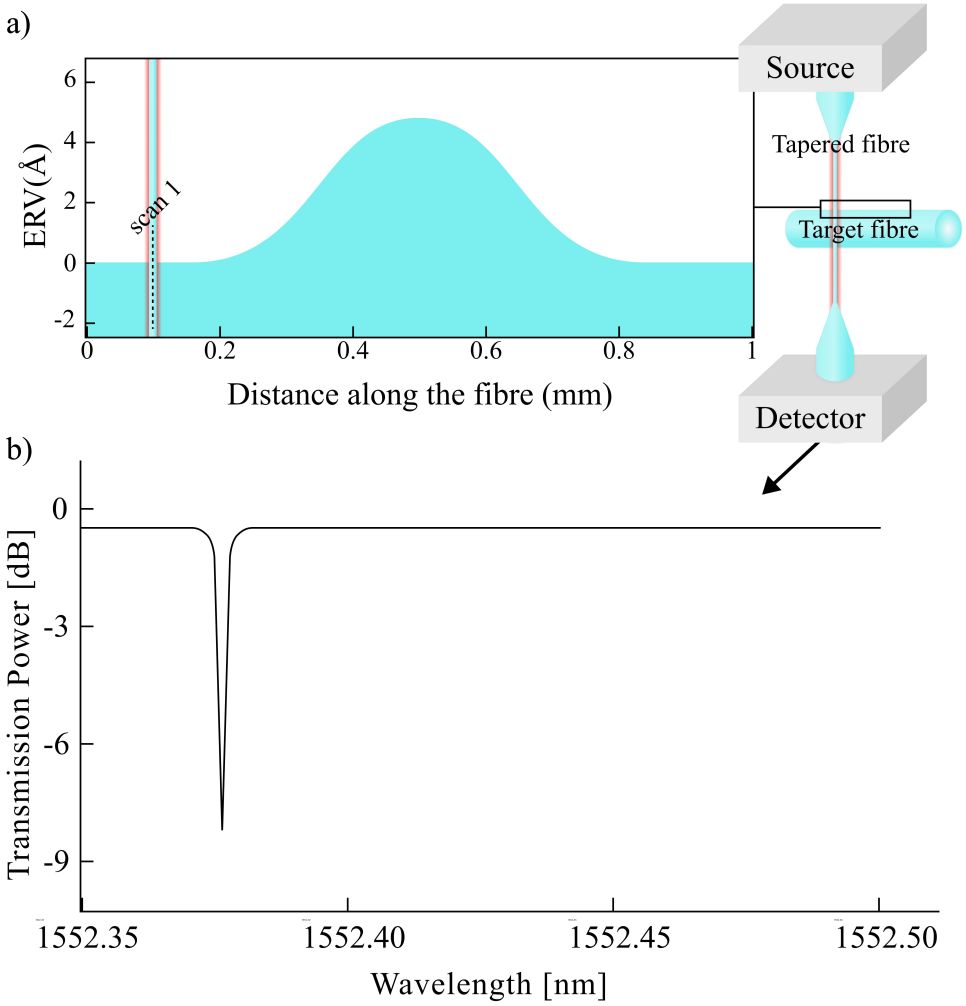

Figure 2.10: SNAP spectroscopy and corresponding Insertion Loss. **(a)** Illustration depicting a SNAP scan with the taper precisely positioned at z = 0.1mm along the fibre axis. **(b)** Insertion loss plot within the wavelength range of 1552.35 nm to 1552.50 nm, corresponding to the taper position shown in **(a)**.

The spike in the insertion loss at 1552.38 nm tells us the resonator's resonance frequency, which relates to a whispering gallery mode. By looking at how wide and deep these spikes are, we can learn about the quality (Q-factor) of the resonator and how much light it might be losing internally.

2.3.3.1 Quality factor

The Q-factor is one of the valuable insights the resonance modes provide in the insertion loss diagram. A resonator's Q-factor, or quality factor, describes how "sharp" or "selective" its resonance is, with a higher Q-factor indicating a sharper resonance. The Q-factor can be determined for optical resonators using a resonance mode's Full Width Half Maximum (FWHM). The formula to derive the Q-factor from the FWHM in wavelength terms is:

$$Q = \frac{\lambda_0}{\Delta\lambda} \tag{2.6}$$

λ_0 is the resonant wavelength. $\Delta\lambda$ is the FWHM of the resonance in wavelength units.

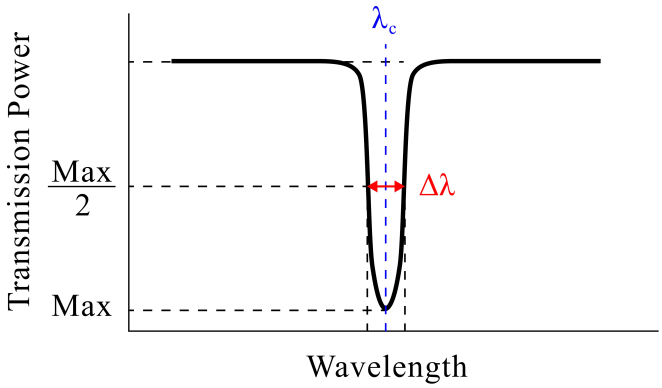

Figure 2.11: Visualization of resonant wavelength and Full Width Half Maximum

In essence, the Q-factor represents the ratio of the resonant frequency to the bandwidth (FWHM) of the resonance. A high Q-factor indicates that the resonance is narrow compared to its central frequency, which typically signifies a low loss in the resonator and a more robust internal field [6].

The Q-factor is directly linked to the mode's decay duration in an optical resonance system. This duration is inversely associated with external and internal loss rates [7]. External losses arise from light being coupled out:

$$Q_{\text{ext}} = \frac{2\pi N}{K} \tag{2.7}$$

K is the coupling coefficient, and N is the mode number. When a single-mode waveguide is linked with the microcavity, enhancing the coupling decreases the quality factor [8]. We can write the Q factor as a sum of these components :

$$\frac{1}{Q} = \sum \left(\frac{1}{Q_{\text{int}}} + \frac{1}{Q_{\text{coupling}}} \right) \tag{2.8}$$

The intrinsic Q factor can be decomposed in the following contributions [9]:

$$\frac{1}{Q_{\text{int}}} = \frac{1}{Q_{\text{material}}} + \frac{1}{Q_{\text{radiation}}} + \frac{1}{Q_{\text{scattering}}} + \frac{1}{Q_{\text{contaminant}}} \tag{2.9}$$

Q_{material} is the material loss, $Q_{\text{radiation}}$ the radiation loss, $Q_{\text{scattering}}$ the surface scattering loss, and $Q_{\text{contaminant}}$ the contaminant loss.

Besides Q_{material}, all other Q-factor components can be optimized during fabrication.

Radiation loss is attributed to the internal field curvature of the cavity, but this can be alleviated by enlarging the microcavity. The quality of the surface primarily influences surface scattering loss. Utilizing the surface tension properties of silica optical fibres, the SNAP platform ensures smoother surfaces for the microresonators, thereby minimizing this loss. Contaminant loss stems from the presence of surface impurities or the uptake of contaminants. By crafting microcavities in

ultra-clean settings, this loss can be significantly reduced.

On the other hand, material absorption loss is mainly influenced by the microcavity's refractive index and wavelength [3]:

$$Q_{\text{material}} = \frac{2\pi n}{\alpha\lambda} \tag{2.10}$$

Here, the attenuation coefficient is α, n the refractive index, λ is the resonant wavelength. In this context, choosing a suitable wavelength is more important to reduce the loss and increase the quality factor.

For silica fibres like the one I used, the lowest attenuation is around the 1550 nm wavelength ($4.6 \times 10^{-6} cm^{-1}$ [10]).

2.3.3.2 WGM Spectral Shift

Another valuable information that the insertion loss diagram can provide is related to the spectral shift of the resonant modes. A whispering gallery mode (WGM) resonator exhibits a high degree of sensitivity to changes in its surrounding refractive index and variations in its radius due to its unique ability to trap light along the periphery of a circular structure.

Alterations in the refractive index or the resonator's radius can modify the optical path length for the confined photons. This affects the phase condition required for resonant modes, pivotal for the waves' constructive interference. Consequently, both these changes lead to shifts in the resonant wavelength of the WGM. Specifically, an increase in either the refractive index or the radius generally results in a redshift (toward longer wavelengths), whereas a decrease induces a blueshift (toward shorter wavelengths).

The refractive index and radius influence the spectral position of the WGM [11]:

$$m\lambda = 2\pi r n_{\text{eff}} \tag{2.11}$$

m represents an integer corresponding to the azimuthal quantum number, while λ denotes the resonant wavelength, r is the radius, and n_{eff} is the effective refractive index experienced by the WGMs.

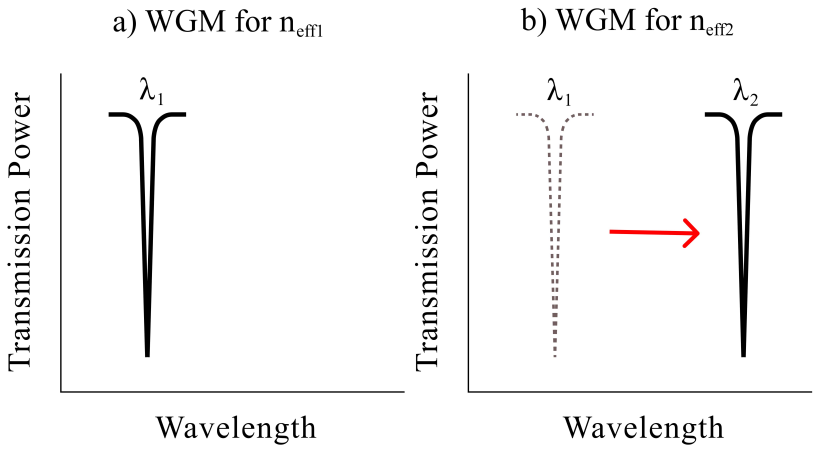

Figure 2.12: **(a)** Resonant wavelength spectral position for n_{eff1}. **(b)** Resonant wavelength following an increase in refractive index to n_{eff2}, exhibiting a redshift relative to **(a)**.

Such shifts make WGM resonators invaluable for sensing applications, where even minuscule environmental changes or specific molecular interactions can be discerned by observing the consequent wavelength shifts, but they also hold significance for designing SNAP microresonators.

By leveraging this sensitivity, one can achieve a meticulously detailed effective refractive index or compelling radius variation profile, which is essential for fine-tuning the resonance properties of these devices.

2.3.3.3 Free spectral range

Lastly, another critical information that can be obtained from the insertion loss diagrams is the Free Spectral Range (FSR) which denotes an optical resonator's frequency difference between two consecutive, same-order resonance peaks λ_m and λ_{m+1}. It represents a complete light round-trip within the resonator.

The Free Spectral Range (FSR) in terms of wavelength for a round-trip optical path length L and refractive index n is given by:

$$FSR_\lambda = \frac{\lambda^2}{nL} \tag{2.12}$$

For a circular resonator, where $L = 2\pi r$, the equation becomes:

$$FSR_\lambda = \frac{\lambda^2}{2\pi nr} \tag{2.13}$$

In terms of frequency, FSR_ν, the formula is:

$$FSR_\nu = \frac{c}{nL} \tag{2.14}$$

Where c is the speed of light.

The FSR's value is dictated by the resonator's size and refractive index, with smaller resonators having a larger FSR. It's a pivotal concept in optical communications, influencing filtering and wavelength division multiplexing.

2.3.4 SNAP spectrograms

SNAP spectrograms represent an advanced step in understanding fiber resonances. These spectrograms reveal the effective radius variation over a specific fibre section by sequentially capturing insertion loss diagrams at consistent intervals along the fiber axis. Additionally, they spotlight the resonant modes of any underlying resonator, allowing for a detailed spatial and spectral analysis of the system. This methodology provides a broad overview and fine-tuned insight into the fibre's characteristics and resonant structures.

While there are more direct methods to obtain a profile of the surface, such as atomic force microscopy (AFM), transmission electron microscopy (TEM), or scanning electron microscopy (SEM), these are technically challenging to implement due to the cylindrical geometry of microfibers. Moreover, these methods don't capture potential changes in the refractive index, which can be crucial for comprehensive characterization.

In this work, our primary focus is on spatial SNAP spectrograms. However, it's worth noting that temporal SNAP spectrograms are also a valuable tool. These temporal spectrograms are derived from insertion loss scans taken at a consistent spatial point but across a set time interval. Such a method holds particular value for sensing applications, allowing real-time monitoring and detection of changes over time.

In practice, a SNAP spectrogram requires three translation stages: one for coupling engagement with the target fibre, another for axial translation along the target, and a third for vertical adjustment on the tapered fibre. I automated these movements using a MATLAB script in our setup, only requiring the scan section length, sample number and scan parameters as inputs (see Appendix).

The following figure illustrates the fifth scan of a series of transmission power scans spaced by $\Delta z = 0.1mm$. The first scan of this series is shown in Figure 2.10. The illustration is qualitative. It highlights a higher concentration of resonant frequencies within the bottle resonator than its exterior shown in the first scan.

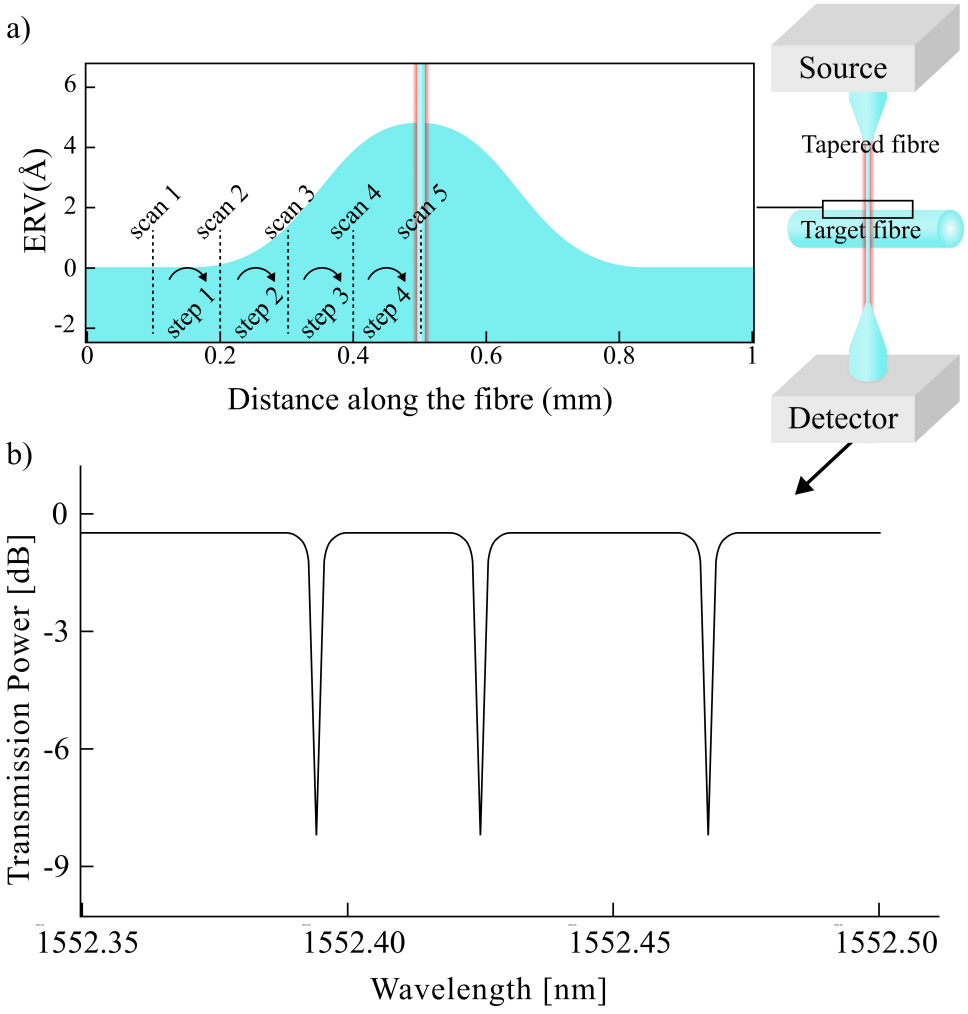

Figure 2.13: **(a)** Illustration depicting a SNAP scan with the taper positioned at z = 0.5mm along the fiber axis. **(b)** Insertion loss plot within the wavelength range of 1552.35 nm to 1552.50 nm, corresponding to the taper position shown in **(a)**.

The upcoming figures provide a visual guide to the construction of SNAP spectrograms. These spectrograms are pieced together from a sequence of transmission power diagrams, mapping out the intricacies of the resonant behaviour within the system.

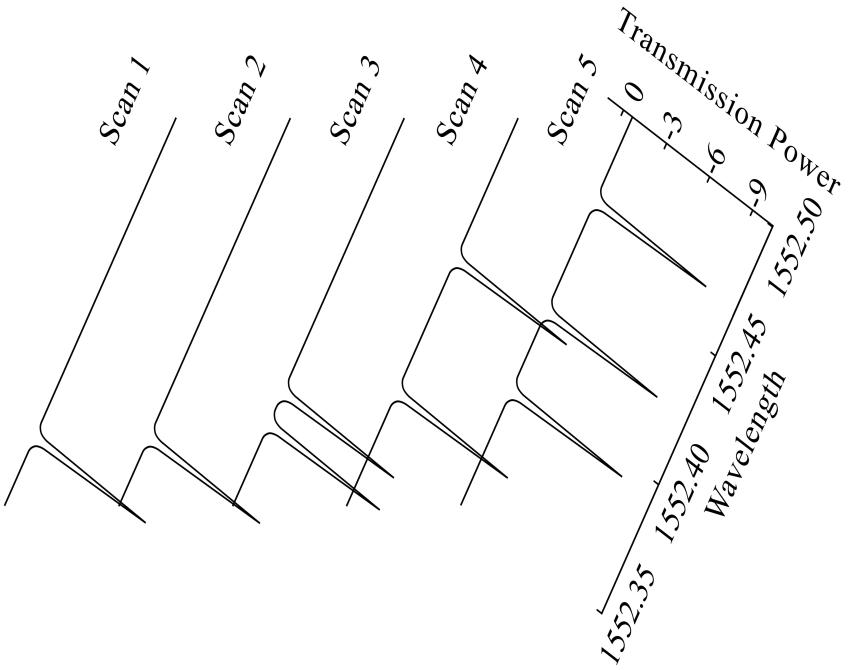

Figure 2.14: The figure provides a visual representation of how the five scans, discussed in figures 2.10 and 2.13, are combined to assemble a spectrogram.

In this depiction, the third dimension introduced by organizing the power transfer diagrams represents the scan number axis, which can be directly correlated to the z position along the fibre axis, given that each scan is consistently separated by the same Δz step.

By enhancing the spatial sampling resolution to 2 μm and visualizing the transfer power through a colorbar representation, we achieve the standard SNAP spectrogram format used for characterizing the resonators explored in this study.

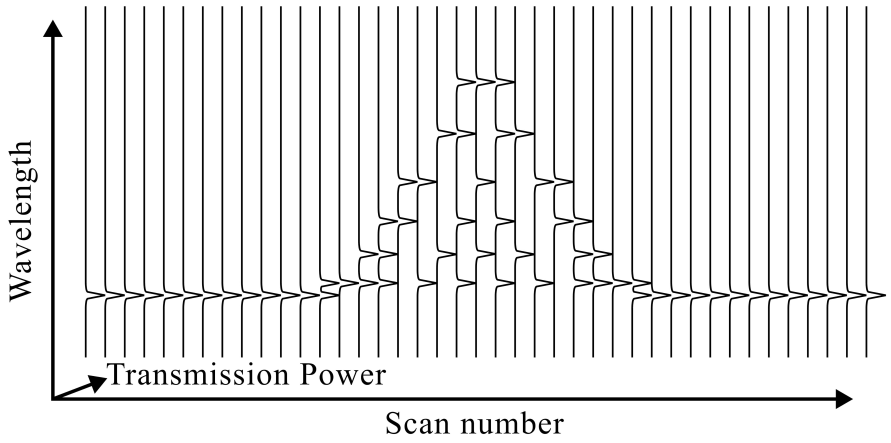

Figure 2.15: SNAP spectrogram in 3D. The spatial resolution of a spectrogram can be enhanced by increasing the number of transmission power samples along the same fibre section.

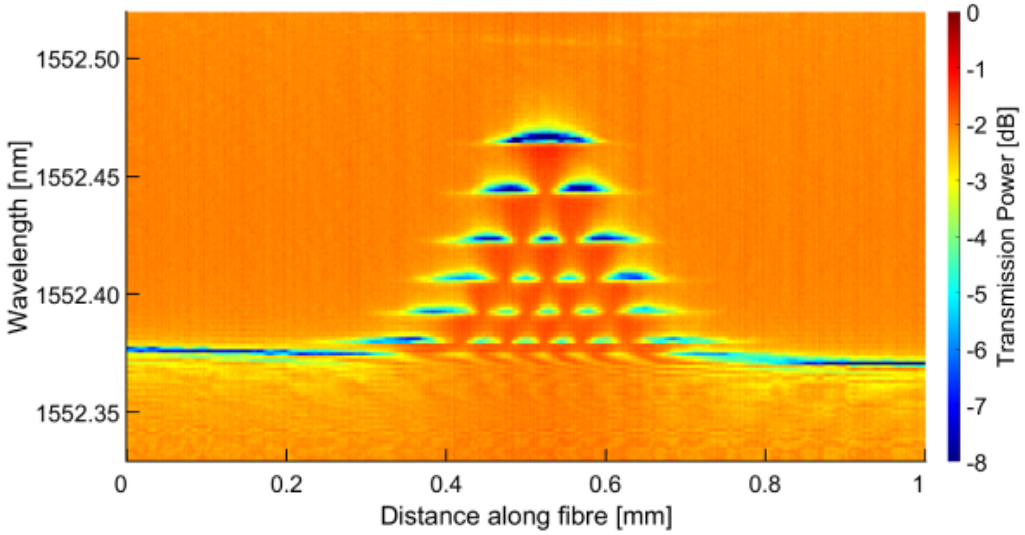

Figure 2.16: Standard SNAP spectrogram format used for characterizing the resonators explored in this study. The wavelength resolution is 1.4 pm, the spatial resolution is 2 μm.

In summary, a spatial spectrogram for a resonator provides a detailed view of the resonator's behavior across a spatial dimension, revealing where certain frequencies or modes are most prominent and how they're distributed across the structure.

Here's a breakdown for a spatial spectrogram of a resonator:

Spatial Axis: The horizontal axis represents the spatial dimension, such as distance along a waveguide or position within a resonator. As we move from left to right, we observe how the wavelengths in the resonator change over different spatial positions.

Wavelength Axis: The vertical axis corresponds to wavelength. Certain positions exhibit specific dominant frequencies or modes depending on the resonator's type and characteristics.

Transmission power: The color on the spatial spectrogram indicates the intensity of each wavelength at a given spatial position. Brighter colours indicate areas of higher transmission power.

Resonant Peaks: In a spatial spectrogram of a resonator, we see distinct lines or bands at particular wavelengths. These indicate spatial regions where specific resonant modes are most prominent.

Mode Profiles: Unlike a temporal spectrogram, which might show the evolution of modes over time, a spatial spectrogram will give insight into the spatial mode profiles of the resonator. These profiles can be vital for understanding the propagation and distribution of light within the resonant structure.

Spatial Harmonics: Depending on the nature of the resonator and the phenomenon being studied, one might observe repeated patterns or harmonics in your spectrogram, representing repeated or periodic spatial variations in the frequency response.

2.4 Foundations of SNAP

2.4.1 Maxwell's equations

We turn to Maxwell's equations to understand the theoretical propagation of an electromagnetic wave through an optical fibre. We derive the Helmholtz equation for wave propagation by assuming a harmonic time dependence. The solutions to this equation give us the possible modes. In a uniform and isotropic dielectric medium, and in the absence of free electric charges and currents, Maxwell's equations can be described as:

$$\nabla \times \vec{E} = -\mu \frac{\partial \vec{H}}{\partial t}, \nabla \times \vec{H} = \epsilon \frac{\partial \vec{E}}{\partial t} \tag{2.15}$$

$$\nabla \cdot \vec{E} = 0, \nabla \cdot \vec{H} = 0 \tag{2.16}$$

Where μ denotes the magnetic permeability, given by $\mu = \mu_r \mu_0$, and ε represents the electric permittivity of the material, expressed as $\varepsilon = \varepsilon_r \varepsilon_0$. We derive the Helmholtz equation by assuming a harmonic time dependence for the field and applying the curl operation :

$$\nabla^2 \Psi + k^2 \Psi = 0, \quad \Psi = \vec{E}, \vec{H} \tag{2.17}$$

Given that $k^2 = \omega^2 \mu \epsilon$ and $\omega = \frac{kc}{n}$ we can write :

$$\mu\epsilon = \frac{n^2}{c^2} \tag{2.18}$$

n is the refractive index.

2.4.2 Step-index Fibre

A step-index fibre is an optical waveguide with a circular and consistent cross-sectional profile. It features a core with a uniform refractive index, n_{core}, encircled by a cladding with a consistent refractive index, n_{clad} [12]. The core has a radius denoted by r_{core}.

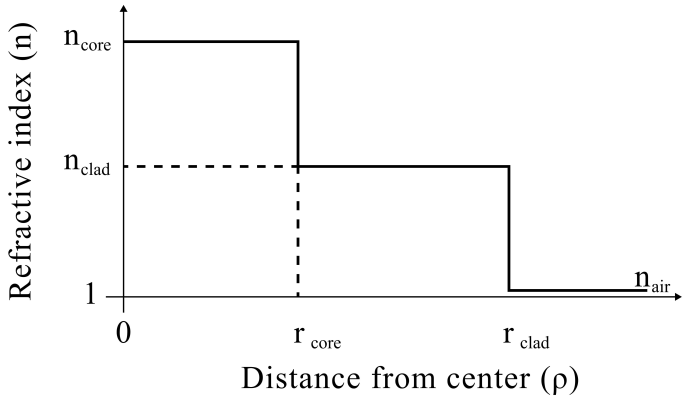

Figure 2.17: Refractive index profile of a step-index fibe.

In waveguides devoid of free charge sources, the Helmholtz equation $(\nabla^2\Psi + k^2\Psi = 0, \quad \Psi = \vec{E}, \vec{H})$ serves as an eigenvalue problem for k, having eigenfunctions denoted as $\vec{E}(\vec{r}, \vec{k})$. These eigenfunctions are referred to as field modes. When considering harmonic fields in free space, a time-varying solution to this equation results in a plane wave.

$$\vec{E}(\vec{r}, t) = \vec{E}_0 exp^{i(\vec{k}.\vec{r} - wt)} \tag{2.19}$$

In cylindrical coordinates (ρ, ϕ, z), the fields are characterized with z as the longitudinal propagation direction, while (ρ, ϕ) serve as the transverse coordinates.

$$E(\rho,\phi,z) = e(\rho,\phi)exp^{ik_z z}, H(\rho,\phi,z) = h(\rho,\phi)exp^{ik_z z} \tag{2.20}$$

k_z is the propagation constant along the z axis. The gradient operator in cylindrical coordinates is $\nabla f = \frac{\partial f}{\partial \rho}\hat{\rho} + \frac{1}{\rho}\frac{\partial f}{\partial \phi}\hat{\phi} + \frac{\partial f}{\partial z}\hat{z}$. For a field propagating along the z-axis in an optical fiber, the fiber's inherent cylindrical symmetry enables the representation of the Helmholtz equation as:

The Helmholtz equation in these coordinates, specifically for the radial dependence, is:

$$\frac{\partial^2\Psi}{\partial\rho^2} + \frac{1}{\rho}\frac{\partial\Psi}{\partial\rho} + \frac{1}{\rho^2}\frac{\partial^2\Psi}{\partial\phi^2} + \frac{\partial^2\Psi}{\partial z^2} + k^2\Psi = 0 \tag{2.21}$$

Where: Ψ represents the field component. k is the wave number.

Due to the very slow propagation of the WGMs, the field has very little variation along the z axis, in this approximation $\partial_z^2 = 0$ and we can write :

$$(\frac{\partial^2}{\partial\rho^2} + \frac{1}{\rho}\frac{\partial}{\partial\rho} + \frac{1}{\rho^2}\frac{\partial^2}{\partial\phi^2} + k_T^2)e_z(\rho,\phi) = 0 \tag{2.22}$$

and

$$(\frac{\partial^2}{\partial\rho^2} + \frac{1}{\rho}\frac{\partial}{\partial\rho} + \frac{1}{\rho^2}\frac{\partial^2}{\partial\phi^2} + k_T^2)h_z(\rho,\phi) = 0 \tag{2.23}$$

k_T is the transverse wave number in this 2D eigenvalue differential equation.

$$k_T^2 = k^2 - k_z^2 = \omega^2\mu\epsilon(\vec{\rho_T}) \tag{2.24}$$

Using coordinate separation: $e_z(\rho,\phi) \propto R(\rho)\Phi(\phi)$ and $h_z(\rho,\phi) \propto R(\rho)\Phi(\phi)$, we get second order differential equations:

$$(\frac{\partial^2}{\partial\phi^2} + m^2)\Phi(\phi) = 0 \tag{2.25}$$

$$(\frac{\partial^2}{\partial\rho^2} + \frac{1}{\rho}\frac{\partial}{\partial\rho} + k_T^2 - \frac{m^2}{\rho^2})R(\rho) = 0 \tag{2.26}$$

The harmonic azimuthal independent solutions for Equation 2.25 :

$$\Phi(\phi) = sin(m\phi)\Phi(\phi) = cos(m\phi) \tag{2.27}$$

m is an integer number that indicates the number of nodes of the field ($m \geq 0$).

In the context of cylindrical waveguides, such as the core of an optical fibre, the radial component of Equation 2.26 can be recast in the form of Bessel's differential equation. For any given m, with 2m signifying the number of field nodes, the general linear solution is described by the first kind of Bessel function.

$$R^m_{\rho<r_{core}}(\rho) = A_m J_m(k_T\rho) \tag{2.28}$$

Beyond the core, assuming cladding to be infinite $kz < n_{\text{clad}}k$, the boundary conditions necessitate the use of specific Bessel function combinations, often referred to as the Hankel functions of the first and second kind.

$$R^m_{\rho>r_{core}}(\rho) = B_m H^{(1)}_m(k_T\rho) + C_m H^{(2)}_m(k_T\rho) \tag{2.29}$$

with

$$H^{(1)}_m(k\rho) = J_m(k\rho) + iY_m(k\rho), H^{(2)}_m(k\rho) = J_m(k\rho) - iY_m(k\rho) \tag{2.30}$$

Establishing the boundary conditions results in the eigenvalue equation. Each eigenvalue specifically corresponds to a distinct radial mode number, denoted as p. Consequently, every mode is characterized by the two mode numbers: p (the radial mode number) and m (the azimuthal mode number). The eigenvalue equation for HE_{pm}, EH_{pm}, and whispering gallery modes, which possess a propagation constant of β and a wave number $k = \frac{2\pi}{\lambda}$ with a radius of ρ_0, is expressed as:

$$(F_{1m}(U) + F_{2m}(W))[F_{1m}(U) + \frac{n_{clad}^2}{n_{core}^2}F_{2m}(W)] = [\frac{m\beta}{kn_{core}}]^2[\frac{V}{UW}]^4 \tag{2.31}$$

with

$$F_{1m}(x) = \frac{1}{xJ_m(x)}\frac{dJ_m(x)}{dx}, F_{2m}(x) = \frac{1}{xH_m^{(2)}(x)}\frac{dH_m^{(2)}(x)}{dx} \tag{2.32}$$

U and W are defined by

$$U = r(k^2n_{core}^2 - \beta^2)^{\frac{1}{2}}; W = r(k^2n_{clad}^2\beta^2)^{\frac{1}{2}} \tag{2.33}$$

V is defined as $V = kr(n_{clad}^2 - n_{core}^2)^{\frac{1}{2}}$. When the propagation constant is zero, Equation 2.31 can be separated into two distinct equations. The equation for the TE modes is presented as:

$$F_{1m}(U_0) + F_{2m}(W_0) = 0 \tag{2.34}$$

And for TM modes as:

$$F_{1m}(U_0) + \frac{n_{clad}^2}{n_{core}^2} F_{2m}(W_0) = 0 \tag{2.35}$$

where $U_0 = n_{core}kr$, and $W_0 = n_{clad}kr$.

2.4.3 Quantum analogy

In this section, we explore the intersections between guided wave optics and quantum mechanics, laying the groundwork for understanding the theory of SNAP. We'll tackle the Helmholtz equation as applied to a fibre, drawing parallels with the Schrödinger equation. By examining the one-dimensional versions of these equations, we aim to shed light on the inherent similarities, providing a clearer understanding of the behaviour of light at the surface of SNAP devices.

2.4.3.1 Helmholtz equation

The general solution for waveguide modes, or the electric field in the z-direction, is given as:

$$E_z(x, z) = E_z(x)e^{i\beta z} \tag{2.36}$$

The function $E_z(x)$ represents the transverse eigenfunction of the guided mode profile moving along the z-axis within a dielectric step-index waveguide having a core width of $2d$. Within the distance range of $-d$ to d, the refractive index is set to n_1 — corresponding to the core's refractive index. Outside of this range, either beyond d or below $-d$, the refractive index is n_2, associated with the cladding. Given this setup, the Helmholtz equation can be expressed as:

$$
\begin{aligned}
[\frac{d^2}{dx^2} + k_T^2]E_z &= [\frac{d^2}{dx^2} + (k^2 - k_z^2)]E_z, \\
&= [\frac{d^2}{dx^2} + \omega^2\mu\epsilon(x) - k_z^2]E_z, \\
&= [\frac{d^2}{dx^2} + k_0^2 n^2(x) - k_z^2]E_z = 0,
\end{aligned}
\tag{2.37}
$$

The eigenvalue k_T is defined as $k_T^2 = k^2 - k_z^2$, representing the transverse propagation constant. Here, k_z is the longitudinal propagation state and $|k|^2 = \omega^2\mu\epsilon(x)$. Furthermore, $k_0^2 n^2$ describes the cross-sectional index profile.

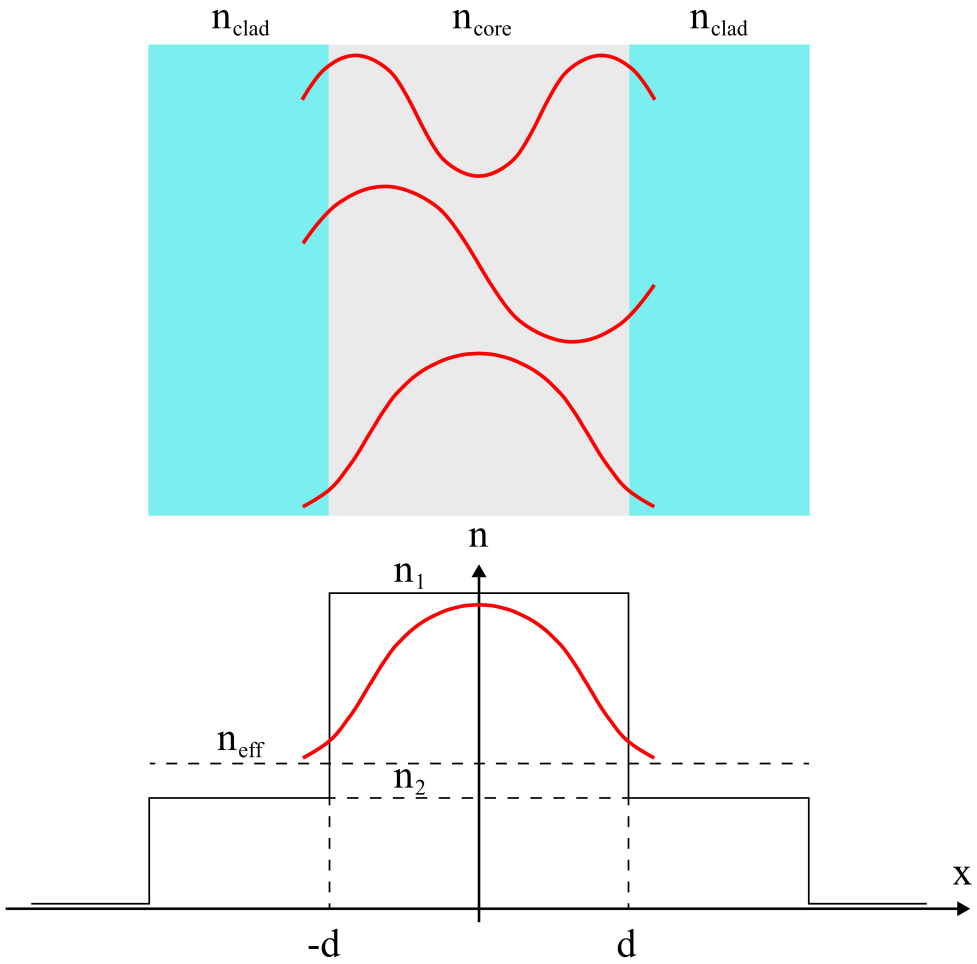

Figure 2.18: Solution of the 1D Helmholtz equation within a step-index dielectric waveguide.

There are three key observations in the depicted figure, which illustrate the solution to the one-dimensional Helmholtz equation for a step-index dielectric waveguide. Firstly, only specific, discrete propagation constant (k_T) values are viable. Secondly, higher-order modes exhibit more nodes, where $E_z(x) = 0$. Lastly, extended waveguides with a pronounced index contrast can support a more diverse set of modes, particularly when considering guided modes:

$$n_{\text{clad}} < n_{\text{eff}} < n_{\text{core}} \tag{2.38}$$

2.4.3.2 Time-independent Schrodinger equation

Conversely, the time-independent Schrödinger equation provides a solution for the wavefunction $\psi(r)$, associated with an eigenvalue energy E for a particle of mass m. This is visually represented in Figure 2.19 Notably, for distances outside the range $[-d, d]$, the potential is V_2, while within this range, it is V_1. The one-dimensional representation of the time-independent Schrödinger equation can be expressed as:

$$\frac{\hbar^2}{2m}\frac{d^2\Psi}{dx^2} + V(x)\Psi - E\Psi = 0 \tag{2.39}$$

with wavefunctions (energy eigenstates) :

$$U(x,t) = \Psi(x)e^{-i\frac{E}{\hbar}t} \tag{2.40}$$

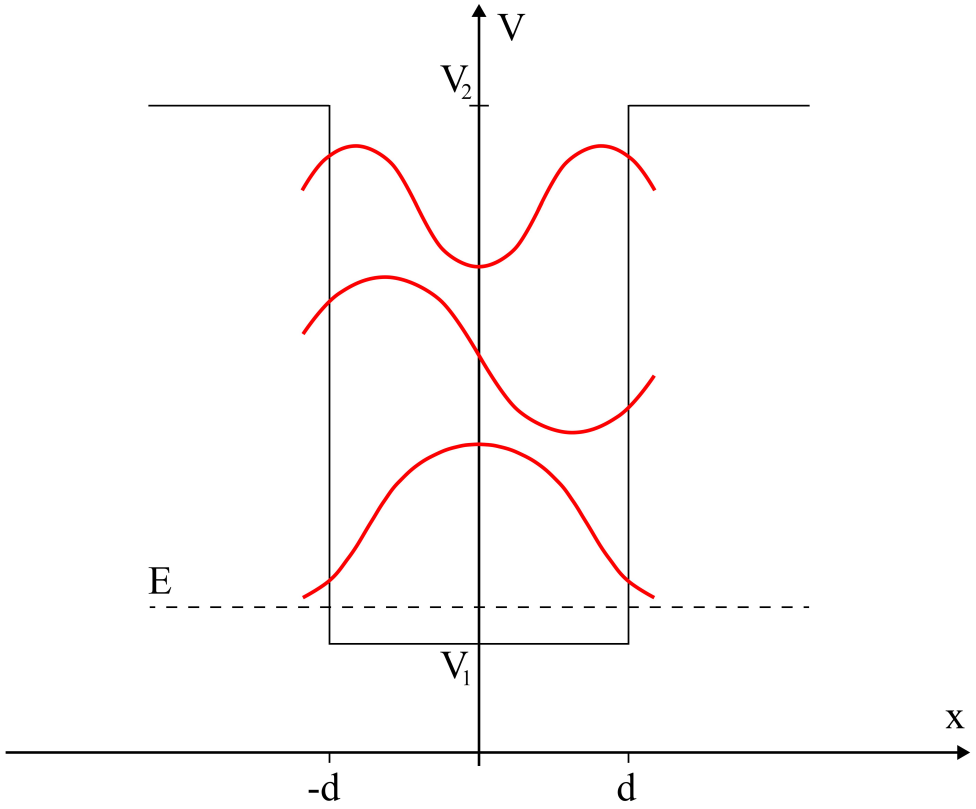

Figure 2.19: One-dimensional solution to the time-independent Schrödinger equation.

Given that $\Psi(x)$ represents the time-independent wave function, a comparison between Equations 2.37 and 2.39 reveals noteworthy parallels. Specifically, the potential $V(x)$ in Schrödinger's equation mirrors $-n^2(x)$ in the Helmholtz equation. Simultaneously, the energy (or eigenvalue) E corresponds to the propagation constant along the z-axis, k_z^2. The energy levels are quantised within a one-dimensional potential well, signifying that only distinct energy values are permissible. Moreover, wave functions with higher energy exhibit increased nodes, where $\psi(x) = 0$. Both the depth and width of the potential well play a role in the number of bounded states produced. For bounded states:

$$V_2 < E < V_1 \tag{2.41}$$

The correspondence between the two equations is concisely presented in the following table:

Table 2.1: The guided optical waves and Quantum mechanics

Guided wave	**Quantum mechanics**
Helmholtz equation in a waveguide: $[\nabla^2 + k_0^2 n^2(x) - \beta^2]E_z = 0$	1D time-independent Schrödinger equation: $\frac{-\hbar^2}{2m}\frac{d^2\Psi}{dx^2} + V(x)\Psi - E\Psi = 0$
$E_z(x)$: x-sectional optical mode	$\Psi(x)$: time-independent wavefunction
$k_0^2 n^2(x)$: x-sectional index profile	$V(x)$: potential energy
β^2: propagation constant	E: energy (eigenvalue)
Electric field along z-direction: $E_z(x,z) = E_z(x)e^{i\beta z}$	Time-dependent wavefunction: $U(x,t) = \Psi(x)e^{-i\frac{E}{\hbar}t}$
Discretized propagation constant - β values	Discretized energy levels - states
Transverse standing wave for confined photon	Transverse standing wave for bound particle
Longer with higher index contrast waveguide, contains more modes	Broader and deeper potential well contains more bounded states
Higher order modes support more nodes ($E = 0$)	Wavefunction with higher energy supports more nodes ($\Psi = 0$)
Guided modes: $n_{\text{clad}} < n_{\text{eff}} < n_{\text{core}}$	Bound states: $V_1 < E < V_2$

2.4.3.3 SNAP theory

Revisiting Equation 2.21, if we take into consideration that $\Psi \propto \exp(im\phi)\exp(i\beta z)$ along the azimuthal direction, then $\partial_z^2 = -\beta^2$ and $\frac{1}{\rho^2}\partial_\varphi^2 = -\frac{m^2}{\rho^2}$, with m being

the discrete azimuthal quantum number and β as the propagation constant. With these considerations, the equation can be recast as Bessel's differential equation.

$$\partial_\rho^2\Psi + \frac{1}{\rho}\partial_\rho\Psi + (k^2 - \frac{m^2}{\rho^2} - \beta^2)\Psi = 0 \tag{2.42}$$

This forms the foundation of the Helmholtz equation in cylindrical coordinates. With this context, we delve into the SNAP theory. Several approximations are made for a SNAP device exhibiting nanoscale radial variations. Initially, we postulate that the field propagates within the wall of a SNAP fibre, predominantly in the z-direction. Furthermore, we presume the absence of input or output waveguides in the fibre. This means the propagating field primarily rests on the whispering gallery modes (WGMs) within the wall of the SNAP fibre. These WGMs are characterized by azimuthal quantum number m, radial quantum number p, and the axial quantum number q. The axial component remains consistent within the SNAP microresonator, but its amplitude is acutely sensitive to the fibre's bridge. Lastly, we model light propagation as adiabatic, indicating that SNAP's effective radius variation is gradual, ensuring the mode shape remains undisturbed, and, consequently, the scale of the propagating light remains consistent. In cylindrical coordinates (z, ρ, φ), the field distribution is characterized as [13].

$$E_{mpq}(z, \rho, \varphi) = \exp(\pm im\varphi)Q_{mp}(\rho)\Psi_{mpq}(z) \tag{2.43}$$

where $\Psi_{mpq}(z)$ represents the distribution of the WGMs along the z-axis. By integrating this expression into the Helmholtz equation, we obtain:

$$(\nabla^2 + k^2)\exp(\pm im\varphi)Q_{mp}(\rho)\Psi_{mpq}(z) = 0 \tag{2.44}$$

A decomposition of the transversal (x, y) and longitudinal (z) fields can be employed to simplify this equation for cylindrical waveguides. As illustrated in Equation 2.24, the propagation constant (k) can be expressed as $k^2 = k_T^2 + k_z^2$, where k_T and k_z denote the transverse and longitudinal propagation constants respectively. When accounting for a lossless wave propagating within the wall of a fiber, k_z can be approximated as β. The distinct slowness of WGMs is highlighted by the diminutive value of their $\beta(z)$, or equivalently, by how close their wavelength λ is to the cutoff wavelength. Despite the cutoff wavelengths of the WGMs with exceedingly large azimuthal quantum numbers m corresponding to zero propagation constant, $\beta = 0$, this doesn't conflict with the widely recognized relationship $k_{mp} n_{\text{ext}} < \lambda < k_{mp} n_{\text{cap}}$ for small m [14]. Consequently, we can express:

$$k^2 = k_T^2 + \beta^2 \tag{2.45}$$

With this, Equation 2.44 becomes :

$$\nabla^2(\Psi_{mpq}(z) Q_{mp}(\rho) \exp(\pm im\varphi)) + (k_T^2 + \beta^2)\Psi_{mpq}(z) Q_{mp}(\rho) \exp(\pm im\varphi) = 0 \tag{2.46}$$

and then :

$$\begin{aligned} \Psi_{mpq}(z)\nabla_\perp^2(Q_{mp}(\rho) \exp(\pm im\varphi)) + (Q_{mp}(\rho) \exp(\pm im\varphi))\frac{d^2\Psi}{dz^2}, \\ +K_T^2(\Psi_{mpq}(z) Q_{mp}(\rho) \exp(\pm im\phi)) + \beta^2(\Psi_{mpq}(z) Q_{mp}(\rho) \exp(\pm im\varphi)) = 0, \end{aligned} \tag{2.47}$$

We can split Equation 2.47 and rewrite it as :

$$\frac{1}{Q_{mp}(\rho)\exp(\pm im\phi)}[\nabla_{\perp}^{2}(Q_{mp}(\rho)\exp(\pm im\phi)) + K_{T}^{2}]\Psi_{mpq}(z) + \frac{1}{Q_{mp}(\rho)\exp(\pm im\phi)}[\frac{d^{2}}{dz^{2}} + \beta^{2}]\Psi_{mpq}(z) = 0 \tag{2.48}$$

By evaluating this equation, we derive the one-dimensional Schrödinger equation as:

$$\frac{d^{2}\Psi_{mpq}}{dz^{2}} + \beta^{2}(\lambda, z)\Psi_{mpq} = 0, \quad \beta^{2}(\lambda, z) = E(\lambda) - V(z) \tag{2.49}$$

where the effective energy, representing the proportionality to the deviation of the wavelength from the cutoff wavelength, is determined as:

$$E(\lambda) = -k^{2}\frac{\nabla\lambda}{\lambda_{0}} \tag{2.50}$$

and the effective potential of the wave corresponds to the variation in both radius and refractive index, or equivalently, the change in the effective radius. This is expressed as:

$$V(z) = -2k^{2}\left[\frac{\Delta r(z)}{r_{0}} + \frac{\Delta n(z)}{n_{0}}\right] = -2k^{2}\left[\frac{\Delta r_{\text{eff}}(z)}{n_{0}r_{0}}\right] \tag{2.51}$$

where $k = \frac{2\pi n_{0}}{\lambda_{0}}$.

The first-order perturbation theory can be used to derive the propagation constant of a slow Whispering Gallery Mode (WGM) [15]. The solution of the Helmholtz equation in an axially symmetric optical fibre in cylindrical coordinates (ρ, z, φ) is given as in Equation 2.43, where the function $Q_{mp}(\rho, \varphi)$ satisfies the differential

equation [14].

$$\frac{d^2Q_{mp}(\rho,\lambda)}{d\rho^2}+\frac{1}{\rho}\frac{dQ_{mp}(\rho,\lambda)}{d\rho}+\left(\left(\frac{2\pi n(\rho)}{\lambda(z)}\right)^2-\frac{m^2}{\rho^2}-\beta_{mp}^2(\lambda)\right)Q_{mp}(\rho,\lambda)=0 \tag{2.52}$$

here, the radial distribution of the refractive index is denoted $n(\rho)$. When considering WGMs with $m \gg 1$, the cutoff wavelengths λ_{mp} correspond to a vanishing propagation constant.

$$\beta_{mp}(\lambda_{mp})=0 \tag{2.53}$$

we rewrite 2.52 as :

$$\boldsymbol{L}Q_{mp}(\rho,\lambda)=\beta_{mp}^2(\lambda)Q_{mp}(\rho,\lambda) \tag{2.54}$$

$$\boldsymbol{L}=\frac{d^2}{d\rho^2}+\frac{1}{\rho}\frac{d}{d\rho}+\left(\frac{2\pi n(\rho)}{\lambda}\right)^2-\frac{m^2}{\rho^2} \tag{2.55}$$

It can be inferred from Equation 2.55 that $\beta_{mp}^2(\omega)$ is the eigenvalue of the operator $\boldsymbol{L}$. As a result, from Equation 2.53, the functions $Q_{mp}(\rho,\lambda_{mp})$ are the eigenfunctions of the operator.

$$\boldsymbol{L}_{mp}^{(0)}=\frac{d^2}{d\rho^2}+\frac{1}{\rho}\frac{d}{d\rho}+\left(\frac{2\pi n(\rho)}{\lambda_{mp}}\right)^2-\frac{m^2}{\rho^2} \tag{2.56}$$

and possess zero eigenvalues. In this context, we focus on scenarios where the deviation in the cutoff wavelength, $\lambda_{mp}^{\text{cut}}(z)$ from λ_{mp}^0, and the discrepancy between

the radiation wavelength and its cutoff, $\lambda - \lambda_{mp}^{\text{cut}}(z)$, are minimal. This condition holds true for minor variations in radii, $\Delta r_{\text{int}}(z)$ and $\Delta r_{\text{ext}}(z)$, and for the evanescent values of $Q_{mp}(\rho, z)$ in proximity to the inner wall surface. Based on these assumptions, for small $\beta_{mp}(\lambda)$, we obtain:

$$\boldsymbol{L} = \boldsymbol{L}_{mp}^{(0)} + \Delta \boldsymbol{L}_{mp}^{(0)} \tag{2.57}$$

$$\Delta \boldsymbol{L}_{mp}^{(0)} = \left(\frac{2\pi n(\rho)}{\lambda}\right)^2 - \left(\frac{(2\pi n(\rho)}{\lambda_{mp}}\right)^2 \approx \frac{2(2\pi n(\rho))^2}{\lambda_{mp}^3}(\lambda_{mp} - \lambda) \tag{2.58}$$

Using Equation 2.58, we can determine the eigenvalues $\beta_{mp}^2(\lambda)$ in the first order of the perturbation theory [16].

$$\begin{aligned} \beta_{mp}^2(\lambda) &= \langle Q_{mp}(\rho, \lambda_{mp})| \, \Delta \boldsymbol{L}_{mp}^{(0)} \, |Q_{mp}(\rho, \lambda_{mp})\rangle \\ &= \frac{8\pi^2}{\lambda_{mp}^3} \langle Q_{mp}(\rho, \lambda_{mp})| \, \Delta \boldsymbol{L}_{mp}^{(0)} \, |Q_{mp}(\rho, \lambda_{mp})\rangle \, (\lambda_{mp} - \lambda) \end{aligned} \tag{2.59}$$

where functions $Q_{mp}(\rho, \lambda_{mp})$ are normalized, $\langle Q_{mp}(\rho, \lambda_{mp})| \, |Q_{mp}(\rho, \lambda_{mp})\rangle = 1$. we can disregard the contribution of evanescent parts of $Q_{mp}(\rho, \lambda_{mp})$ in Equation (2.59) which simplifies to:

$$\beta_{mp}^2(\lambda) = \frac{8\pi^2}{\lambda_{mp}^3} n_{cap}^2 (\lambda_{mp} - \lambda) \tag{2.60}$$

Finally, to streamline the solution process for the Helmholtz equation in an optical fibre, we can make the assumption that propagation in our system predominantly relies on WGMs, which are localized along the axis. The inherent slowness of WGMs is characterized by the minute magnitude of their propagation constant, β, or equivalently, the closeness of their wavelength λ to the cutoff wavelength

$\lambda_{mp}^{(\text{cut})}(z)$. With this in mind, Equation (2.52) can be reduced to a wavelength-independent form:

$$\partial_\rho^2 Q_{mp} + \frac{1}{\rho}\partial_\rho Q_{mp} + \left(\left(\frac{2\pi n(\rho, z)^{(cut)(z)}}{\lambda_{mp}} \right)^2 - \frac{m^2}{\rho^2} \right) Q_{mp} = 0 \tag{2.61}$$

The solution, taking into account the continuous refractive index profile and the boundary conditions, is given as follows:

$$Q_{m,p}(\rho, z) = \begin{cases} AJ_m(k_{mp} n_{core} \rho) & \text{for } 0 < \rho \leq r_{core}(z), \\ BJ_m(k_{mp} n_{clad} \rho) + CY_m(k_{mp} n_{clad} \rho) & \text{for } r_{core}(z) < \rho \leq r_{clad}(z). \end{cases} \tag{2.62}$$

Here, $k_{mp} = \frac{2\pi}{\lambda_{mp}}$, where $J_m(x)$ and $Y_m(x)$ are Bessel functions of the first and second kinds, respectively. The coefficients A, B, and C are determined by applying the electromagnetic boundary conditions, ensuring the continuity of $Q_{mp}(\rho, z)$ and its derivative with respect to ρ at the core-cladding interface.

2.4.3.4 SNAP devices

SNAP devices are categorized into three distinct regimes, as depicted in Figure 2.20. The energy position, E, characterizes the SNAP device structure analogous to the fundamental quantum mechanical phenomena [16]. In this context, E is related to the wavelength detuning from the resonator. The location z_1 designates the microfiber's position along the SNAP fiber.

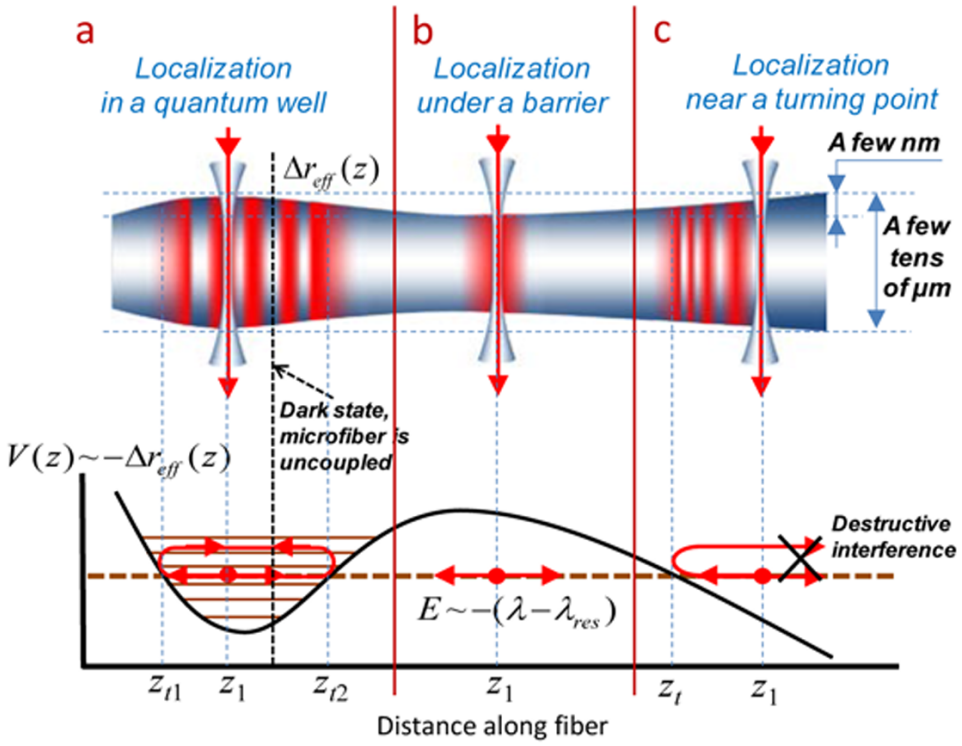

Figure 2.20: SNAP device classifications: a. WGM bottle-shaped microresonator [2]]. b. Inward-curved fiber waist [2]. c. Gradual alteration in fiber diameter [2].

The initial regime reveals a bottle microresonator [17], analogous to a quantum well, where the potential aligns with the negative shift in the effective radius. In this regime, the presence of a microfiber induces the emergence of excited WGMs. These modes are confined between z_{t1} and z_{t2} across different wavelength series, giving rise to discrete states. At z_1, the resonance transmission magnitude is governed by the WGM's amplitude [2]. When the microfiber aligns with a WGM node, the coupling is absent, leading to "dark" WGMs. These are marked as dark states in Figure 2.20. Reflections at z_{t1} and z_{t2} due to effective radius variations cause constructive interference [18].

The subsequent regime showcases a slight concave fiber waist, likened to a potential barrier. When energy surpasses the potential, non-localized WGMs emerge

within the SNAP device. However, if it's below, the excited WGMs experience exponential decay from z_1. In instances where effective radius variations are nil (signifying a consistent fiber), WGMs exhibit a delocalized behavior. Thus, excited WGMs within a consistent fiber radiate axially. This resonance is seldom observed due to Gaussian beam self-interference occurring near the surface. Moreover, the resonance quality factor is substantially lower, about 2.5 times, compared to analogous modes in spheroidal microresonators [19].

Lastly, the third regime sees a consistent rise in the SNAP device radius approaching z_1. Here, excited WGMs moving toward a decreasing radius (or negative SNAP device direction) from z_1 collide with WGMs reflected from z_t. Conversely, those in the positive direction experience destructive interference. As a consequence, light propagation primarily occurs between z_t and z_1 within this regime [18].

2.5 Existing SNAP fabrication techniques

The fabrication of Surface Nanoscale Axial Photonics (SNAP) devices involves creating precise nanoscale modifications along the optical fiber to manipulate light propagation. Here are several key techniques currently used in SNAP device fabrication:

Femtosecond Laser Micromachining: This method uses ultra-short pulses from a femtosecond laser to induce localized changes in the refractive index of the fiber's core or cladding. The high precision and minimal thermal effects of femtosecond lasers allow for the creation of axial variations with nanometer accuracy without significantly damaging the fiber.

Ion Beam Irradiation: Ion beam irradiation modifies the refractive index of the

fiber by bombarding it with focused beams of ions. The process can be finely controlled to adjust the size and refractive index change of the modified regions, enabling the creation of axial variations along the fiber.

Chemical Etching: In this technique, portions of the optical fiber are exposed to chemicals that selectively remove material from the fiber's surface. By controlling the concentration of the etching solution, exposure time, and area of exposure, axial variations with nanoscale precision can be achieved.

Photolithography and Etching: This involves coating the fiber with a photosensitive material, then exposing it to light through a mask that defines the pattern of the axial variations. The exposed areas are then developed, and the underlying fiber is etched away, creating the desired nanoscale features.

CO2 Laser Processing: A focused CO2 laser beam can be used to locally heat specific regions of the fiber, causing expansion or other modifications that alter the optical properties of the fiber. This method allows for the adjustment of the diameter of the fiber at nanoscale intervals along its axis.

Nano-Imprint Lithography: This technique involves pressing a mold with nanoscale features into the surface of the optical fiber, transferring the pattern directly onto the fiber. This method can efficiently produce uniform and repeatable nanoscale features over long sections of fiber.

Each of these techniques offers different advantages in terms of precision, scalability, and compatibility with various types of optical fibers. The choice of fabrication method depends on the specific requirements of the SNAP device being developed, including the nature of the optical effects desired, the type of fiber used, and the application's sensitivity and resolution requirements. Researchers continue to refine these techniques and explore new methods to enhance the capabilities and applications of SNAP technology.

3 | Method 1: Thermal sculpting

We delve into a novel technique to fabricate SNAP resonators utilising a simple butane torch. While prevailing fabrication methodologies offer precision in effecting desired changes to the effective radius, they are contingent upon access to niche equipment and materials, like CO2 lasers or photosensitive fibres. This research demonstrates an alternative approach, enabling SNAP resonator fabrication in settings with rudimentary SNAP setups complemented by a butane torch. Through evanescent spectroscopy, we analyze the resonators birthed from this method. The resultant transmission spectra substantiate that a flame-induced effective radius variation can achieve complete light localisation. Furthermore, the resonators forged in this manner can sustain exceptionally low-loss resonant modes.

3.1 Reading a SNAP spectrogram

A brief primer on how to interpret spectrograms is essential, given that they represent the primary characterization tool utilized throughout my research. Understanding their nuances and intricacies is pivotal to fully grasping the findings and analyses presented in this work.

Optical fibres often exhibit high-quality-factor optical resonance lines in their WGM spectra [20] [21] [22]. These particular resonances align with what is termed the cutoff wavelengths of light, denoted mp. In this context, m represents the azimuthal quantum number and p the radial quantum number. Together, they enumerate the modes travelling in an axially symmetric and uniform fibre. The formulation for the electromagnetic field associated with these modes is factorized when presented in cylindrical coordinates as [14]:

$$E^{\pm}_{mpq}(z,\rho,\varphi) = \exp(\pm i\beta_{mp}(\lambda)z + im\varphi)Q_{mp}(\rho) \tag{3.1}$$

The characteristic slowness of WGMs is evidenced by their small propagation constant, $\beta_{mp}(\lambda)$, and by how closely their wavelength, λ, approaches the cut-off wavelength, $\lambda^{\text{cut}}_{mp}(z)$. It's worth noting that the cutoff wavelengths for WGMs with large azimuthal quantum numbers, m, meaning a zero propagation constant, $\beta = 0$, is consistent with the established relation $k_{mp}n_{\text{ext}} < \beta < k_{mp}n$ for small m [14]. The function $Q_{mp}(\rho)$ declines exponentially outside the fibre for $\rho > r_{\text{ext}}$. WGMs of primary interest are those close to the optical fibre surface. As they approach cutoff wavelengths λ_{mp}, their propagation constants near zero, $\beta_{mp}(\lambda_{mp}) = 0$. Their sluggish axial propagation along the fibre enables them to be influenced by angstrom-scale fibre radius variations, as utilized in SNAP [23]. As discussed later, similar effective radius changes can be instigated by shifts in cutoff wavelengths λ_{mp} due to heat treatment (method 1) or due to the evanescent coupling of WGMs with another fibre (method 2).

Figure 3.1 displays values of λ_{mp} within the wavelength range $1540\,\text{nm} < \lambda < 1550\,\text{nm}$ for quantum numbers up to $p \leq 5$. The figure also depicts azimuthal quantum numbers, m, which range from 347 to 393. These numbers are likely to be detected in our experiments, on the other hand, WGMs with larger p values might be challenging to detect due to their scattering at interfaces and consequent high attenuation. It's important to note that transverse magnetic (TM)-polarized WGMs have lower quality factors compared to the TE-polarized ones. This difference is attributed to scattering from surface inconsistencies and bulk variations [3].

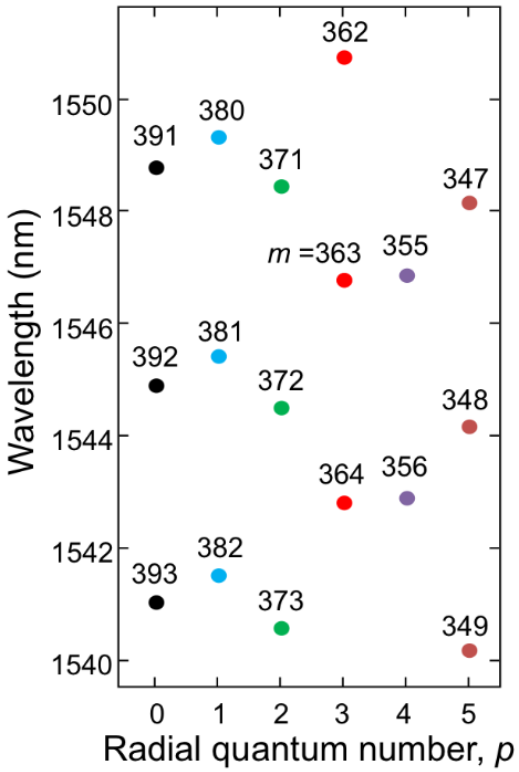

Figure 3.1: The cutoff wavelengths, represented by dots, correspond to TE-polarized WGMs with values of $p = 0, 1, 2, 3, 4,$ and 5 within the wavelength range of $1540\,\text{nm} < \lambda < 1550\,\text{nm}$. Adjacent to each dot, the respective azimuthal quantum numbers m are indicated [3].

For illustration, Figure 3.2 presents a surface plot detailing the transmission power $P(z, \lambda) = |A(z, \lambda)|^2$ for a target fibre exhibiting effective radius variations achieved by our Thermal sculpting method.

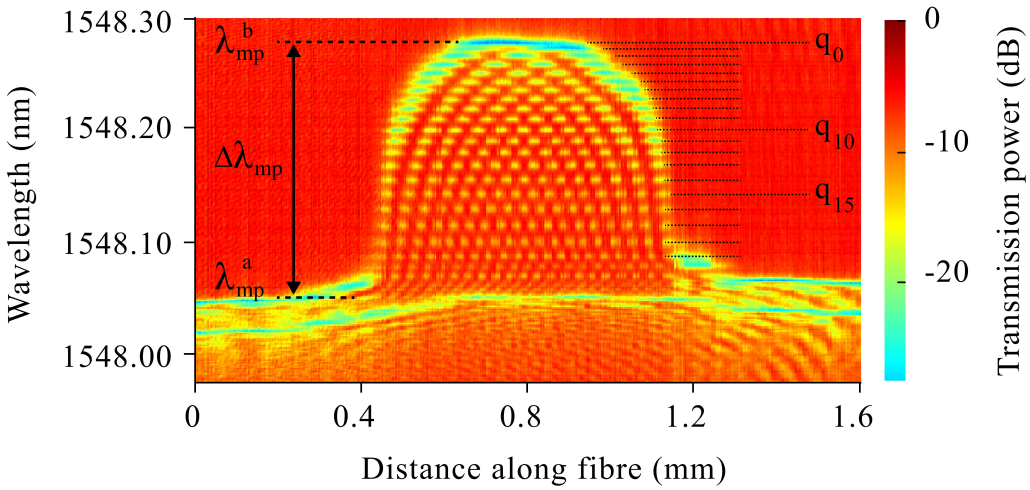

Figure 3.2: Spatial SNAP spectrogram, corresponding to a heat-induced shift in the cutoff wavelength of 0.25 nm.

The cutoff wavelength of the unaltered fibre is set to $\lambda^a_{mp} = 1548.05$ nm, we see an increase of $\Delta\lambda_{mp} = 0.25$ nm, shifting to $\lambda^b_{mp} = 1548.30$ nm within the heated zone. This adapted cutoff wavelength profile is analogous to a quantum well effectively acting as an optical microresonator. The horizontal resonance pathways showcasing alternating nodes and antinodes are indicative of the axial eigenvalues of this microresonator, characterized by quantum numbers $q = 0, 1, 2, 3....$ This structure can aptly be termed a heat-induced bottle microresonator.

3.2 SNAP setup preparation

Before we dive into the nuances of the thermal sculpting technique, it's imperative to touch upon the target and tapered fibre briefly.

3.2.1 Target Fibre Readying

The foundation for SNAP resonator fabrication is derived from a standard single-mode optical fibre, initially measuring 125 μm in diameter. Given the heightened surface sensitivity inherent to SNAP, removing the polymer jacket during the target fibre's preparation plays a pivotal role in determining the quality of the resultant resonator. The polymer can be removed chemically, but it can be challenging due to the resilience of these coatings, designed to protect the delicate inner glass fibre. Primarily, the polymer coating of an optical fibre is removed using mechanical stripping tools designed specifically for that purpose:

Figure 3.3: Fiber Optic Stripper.

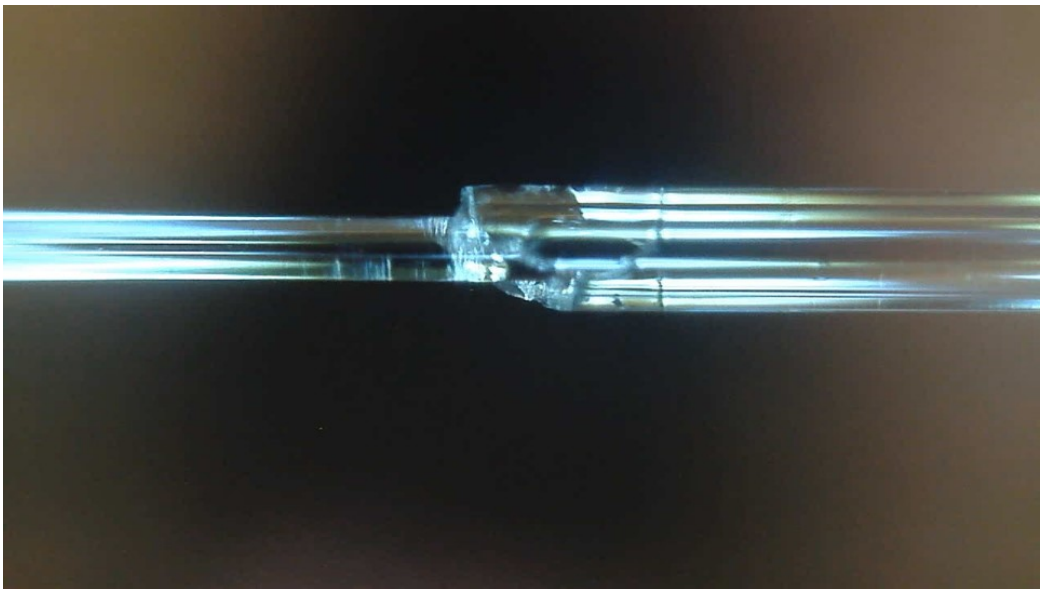

Figure 3.4: Close up of a 125 μm fibre with (right) and without polymer coating.

While the chemical stripping method can remove most of the polymer jacket, the outcome might not be flawless. A subsequent cleaning with isopropanol is often required to ensure the complete removal of any residual polymer. The quality of the surface can typically be assessed visually using a microscope :

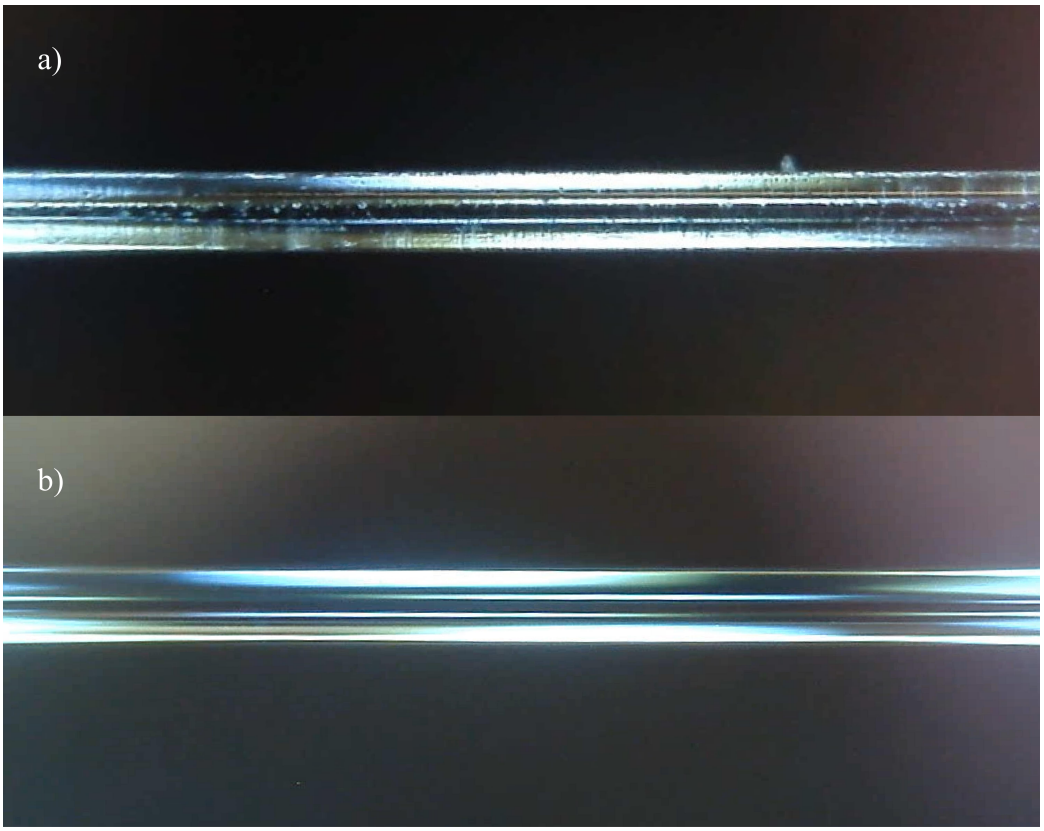

Figure 3.5: Close up of a stripped 125 μm fibre before **(a)** and after **(b)** cleaning it with isopropanol-soaked optical cleaning cloth.

An effective and definitive approach to gauge the surface quality of the target fiber during preparation is through spectrogram analysis. While microscopic visual inspection provides an initial assessment, capturing a spectrogram of a specific fiber section offers a more detailed representation of its surface condition. Such spectroscopic readings can highlight irregularities and imperfections, ensuring the fiber is optimally prepared before further processing or utilization.

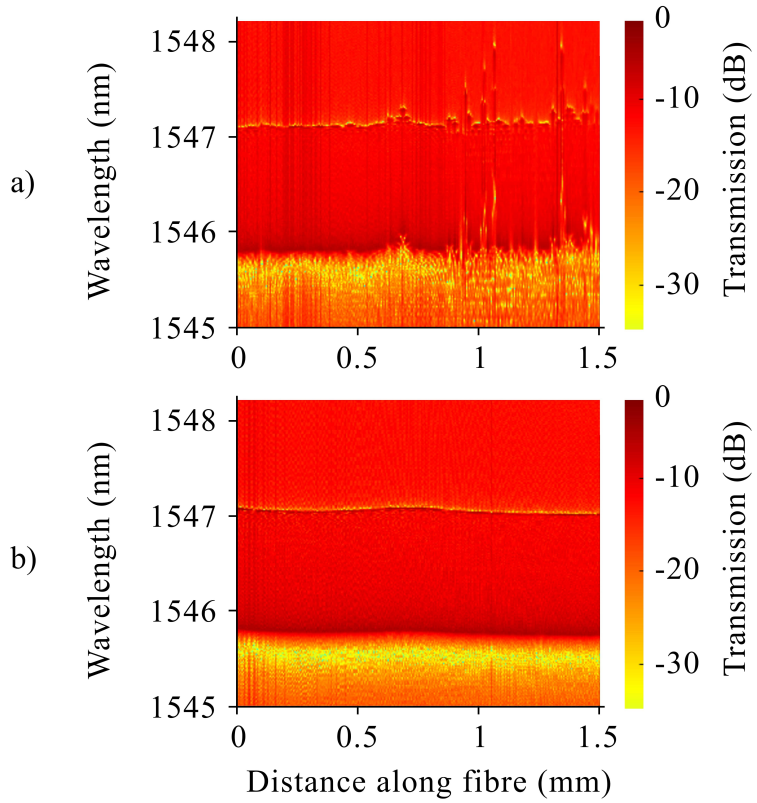

Figure 3.6: Spectrograms of a 1.5 mm fibre segment, scanned at 2 μm intervals. **(a)** Demonstrates a poorly cleaned fibre's response, and **(b)** highlights the spectrogram after a thorough cleaning process.

Whispering Gallery Modes (WGMs) in a SNAP resonator are highly sensitive to surface cleanliness. This is because WGMs reflect off the boundary between the fibre's cladding and the surrounding air. Even small amounts of dirt or impurities on the fibre's surface can disrupt these reflections. Essentially, a cleaner surface ensures that the WGMs function properly, highlighting the importance of keeping the fibre's exterior pristine.

3.2.2 Taper Readying

WGMs within the target fibre are examined by perpendicularly placing a microfiber against it. This microfiber, depicted below, originates from the identical stock fibre and boasts a biconical taper, with its waist diameter estimated at roughly 1 μm [24]. This tapered optical fibre remains in direct contact with the SNAP resonator during each Insertion Loss scan.

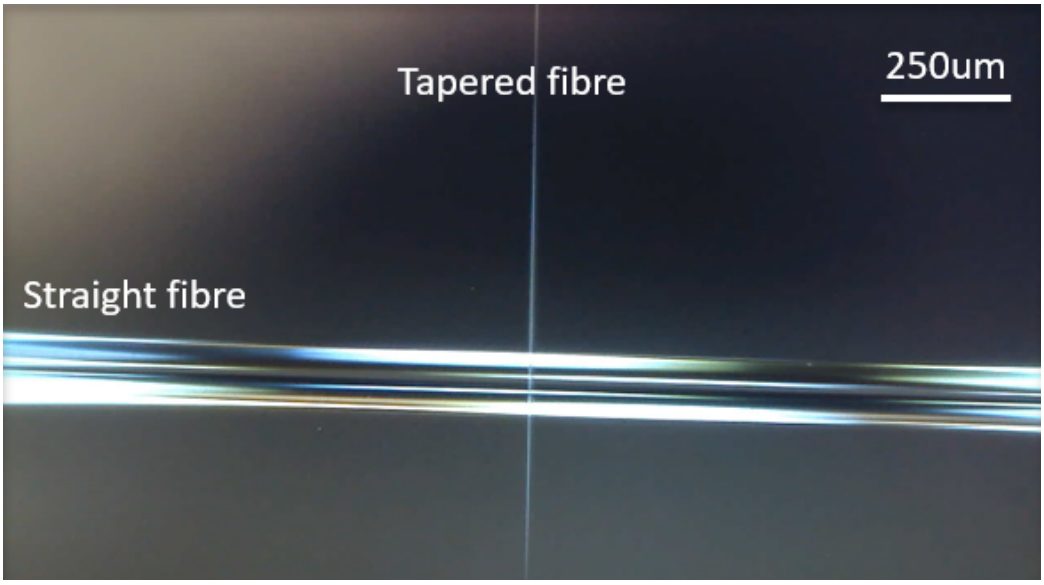

Figure 3.7: Close up of a stripped 125 μm fibre in contact with a tapered fibre.

Before characterising the SNAP resonators, it is imperative to ensure that the variations observed on the spectrogram arise from the resonator itself and not from the taper. The taper, which functions as a light input conduit and a resonator characterisation tool, can introduce variations if not properly calibrated or maintained.

The SNAP platform utilizes the tapered fibre as a crucial component to couple light into the Target Fibre. A standard SNAP spectrogram of a regular commercial 125 μm fibre without a polymer jacket near 1550 nm wavelength looks as such :

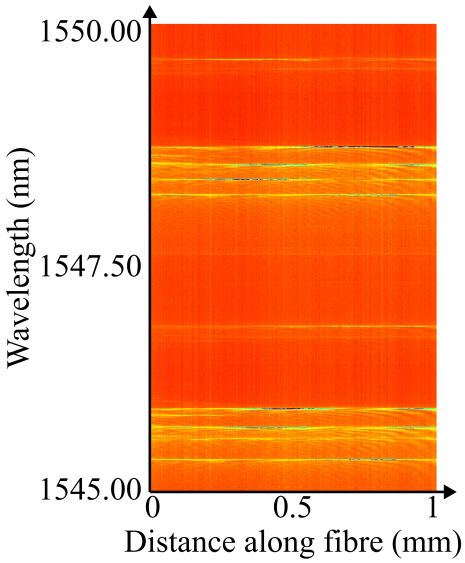

Figure 3.8: spatial SNAP spectrogram of an unaltered fibre.

We illustrated the scanning procedure for the spatial SNAP spectrogram in Figure 2.13.

The lines observed in the spectrogram of an unaltered fibre are indicative of the resonant modes. When a repeating pattern is seen, it can mean several things:

Mode Families: Optical fibres can support multiple whispering gallery modes (WGMs) classified into families. Within a family, you have radial, azimuthal, and polar modes. The repeating pattern might be due to consecutive azimuthal modes or other mode families.

Free Spectral Range (FSR): The spacing between consecutive resonant wavelengths for a particular mode family is termed the Free Spectral Range (FSR). It represents the wavelength difference between two successive modes of the same family. Regular patterns likely observe the FSR of the fibre for that mode family.

Birefringence Effects: Imperfections, bends, or asymmetry can introduce birefringence, leading to the splitting of degenerate modes. This can sometimes create

closely spaced resonances appearing as repeating patterns.

Theoretical models and experimental data are used to accurately determine each line's mode or mode family. Matching theory and experiment for WGMs can be challenging due to the sheer number of modes and their sensitivity to even minute changes.

While the tapered section is designed to be uniform, it is sensitive to minute variations in its own radius, and any small change in the position of the contact point along the tapered fibre can lead to very different spectrograms. This is unacceptable for consistently characterising a resonator. The extreme sensitivity emphasizes the importance of meticulous fabrication to maintain uniformity and the need for precise measurement tools during the characterisation process.

To characterize the tapered fibre, one can adopt a modified approach from the standard procedure used for the target fibre. Instead of maintaining a constant contact point on the tapered fibre while varying the contact point on the target fibre, the strategy is reversed. By keeping the contact point on the target fibre static and adjusting the contact point along the tapered fibre, one can gain insights into the taper's profile and performance intricacies.

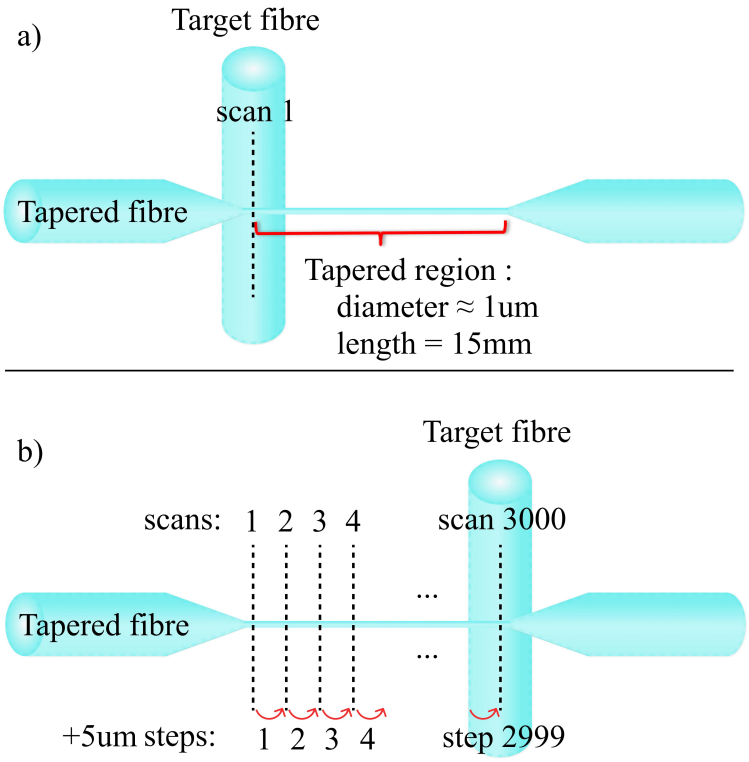

Figure 3.9: Setup for spatial spectrogram measurement of the taper. **(a)** Initial position for the scanning of the taper. **(b)** Final position for the scanning of the taper (3000 scans separated by 5 μm to cover the 15 mm tapered region).

As explained in Chapter 2, the 3000 scans are combined to form a spatial spectrogram of the tapered fibre that maps the cutoff wavelengths at different positions along the tapered section. This map can be used to find the optimal coupling position with the unaltered target fibre and sets a reference to track and characterise the changes that will be introduced in later experiments. The best position generally has relatively low losses and offers sharp cutoff wavelength dips in the insertion loss diagrams.

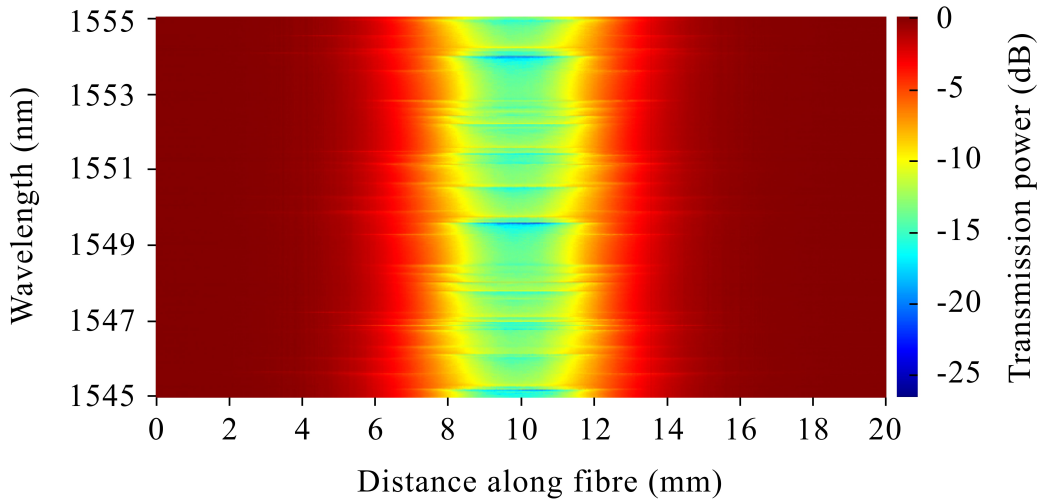

Figure 3.10: Spectrogram of a tapered fibre commonly used for SNAP characterisation, mapping the cutoff wavelengths of the target fibre at different positions. The centre of the tapered section is at z = 10 mm.

We can see that coupling the target fibre at various regions along the taper results in the emergence of distinct cutoff wavelengths. As the taper narrows towards its centre, there's an increased coupling of light into the target fibre. Even a minute shift, as slight as half a millimetre along the taper, can yield markedly different spectrograms. This underlines the precision and sensitivity of the system to positional changes during coupling.

In examining the spectrogram, a distinct symmetry emerges around the midpoint of the tapered section at $z = 10$ mm. This inherent symmetry suggests that it's sufficient to consider just one half of the spectrogram for analysis purposes. By focusing on this half, we can efficiently decipher and understand the various regions it presents.

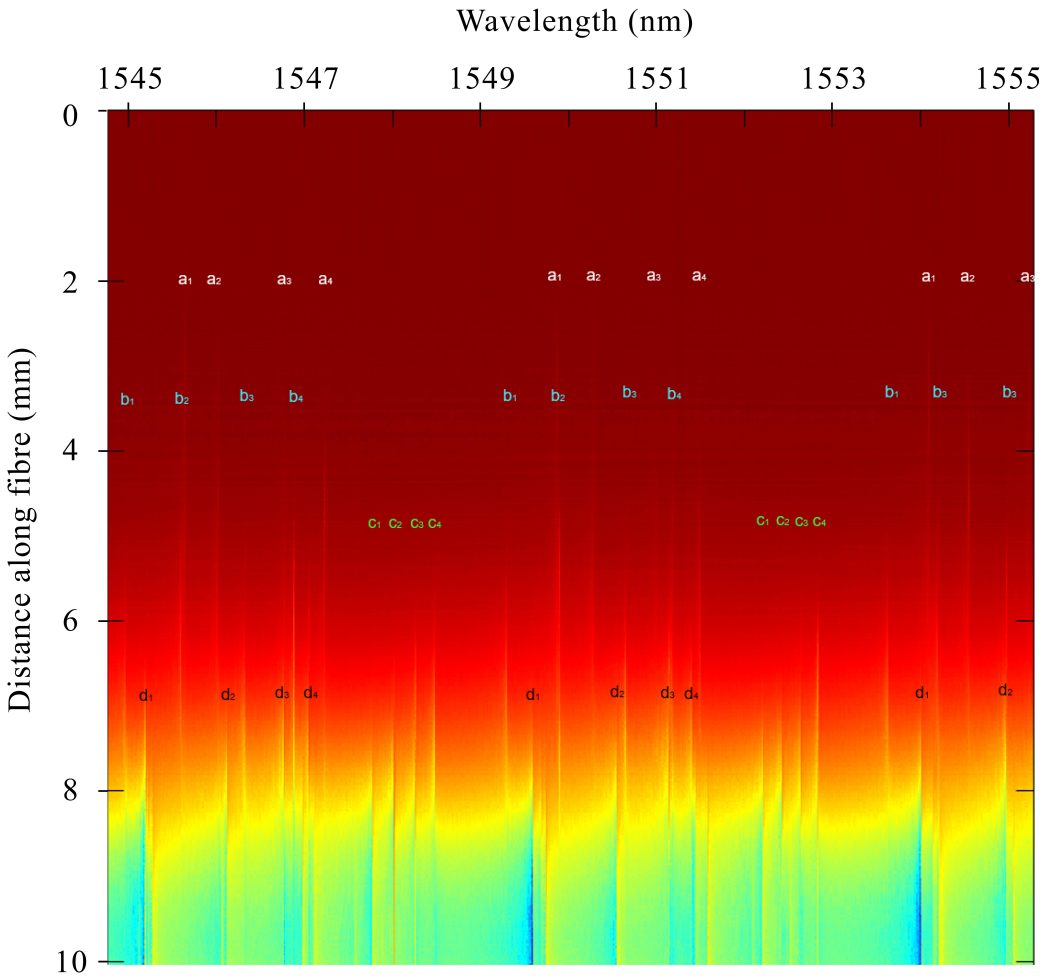

Figure 3.11: A 90 degree rotated half of the previous spectrogram.

From the figure, we see that as we approach the centre of the tapered region, both the losses and the number of cutoff wavelengths increase. This trend demarcates four distinct regions, each characterized by its unique cluster of cutoff wavelengths. These clusters have been labelled as a, b, c, and d in the figure for clearer reference and analysis. The following figures consider the four corresponding regions that can be identified.

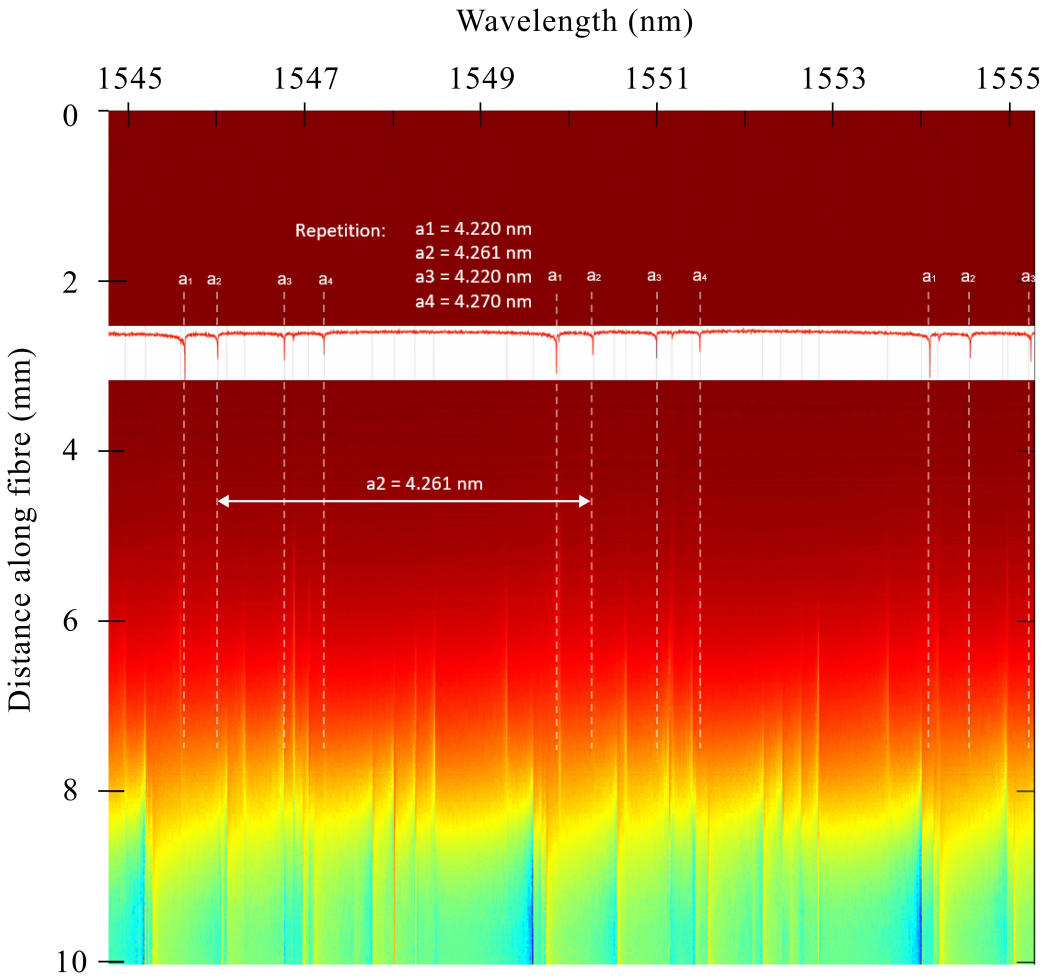

Figure 3.12: First region, 9-7 mm from the middle of the taper, an insertion loss of this region is inserted.

In the figure, we observe four distinct WGM cutoff wavelengths recurring at intervals of approximately 4.25 nm. This pattern is consistent with the external circumference of the target fibre. The losses are low, even the depth of the dips corresponding to these cutoff wavelengths is less than 2 dB.

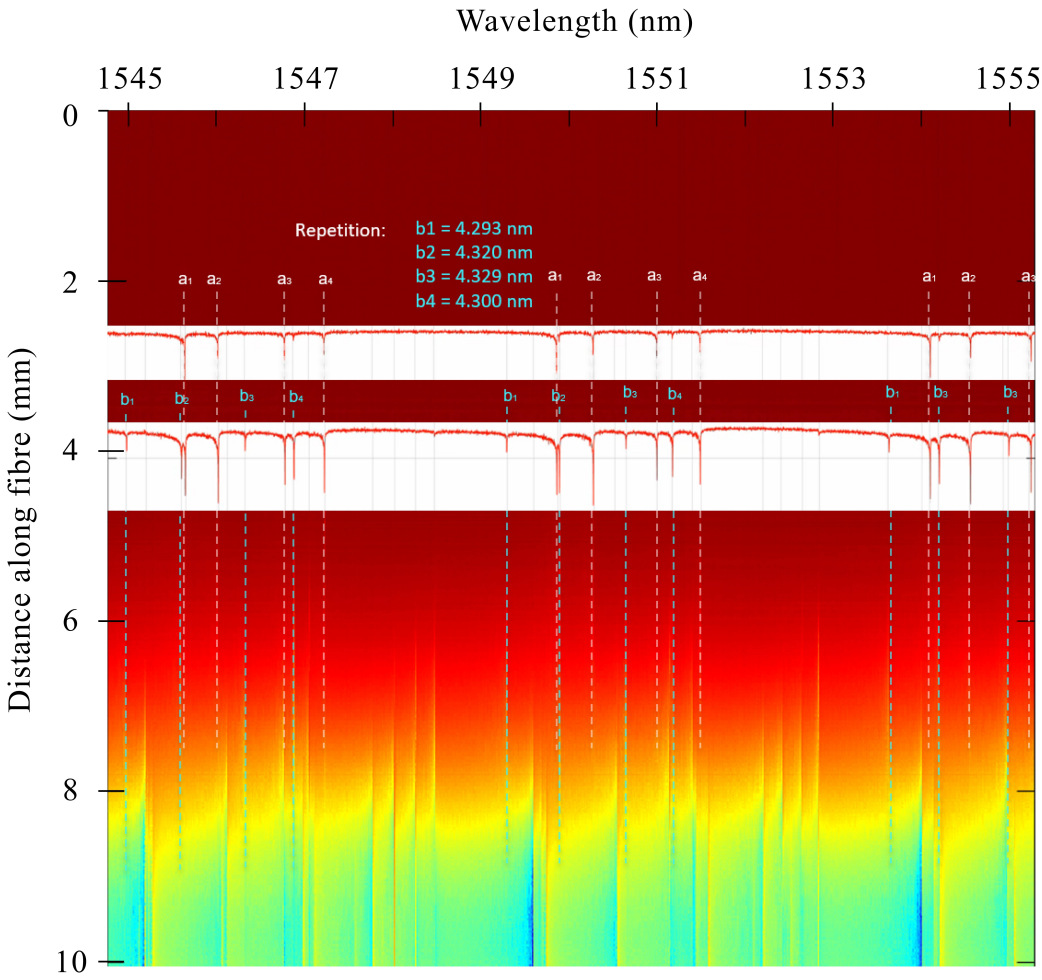

Figure 3.13: Second region, 7-5 mm from the middle of the taper, with the corresponding insertion loss diagram added.

Within 7-5 mm from the taper's centre, we can discern four additional cutoff wavelengths, recurring at intervals of 4.3 nm. This particular region is often the preferred choice for SNAP characterization. Its appeal lies in its relatively low-loss background and sharp resonance dips, indicative of a high Q-factor.

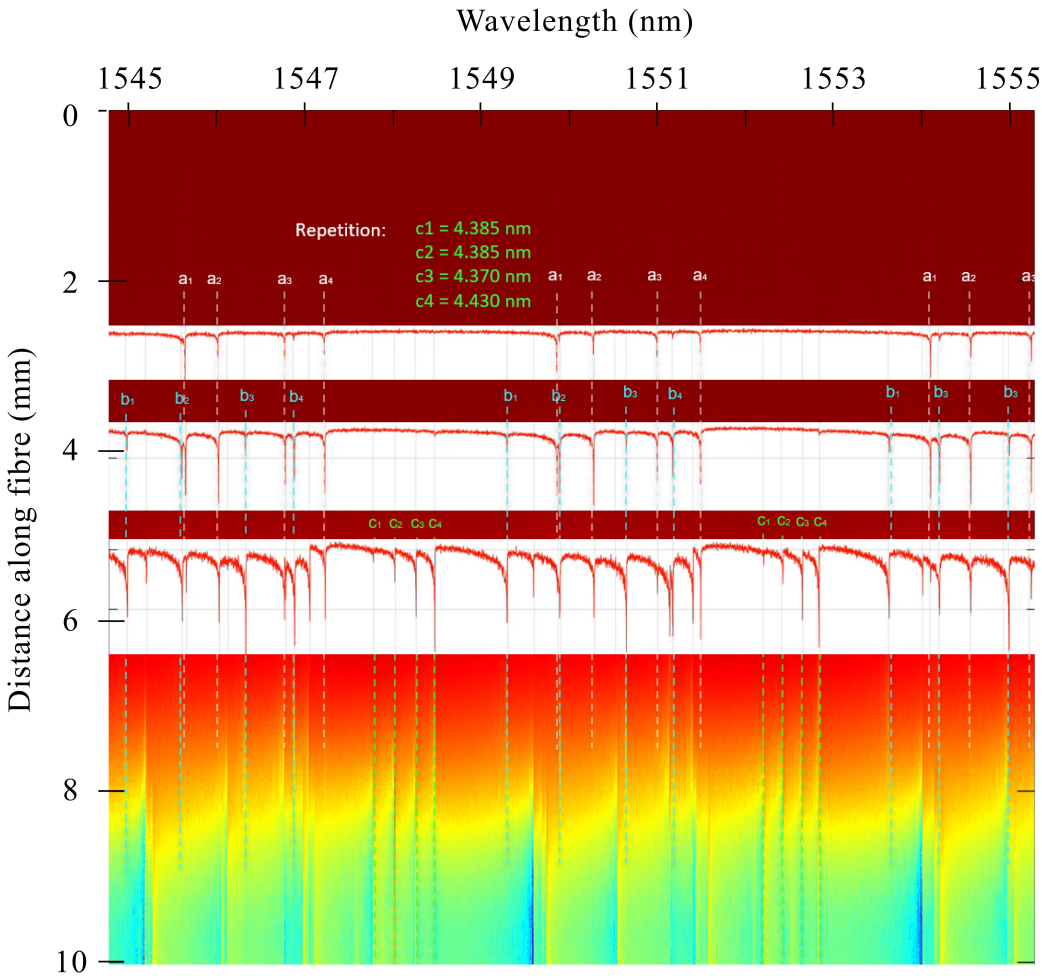

Figure 3.14: Third region, 5-3 mm from the middle of the taper, with the corresponding insertion loss diagram added.

On the figure, within the 5-3 mm range from the taper's centre, four additional cutoff wavelengths are noticeable, with a periodicity of 4.4 nm. As we move closer to this region, an increasing amount of light couples into the target fibre. This results in a more loss-laden background and resonance dips that are broader and less distinct.

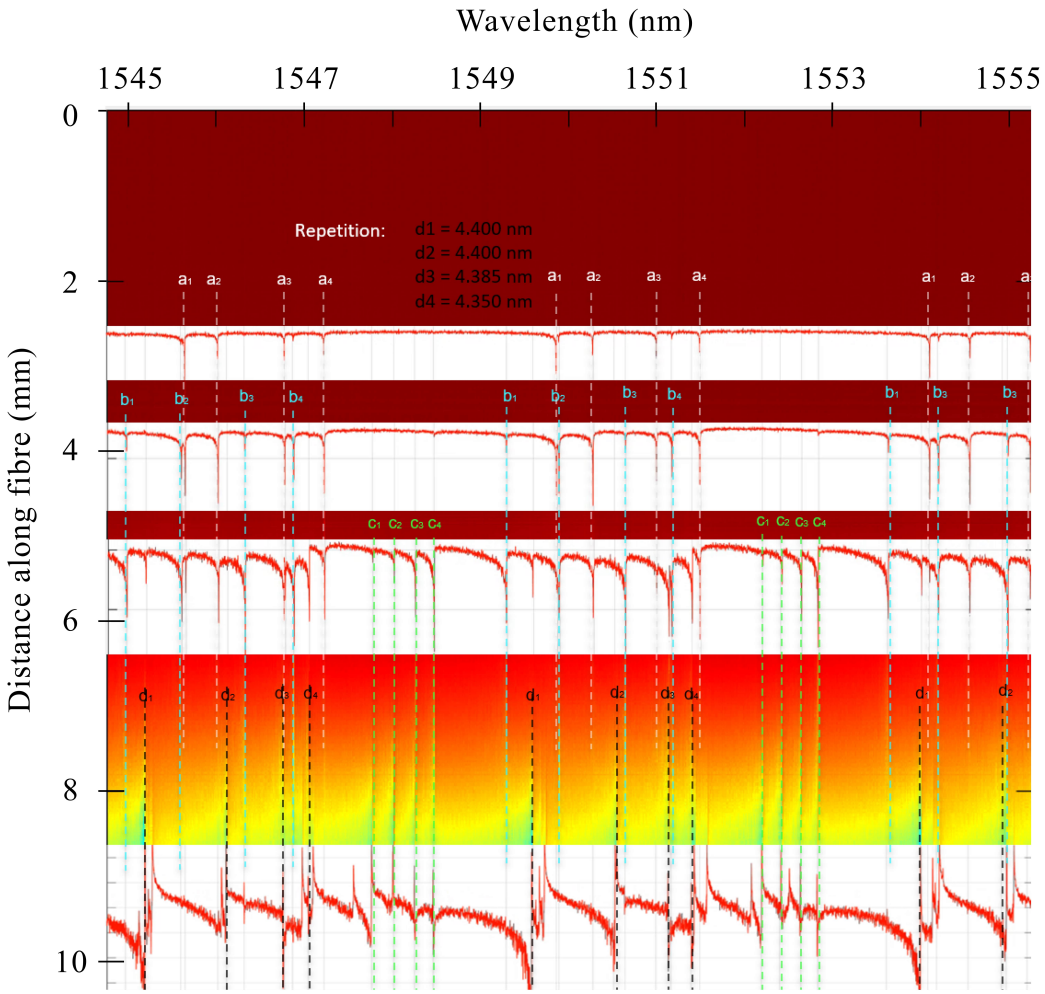

Figure 3.15: Fourth region, 3-0 mm from the middle of the taper, with the corresponding insertion loss diagram added.

The pattern continues with four more lines, however on the insertion loss insert we can see what appears like positive peaks. In the context of photonics, Fano resonances are observed in certain structures where a sharp resonance overlaps with a broader one, leading to an asymmetric lineshape in the transmission or reflection spectrum. This asymmetric profile is a hallmark of Fano interference and has been exploited in sensors, modulators, and other photonic devices due to its high sensitivity to changes in the system's parameters.

For the spectrograms discussed earlier, it's notable that the lines may exhibit a shift in wavelength when a different tapered fibre is utilized. However, the spacing between these lines remains consistent when using the same target fibre. For the experiments explored in this thesis, the taper's second region (7-5 mm from the centre) was used.

By characterizing the taper prior to experimentation, we can accurately pinpoint the cutoff wavelengths post-experiment. The subsequent image presents a spectrogram of the target fiber, showcasing an effective radius structure achieved through our Thermal Sculpting Method. The position along the taper is indicated with the corresponding insertion loss, helping to identify the cutoff wavelengths:

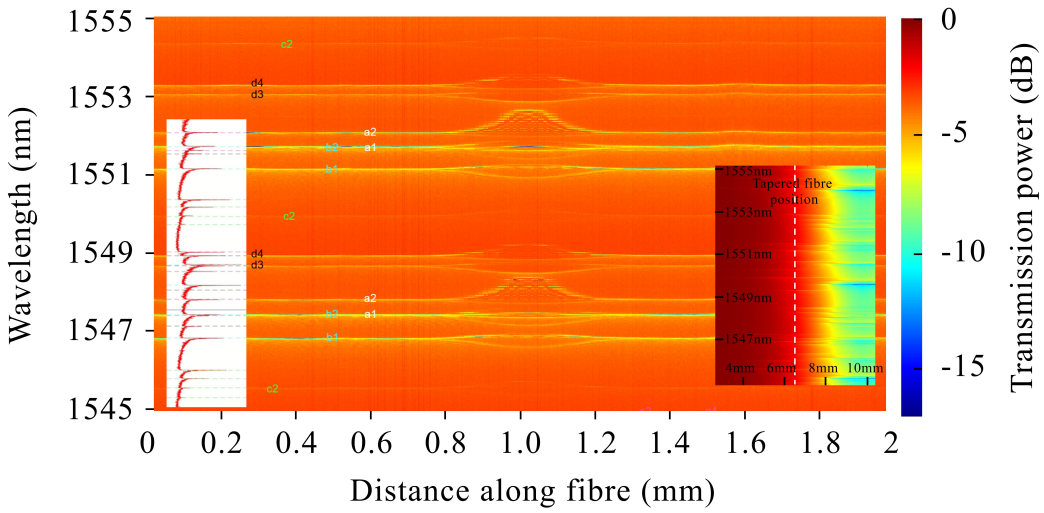

Figure 3.16: Spectrogram of an effective radius structure achieved through our Thermal Sculpting Method with the cutoff wavelengths identified thanks to the taper characterisation.

The line pattern observed in the insertion loss at the taper position serves a pivotal role in discerning the various cutoff wavelengths. This not only aids in a clearer understanding of the underlying spectral features but also bolsters the efficiency of characterizing our effective radius variation (ERV) engineering techniques.

3.3 Introduction

Whispering Gallery Mode (WGM) Optical Microresonators: One of the fascinating realms of optics revolves around whispering gallery mode (WGM) optical microresonators. These resonators allow light to circulate or "whisper" around a dielectric structure, hence the name. One commonly adopted technique to fabricate these microresonators is through the melting of silica fibres [9]. Over time, various methods have emerged to execute this melting process, including using a flame, a CO2 laser beam, an arc discharge, and even an electric heater [25], [26], [27].

The quest to achieve perfection in these resonators is often measured using the Q-factor. A higher Q-factor represents fewer energy losses. In some instances, melting-fabricated microresonators have astonishingly achieved Q-factors approaching 10^{10} [9]. However, no method is without its challenges. The precision with which we can reproduce this melting process typically hovers around a few microns [26]. One could argue that this level of precision leaves room for improvement.

Post-Processing Techniques: To enhance this precision, researchers have introduced post-processing techniques. For instance, hydrofluoric (HF) etching has been found to potentially refine the microresonator's surface potentially, leading to better accuracy [28], [29].

Impact on Spectral Characteristics: It's intriguing to note that even when WGM microresonators are shaped identically and made from the same material, their spectral characteristics can vary depending on the fabrication method. Etching, for instance, does not affect the bulk material's refractive index. However, methods like CO2 laser and flame heating do introduce variations to the refractive index.

The difference lies in how the optical material is heated: a laser beam heats from within, while a flame influences the external surface [30], [31]. These variances in heating techniques can result in different refractive index distributions, which in turn influence the WGMs in the microresonators.

Flame-Based Annealing: In this study, we have delved into the use of flame to locally anneal the optical fibre, presenting an alternative to the conventional melting approach. Remarkably, we discovered that annealing with a flame offers superior precision over melting. But why is this the case? Annealing serves to release the 'frozen-in' tension that gets introduced during the fibre drawing process. This release causes a much smaller deformation in the fibre material compared to when it is melted. Consequently, the effective radius of the fibre undergoes only nanoscale variations, accounting for changes in both its physical radius and refractive index. This fine-tuned process gives rise to a unique and shallow bottle microresonator termed the Surface Nanoscale Axial Photonics (SNAP) microresonator (SMR) [2], [23]. Over time, efforts to fabricate SMRs have adopted varied approaches, such as CO2 laser annealing [2], [23], femtosecond laser inscription [32], [33], slow cooking [34], and even etching [29]. Our contribution to this burgeoning field has been to advance a flame-based technique for SMR fabrication, boasting exceptional precision at the angstrom level.

WGM Cutoff Wavelengths and Applications: Another pivotal finding from our work pertains to the behaviour of WGM cutoff wavelengths. Specifically, we observed a strikingly unscalable behaviour of these wavelengths across different radial quantum numbers along the fibre length. Understanding and harnessing this behaviour is paramount for various applications.

3.4 Fabrication of SMRs

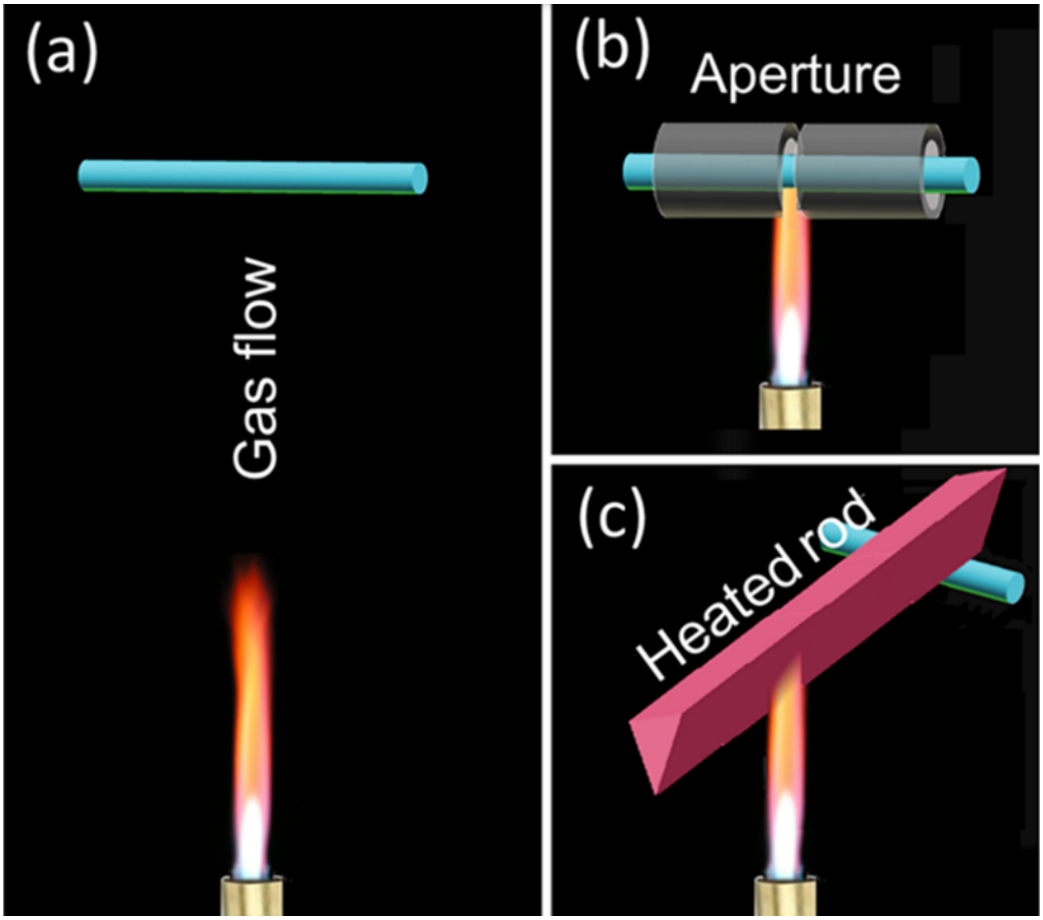

Figure 3.17: Methods employed in the fabrication of SNAP microresonators: **(a)** gas flow with direct flame heating, **(b)** flame confined through an aperture, and **(c)** flame heating without direct contact, taken from [4].

Experimental Setup Overview:

The equipment and setups used in our experiments are depicted in Figure 3.17. Central to all these setups is the use of a torch powered by a mix of butane and propane gases. We set up the apparatus such that the fibre segment remained horizontal while the flame was projected vertically. This configuration was essential

for precision and consistency in the annealing process.

Setup Descriptions:

Direct Flame Annealing (Figure 1(a)): The first setup, illustrated in Figure 3.17 (a), presents a straightforward annealing procedure. The optical fibre was positioned at a distance of 10 cm from the visible part of the flame. Here, the fibre isn't directly exposed to the flame but rather to the gas flow that's sufficiently heated from the flame. This localized flow of gas produces the necessary heat to induce the desired permanent change in the fibre's effective radius.

Aperture-aided Annealing (Figure 3.17 (b)): To refine our process, we introduced an aperture into the setup as shown in figure 3.17 (b). This aperture was crafted from sapphire tubes, boasting an outer diameter of 3 mm and an inner diameter of 1.2 mm. The aperture size for this specific experiment was set at 2 mm. Its role was crucial as it allowed us to reduce the length of the microresonator along the fibre's axis, thus offering more control over the annealing process.

Indirect Annealing via a Heated Metal Rod (Figure 3.17 (c)): Moving on to figure 3.17 (c), we employed a more indirect method of annealing [35]. Rather than using the flame or hot gas flow directly, an optical fibre was annealed through a metal rod that was previously heated by the flame. The advantage? This method considerably mitigated the disturbances from the gas flow, ensuring a more stabilized heating temperature. When fabricating the SMR, the fibre was moved at a speed of approximately 15-20 mm/s.

Translation of the Fibre:

In the setups outlined in figures 3.17 (a) to 3.17 (c), the fibre was moved at a consistent speed perpendicular to both its axial direction and the direction of the flame. This consistent speed meant that the fibre would be exposed to the heat for

only a brief moment—fractions of a second—as it traversed the hot zone.

However, a notable exception was observed in the setup shown in figure 3.17 (c). In this configuration, the fibre's movement was first parallel to the direction of the flame towards the heated rod and then immediately retraced its path away from the rod. Even with this different movement pattern, the time the fibre spent undergoing annealing remained roughly equivalent to the other methods.

3.5 Characterization of SMRs

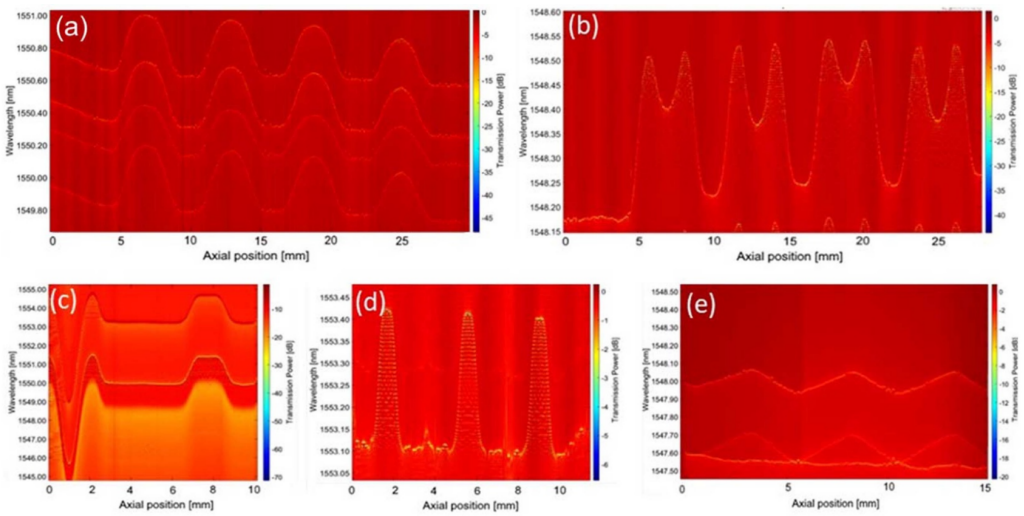

Figure 3.18: Spectrograms showcasing SMRs produced using the techniques depicted in Figure 1: **(a)**–**(c)** Heating through remote gas flow, **(d)** Heating via a flame within an aperture, and **(e)** Flame heating in an indirect manner.

Spectral Analysis Setup:

To assess the spectral characteristics of our fabricated SMRs, we utilized a biconically tapered optical fibre with a micron-scale waist, commonly referred to as a microfibre. This was connected to an optical spectrum analyzer (OSA), specifi-

cally, the Luna 5000 model. The microfibre was strategically positioned perpendicular to the fibre segments we were evaluating.

Scanning and Measurement Process:

During the characterization phase, the microfibre slid along the axis of the fibre. Throughout this translation, it would periodically come into contact with the fibre at specific, evenly spaced points [2], [23]. It was at these contact points where we measured the amplitude of resonant transmission through the SMRs. Our observations from these experiments are visualized in Figure 3.18.

Observations and Findings:

Spectrogram Interpretation: Figure 3.18 consolidates the results derived from the three fabrication approaches delineated in Figure 1. The presented spectrograms illustrate the transmission power spectrum, $P(z, \lambda)$, as it relates to the microfibre's position (z) along the SMR axis and the wavelength (λ). These spectrograms are crucial for they clearly indicate the WGM cutoff wavelengths. These wavelengths are not constant; rather, they fluctuate along the fibre axis and encapsulate the spectrum of the fabricated SMRs. With our OSA resolution standing at 1.3 pm, only the shorter SMRs, specifically those in figures 3.18 (b) and (d), displayed spectra that were clearly discernible.

Choice of Fibre: Different fibres were chosen for various experiments. A standard 125 μm fibre was employed for results captured in Figures 3.18 (a), (b), and (e). Meanwhile, a smaller 40 μm fibre was the choice for results in Figures 3.18 (c) and (d).

Specific Spectrogram Observations: Looking closely at the figures:

Figures 3.18 (a) to 3.18 (c) highlight spectrograms of SMRs that underwent distance annealing as depicted in Figure 3.17 (a). Specifically, figure 3.18 (a) pro-

vides insights into an "undersaturated" scenario where the inbuilt tension wasn't fully alleviated. Conversely, the SMR profiles in Figure 3.18 (b) indicate "oversaturation", a condition where the heating temperature surpasses the annealing threshold, leading to the fibre starting to soften and a dip in fabrication reproducibility. Figure 3.18 (c) showcases a flat SMR profile that's fully saturated [2]. Incorporating the sapphire tube aperture, as detailed in Figure 3.17 (b), granted us the ability to create shorter SMRs, the spectrogram of which is captured in Figure 3.18 (d). Upon contrasting these SMR spectrograms with that of an untouched fibre, we deduced that these SMRs were meticulously crafted with remarkable precision – 5 pm in terms of wavelength and an impressive 0.7 angstrom concerning the variation in the effective fibre radius. The Flame's Precision: The results conclusively showcased that the flame-based fabrication technique could attain angstrom-level precision when producing SMRs.

SMRs via Indirect Heating: Our subsequent endeavour was the fabrication of SMRs using indirect heating, following the blueprint provided in Figure 3.17 (c). Here, the resulting spectrogram (Figure 3.18 (e)) revealed an intriguing pattern: the axial profiles of cutoff wavelength variations related to diverse radial quantum numbers were entirely non-scalable. This manifested as a triangular-shaped variation in the cutoff wavelength for a specific series of WGMs, while other series remained largely unaffected by the annealing process. We surmise this unique outcome is attributed to the distinct spatial (aligned with the fibre's radial direction) and temporal fluctuations in the flame's heating power, as evident in Figure 3.18 (e). This phenomenon starkly contrasted with the patterns witnessed in Figure 3.18 (a) and the characteristics observed when internally heating with a CO2 laser beam [2], [23].

3.6 Discussion

Main Achievements:

A notable advancement in the fabrication of optical microresonators was achieved through the use of an elementary flame torch. This technique, seemingly simple in its application, has rendered the ability to craft microresonators with remarkable angstrom precision. The ramifications of this achievement are profound, as they herald a new era in the precision and efficiency of microresonator fabrication.

Characteristics of Fabricated SMRs:

The methodology we have pioneered produces SMRs that are distinguishable by their smooth, elongated profiles. Upon a more intricate examination of the SMRs — particularly those reflected in the spectrogram of figure 3.18 (a) (which isn't presented in this section) — an insightful observation emerged: the apexes of several of the fabricated SMRs are characterized by a rigorously defined parabolic contour. This precision in shaping is paramount for specific applications, notably in the realms of crafting minuscule delay lines [36] and frequency comb generators [37].

Comparison with SNAP Technology:

The advent of Surface Nanoscale Axial Photonics (SNAP) technology has been groundbreaking in its own right [32], [33], [34]. Yet, there remain certain challenges within this domain, particularly in the fabrication of specific SMR profiles. Our flame torch technique seems to offer a promising alternative or supplement to the existing SNAP methodologies, evident from the precision and efficacy we have observed.

Potential Applications:

The non-scalable behaviour of the cutoff wavelength, showcased in Figure 3.18 (e), unlocks potential avenues in the realm of all-optical manipulation. Here, the propagation dynamics of robust control pulses and their weaker counterparts could be directed by varying axial cutoff wavelengths [38], [39]. This implies that the flame torch technique could be pivotal in achieving nuanced control over the movement of whispering gallery light pulses.

Future Prospects:

Our sights are firmly set on refining and furthering this methodology. Upcoming endeavours will involve experimental enhancement and fine-tuning of the setups illustrated in figure 3.17. Furthermore, our research will be oriented towards modelling the transient heating processes that are invoked by the flame. These steps, we believe, will consolidate our approach's position at the forefront of SMR fabrication techniques.

4 | Method 2: Side-coupled optical fibres

In the preceding chapter, we demonstrated that light propagation in the form of a Whispering Gallery Mode (WGM) along an optical fiber surface can be manipulated by infinitesimal nanoscale alterations in the effective fiber radius [23]. Remarkably, even a nanometer-fraction deformation of the fiber can completely trap WGMs, creating a high-quality microresonator [2]. Such a variation in the fiber radius required to regulate WGMs is significantly less than the light's wavelength. Leveraging this principle, the Surface Nanoscale Axial Photonics (SNAP) platform facilitates the creation of resonant optical devices on the fiber surface with unparalleled sub-angstrom precision and minimal loss [40] [36].

The advancements outlined in the ensuing sections harness the potential of the SNAP platform, introducing a greater degree of adaptability. Whereas traditional SNAP relied on WGMs controlled by nanoscale deformation of the optical fiber's outer surface, our contribution extends this paradigm. We posit that certain structures can be conceived without necessitating any tangible deformation.

In our earlier discussions, we established that incorporating SNAP resonators is achievable through the deformation of the external surface and alterations in the bulk fibre's refractive index—permanent processes. Contrarily, we now propose a non-destructive approach that is both reversible and highly adjustable. Our findings suggest that WGMs traversing the microfiber can be influenced solely by coupling to another bent target fiber, wherein the control hinges on the bend's radius. We illustrate how such coupling can effectively trap WGMs and give rise to a superior optical microresonator. When the microfiber is translated along the target fibre, the resonator's spectra reveal a series of resonances. These are instrumental in ascertaining the contact region's dimensions and the ensuing effective radius

alteration. The capabilities of the optical spectrum analyzer deployed solely bind the precision of our quality factor measurements. This revelation sets the stage for a ground-breaking approach to SNAP resonator design and heralds a new era of adjustable resonant photonic instruments. The research discussed in this chapter was undertaken at the Aston Institute of Photonics Technologies (AIPT), Birmingham, UK and is adapted from the subsequent publication [5].

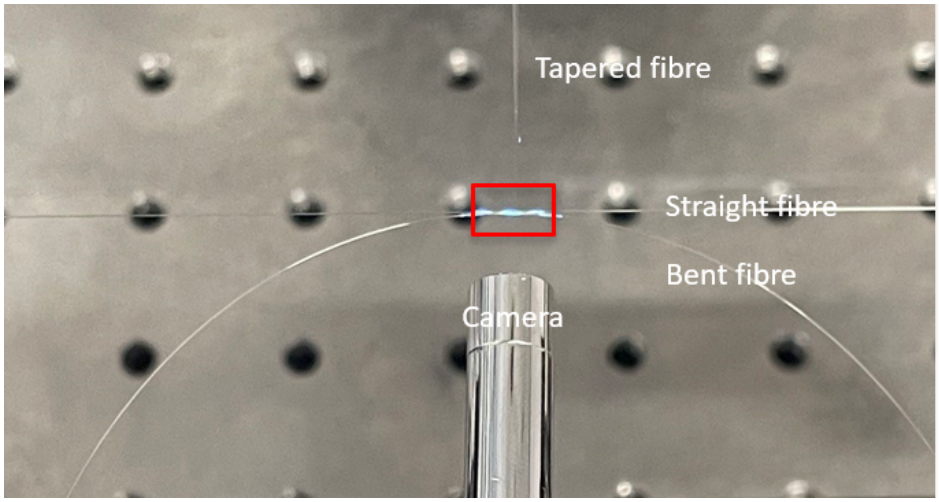

Figure 4.1: Experimental setup for Side-coupling optical fibres.

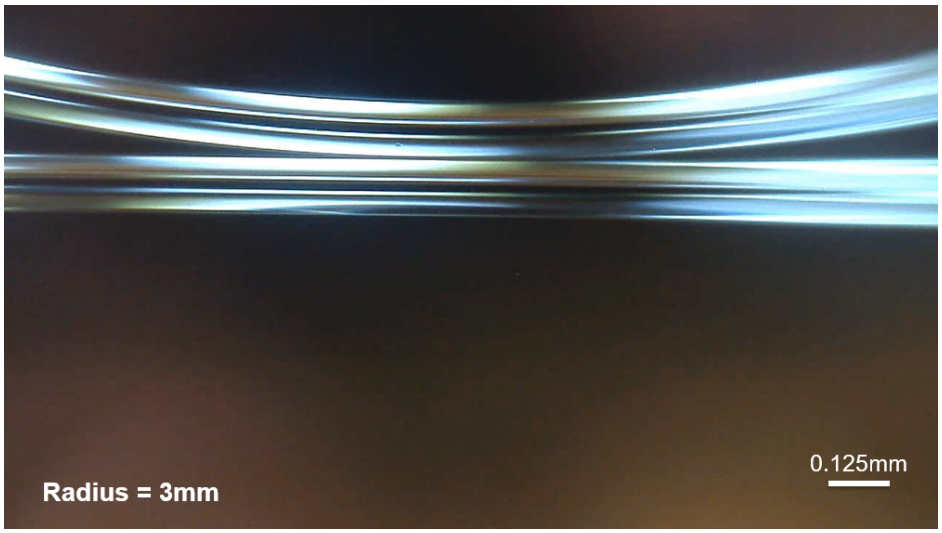

Figure 4.2: Close up of the contact point.

4.1 Significance

Monolithic Optical Microresonators and Their Significance:

Optical microresonators with high Q-factors (a parameter indicating the quality of the resonator) are pivotal components in numerous scientific and technological domains. These resonators are at the heart of innovations in classical and quantum optical signal processing, microwave photonics, and ultra-precise sensing. Beyond their technological applications, they also significantly advance our understanding of optical and physical sciences at a fundamental level.

Challenges with Traditional Microresonators:

Despite their broad utility, these monolithic optical microresonators have inherent limitations owing to their solid structure. One of the primary challenges has been the difficulty in adjusting their free spectral range (FSR) - a key parameter defining the frequency spacing between the successive resonances of the microresonator. Achieving tunability in FSR is vital for several applications, yet it remained an elusive feature for most monolithic microresonators until now.

Our Novel Approach: Side-Coupling of Coplanar Bent Optical Fibers:

This research presents a groundbreaking experimental approach to address this limitation. We discovered that by side-coupling coplanar bent optical fibres, we could induce a high Q-factor whispering gallery mode (WGM) optical microresonator.

The beauty of this method lies in its mechanical reconfigurability. By varying the curvature radius of these fibers — ranging from the scale of centimetres down to millimetres —we can craft optical microresonators whose dimensions span from millimetres to as fine as 100 microns. This adaptability further translates to an

FSR tunability that stretches from a picometre scale up to ten picometres.

Theoretical Framework and Experimental Validation:

We've also developed a comprehensive theoretical framework that elucidates the formation of these novel microresonators. Impressively, our theoretical predictions align reasonably well with the experimental data, showcasing the robustness of our model.

Potential Applications:

The potential applications for these new microresonators are vast and transformative. They promise advancements in cavity Quantum Electrodynamics (QED), microresonator optomechanics, and frequency comb generation with tunable repetition rates. Furthermore, they open doors to innovations in tunable lasing and optical pulses' adaptable processing and delay.

4.2 Introduction

Microphotonic devices serve as fundamental building blocks in the realm of optical technologies, playing pivotal roles in a vast array of applications [41], [42]. At their core, these devices consist of elements such as waveguides, which guide light along a specific path, couplers that facilitate light transfer between different pathways, and microresonators that selectively amplify or attenuate specific wavelengths of light.

Achieving optimal functionality for these systems necessitates adherence to certain non-negotiable criteria. Foremost among these is the need for impeccable precision in fabrication, as even minor deviations can impact performance or result in inefficiencies [42], [43]. Moreover, it's imperative that these devices operate with minimal losses to ensure the integrity of the signal's strength and quality. Beyond

these foundational requirements, the adaptability offered by tunability emerges as a game-changer, paving the way for a broader spectrum of applications [44], [45].

In the broader landscape of micro photonics, there's a delicate balance between complexity and simplicity. While the allure of complex tunable circuits, capable of a vast array of signal transformations, is undeniable [41], the elegance of standalone devices cannot be overlooked. For instance, tunable three-dimensional microresonators, despite their seeming simplicity, offer a range of unique functionalities that more intricate systems might struggle to replicate.

Efforts to enhance tunability in microresonators have led researchers down diverse paths. Whether dealing with spherical, toroidal, or bottle-shaped resonators, various techniques have been applied, such as mechanical stretching, heating, and the exploitation of nonlinear light effects [46], [47] [26] [48] [49]. Some of these ventures have even delved into the crafting of monolithic or specifically coated microresonators to access distinct properties. However, a recurring challenge across many of these methods is their limited tunability scope. While they allow adjustments in resonant wavelengths, the separation between them often remains rigid, posing challenges for applications needing more nuanced tuning capabilities.

Several applications in photonics underscore the significance of having microresonators that feature tunable eigenwavelength separation, particularly a tunable free spectral range. These applications span a range of fields including cavity QED [26], [50], [51], optomechanics [52], [53], frequency microcomb generation [54], [55], optical signal processing and delay [44], [45], [56], and lasing [57], [58], [59], [60].

A primary advantage of this tunability lies in the versatility it introduces. For instance, researchers can craft optical frequency microcomb generators and microlasers by manipulating the free spectral range. This allows for continuous

adjustments in both the repetition rate and wavelength. Furthermore, the capability to fine-tune the microresonator eigenfrequency separation in harmony with its mechanical oscillations' frequency opens up avenues for more advanced applications.

Attaining meaningful shifts in the eigenwavelength separation often demands significant modifications either in the microresonator's dimensions or its refractive index parameters. In many cases, these changes must be comparable to the original parameters of the microresonator, which presents challenges. A potential solution to this predicament lies in the realm of Fabry-Perot microresonators. By incorporating adjustable mirror separations and specifically housing optical materials of interest, these microresonators promise a degree of tunability [51], [60], [61].

Enhancing the flexibility of such tuning mechanisms takes innovation. Two approaches stand out in this regard. One involves designing Fabry-Perot microresonators that contain a liquid material [60], providing dynamic refractive index adjustments. In contrast, another technique strategically places a wedge-shaped solid optical material inside the Fabry-Perot microresonator [62]. Translating this material allows variably adjusting its dimensions, offering a unique pathway to modify the resonator's properties.

Another intriguing avenue to explore involves the challenge of achieving eigenwavelength separation tunability in three-dimensional monolithic high Q-factor microresonators. Specifically, those of spherical, toroidal, and bottle shapes are of great interest. The allure of these shapes extends beyond mere form, offering potential advancements to the burgeoning applications of such microresonators. As mentioned earlier, these encompass realms like QED, optomechanics, lasing, and frequency comb generation.

But there's a significant roadblock when navigating this path. A primary obstacle arises from the inherent structure of these monolithic microresonators. Achieving the desired change in their eigenwavelength separation often necessitates deformation. Yet, deforming these microresonators, especially to the degree that would effect a considerable change, is a daunting challenge. In many cases, attempting such alterations proves unfeasible, given these devices' solid and intricately shaped nature.

This limitation poses a crucial question for researchers: How can one marry the inherent advantages of these three-dimensional structures with the desired tunability without compromising their integrity or performance?

Amidst the challenges associated with achieving tunability in three-dimensional monolithic microresonators, a shining exception emerges in the form of SNAP (Surface Nanoscale Axial Photonics) microresonators [13]. What sets these microresonators apart is their innovative fabrication technique. Rather than conventional means, SNAP microresonators come to life through the precise nanoscale deformation of an optical fibre's surface. This intricate process results in equally precise variations in the cutoff wavelengths (CWLs). It's these CWLs that regulate the slow propagation of the whispering gallery modes (WGMs) along the fibre's axis, a phenomenon elaborated upon in several studies [13], [63].

To better appreciate the potential of SNAP microresonators, consider the work presented in [64]. Researchers showcased a SNAP microresonator that not only was induced by localized heating of an optical fibre but was also fully reconfigurable. In another notable study, [33], the spotlight was on the feasibility of crafting a SNAP microresonator by locally bending an optical fibre. This study expanded on the theme by emphasizing control over the microresonator's dimensions through this bending mechanism. Both these methods underscored the abil-

ity to tune the eigenwavelength separation to degrees comparable to or even exceeding its original value.

However, no method is without its limitations. In these pioneering approaches, the resultant microresonator shapes weren't highly versatile. They exhibited characteristic axial dimensions that couldn't be shrunk below a few millimetres. This limitation stemmed from the length constraints posed by the characteristic heat distribution along the fibre for the microresonator induced by heating. In contrast, for the microresonator crafted by bending, the size reduction encountered barriers set by the smallest permissible curvature radius. Pushing this radius any further risks reaching the fibre's breaking point.

This work unveils a novel and groundbreaking variant of WGM optical microresonators that comfortably nestles within the SNAP microresonator family. One of the standout aspects of our research revolves around the innovative use of side-coupled coplanar bent fibres, as illustrated in Fig. 4.3. The design and alignment of these fibres play a pivotal role in inducing a high Q-factor SNAP microresonator. Remarkably, this microresonator becomes localized right at the point where the fibres couple.

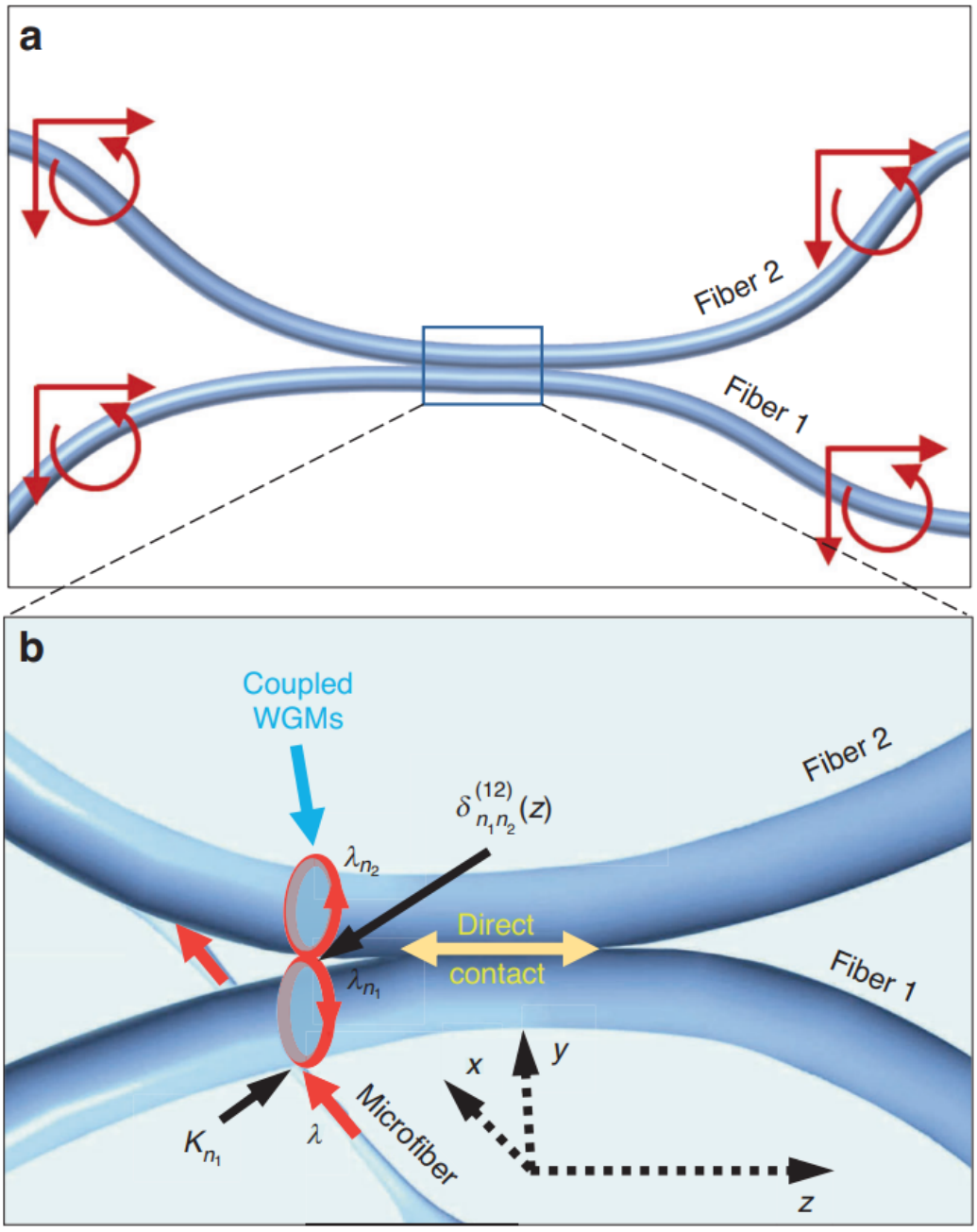

Figure 4.3: Optical fibres side-coupling configuration. **(a)** Bent optical fibres in a coplanar arrangement making contact. Fibre profile adjustments are achieved by bending and shifting the fibre tails, depicted by curved and straight arrows. **(b)** Schematic showing the interaction between the input-output microfiber and the WGMs in Fibre 1 and Fibre 2, particularly near their respective cutoff wavelengths. Image from [5].

Fig. 4.3 doesn't just serve as a mere illustration; it offers an insightful glimpse into the flexibility inherent in our approach. Leveraging this configuration, we can expertly modulate the shape of the ensuing SNAP microresonators. This configurational adaptability extends to their axial dimensions, too, allowing for a range that spans from the hundred-micron scale all the way to the millimetre scale. Such variability directly translates into our ability to fine-tune their eigenwavelength separation. In more precise terms, our methodology permits adjustments ranging from the ten-picometre scale right down to the singular picometre scale.

4.3 Results

4.3.1 CWLs behaviour in uncoupled and side-coupled straight fibres

To gain a comprehensive understanding of the behaviour of CWLs, it's essential to study them in both uncoupled and side-coupled straight optical fibres. We began by meticulously cleaving a 125-micron diameter, uncoated commercial optical fibre to facilitate this exploration. This division yielded two distinct sections, which we refer to as Fibre 1 and Fibre 2.

The next phase involved the precision alignment of these fibres. This meant ensuring that the fibres were coaxially positioned and in direct contact for an expanse of 3.5 mm. A visual representation of this alignment can be seen in Fig. 4.4 a.

Light's entry point into our system was through Fibre 1. To ensure efficient light transmission, we utilized a taper. This taper, distinctly characterized by its micrometre diameter waist, functioned as an input-output microfibre. Additionally, we employed an Optical Spectrum Analyzer (OSA) to refine the process further.

Once introduced into Fibre 1, the light embarks on a fascinating journey, gradually forming Whispering Gallery Modes (WGMs). These WGMs follow a determined trajectory, predominantly gravitating towards the surface of the fibre. The region where the two fibres intimately connect, as depicted in Fig. 4.4 a, becomes a focal point of activity. Within this juncture, a compelling interaction occurs. The WGMs established in Fibre 1 find their counterparts in Fibre 2, and, as a result, coupling between the WGMs of the two fibres takes place.

In our quest to effectively understand the implications of interfiber coupling, it was crucial to perform meticulous characterizations. As such, we embarked on the task of measuring the spectrograms associated with our meticulously arranged fibre system.

For this experiment, we relied on the input-output microfibre. With precision, this microfibre was gradually moved along the length of Fibre 1, a setup visually depicted in Figs. 4.3 b and 4.4 a. Ensuring utmost accuracy, we allowed it to touch Fibre 1 intermittently, maintaining a spatial resolution of precisely 2 μm. As the microfibre approached the termination of Fibre 1, we directed its movement toward Fibre 2, ensuring a continuous scanning process across this second fibre.

Our primary goal here was to capture comprehensive data. Thus, we measured the spectrograms of the transmission power, denoted as $P(\lambda, z)$. This measurement was undertaken with two variables in mind: the wavelength, represented by λ, and the microfibre's specific position, denoted by z, along the central axis of Fibre 1.

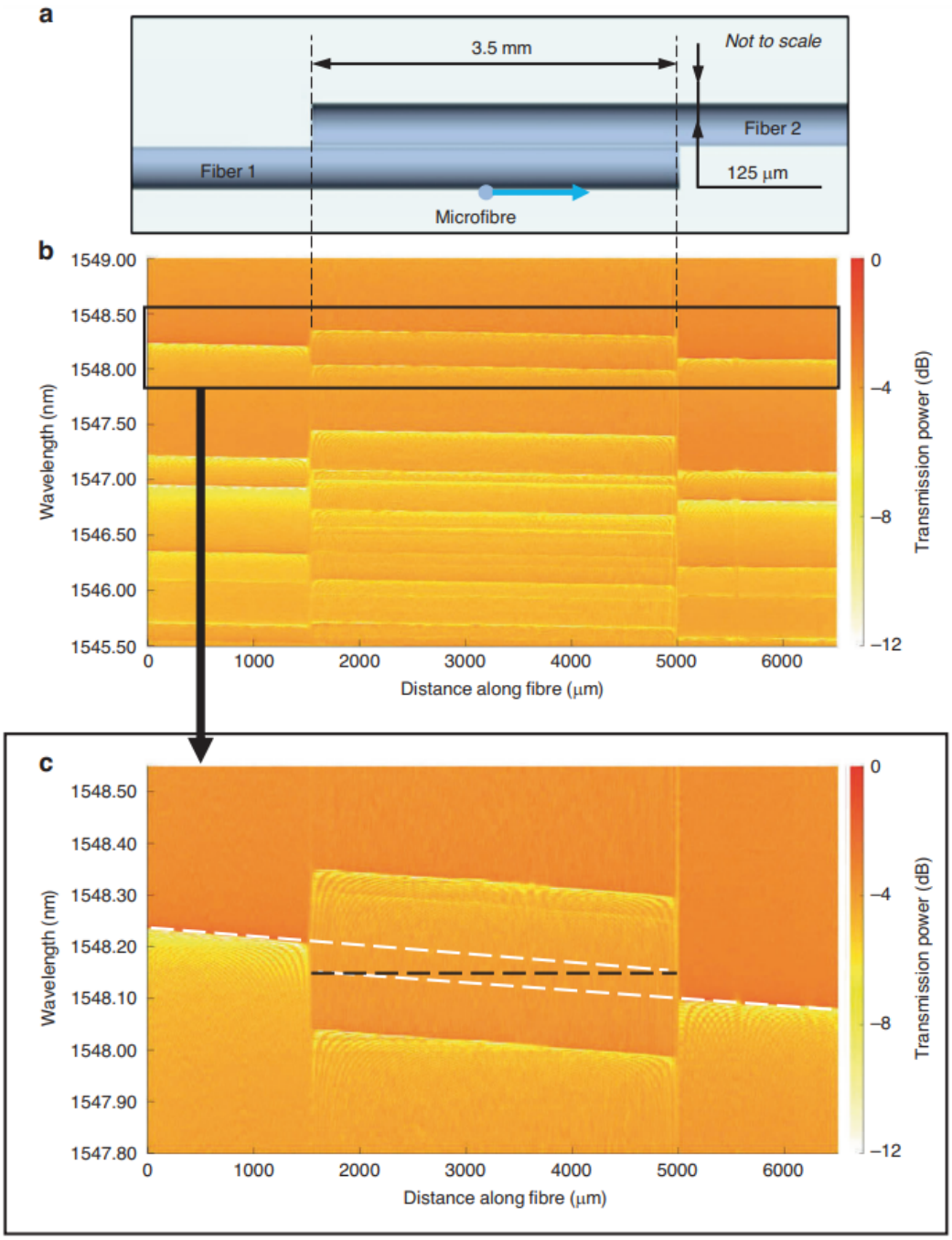

Figure 4.4: CWL divergence in side-connected straight optical fibres. **(a)** Representation of the side-attached straight optical fibre setup. **(b)** Spectral display of this setup. Spectrograms herein and in subsequent images are adjusted based on the output power's peak value in the spectrogram. **(c)** Enlarged segment highlighted in spectrogram **(b)**.

The spectrogram we obtained from our fibre system can be visualized in Fig. 4.4 b. On inspecting this figure, it's evident that the left and right segments of the spectrogram pertain to the uncoupled Fibre 1 and Fibre 2, respectively. Within the spectrogram presented in Fig. 4.4 b, discernible lines signify the CWLs associated with both uncoupled and coupled fibres. We must underscore that these CWLs are representative of WGMs, characterized by their distinct azimuthal and radial quantum numbers.

For a closer examination, we present an enlarged view of the section demarcated in Fig. 4.4 b, which can be seen in Fig. 4.4 c. Observing this magnified section, it becomes evident that the CWLs manifest as linear traces that are slightly slanted relative to the horizontal plane. We pinpointed the magnitude of this tilt from our measurements to be $\epsilon_t = 0.015$ nm/mm. Leveraging this, we computed the linear change in the fibre radius as $\Delta r_t = r_0\epsilon_t/\lambda_0 = 0.6$ nm/mm [65]. In this calculation, we employed values $r_0 = 62.5$ μm and $\lambda_0 = 1.55$ nm. By extending the CWLs of both Fibre 1 and Fibre 2 linearly, as visualized by the white dashed lines, it is reaffirmed that their intersections, marked by the horizontal black dashed line, align perfectly at the termination points of these fibres.

Within the 3.5 mm contact zone, WGMs in Fibre 1 interact with those in Fibre 2, causing the associated CWLs to diverge. The layout and orientation of these CWLs in the contact region are influenced by the coupling strength, a topic that will be elaborated upon later. It's worth noting that the detected CWL separation, as seen in Fig. 4.4 c, approximates to 0.1 nm. This is consistent with typical CWL alterations in SNAP microresonators [13], [63]. The positive shift of CWL within the coupling area fosters the formation of a tunable microresonator, whose characteristics can be altered by modifying the length of the side-joined fibre section.

In our recent tests, the Q-factor of the spawned SNAP resonator was subpar, a

consequence of light scatter at the fibre ends that weren't neatly severed, typically yielding about 70% WGM reflectivity [66]. Nonetheless, we advocate for the potential application of this resonator in the fabrication of compact, widely adjustable optical delay lines. This expands upon our earlier findings with fixed-dimension SNAP microresonators [36], [29]. In such an apparatus, WGM pulses navigate the fibre axis just once. As a result, light losses at the fibre terminations may only curtail the emitted light intensity by a ballpark figure of 50%. Additionally, we posit that with appropriate modifications, the Q-factor of these microresonators could be appreciably augmented, a matter to be discussed in subsequent sections.

4.3.2 Basic experiment

In our preliminary tests, commercial silica optical fibres with a diameter of 125 microns were used, making contact as depicted in Fig. 4.3 a. To achieve the desired contour near the coupling region (illustrated in Fig.4.3 b), the ends of both Fibre 1 and Fibre 2 were manipulated. These fibres were either originally linear or had been subjected to heat for permanent bending. As mentioned earlier, WGMs were introduced into Fibre 1 via a laterally oriented microfibre linked to the OSA. Given a sufficiently narrow gap between Fibre 1 and Fibre 2, WGMs transition from the former to the latter.

For the most rudimentary configuration explored here, Fibre 1 remained straight while the adjacent Fibre 2 exhibited a curve. The fibres were made to touch and then pressed closer to augment the coupling area. An actual image of the fibres arranged for this experiment is presented in Fig. 4.5 a. Analyzing this image, we deduced the bent fibre's curvature radius to be approximate $R \approx 30$ mm (further deliberations on the fibre profile will follow). Fig. 4.5 b offers the spectrogram of the established assembly, assessed over a 3.5 nm bandwidth spanning an axial

extent of 700 µm in Fibre 1. At the peripheries of this examination zone, where inter-fibre coupling is minimal, CWLs remain largely constant with respect to distance z, reflecting primarily the characteristics of Fibre 1. The distribution of CWLs in these areas mirrors what's seen in Fig. 4.4 b.

One of the critical highlights of our research becomes evident when focusing on the central portion of the spectrogram depicted in Fig. 4.5 b. A myriad of CWLs in this area demonstrates varying degrees of positive and negative shifts along the axial dimension, denoted as z. For clarity, we've zoomed into specific regions of this spectrogram, which can be examined more closely in Fig. 4.5 c and 4.5 d.

Upon inspection, the findings align with our initial hypotheses. Unlike the negative shifts, positive variations in the CWL result in the confinement of WGMs. This confinement mechanism subsequently gives rise to the formation of microresonators. A deeper dive into our calculations, which are conveniently represented in the inset of Fig. 4.5 c, suggests that the Q-factor of the microresonator we fabricated is rather remarkable. It's worth noting that the precise quantification of the Q-factor was constrained by the 1.3 pm resolution of the Optical Spectrum Analyzer (OSA) employed in our setup. Nevertheless, our estimates place this value in excess of 10^6.

The observed nuances in CWL fluctuations showcased in Fig. 4.5 c and 4.5 d aren't merely accidental artefacts. They are coherent with the underlying theory, which will be elaborated upon in the ensuing sections of this chapter.

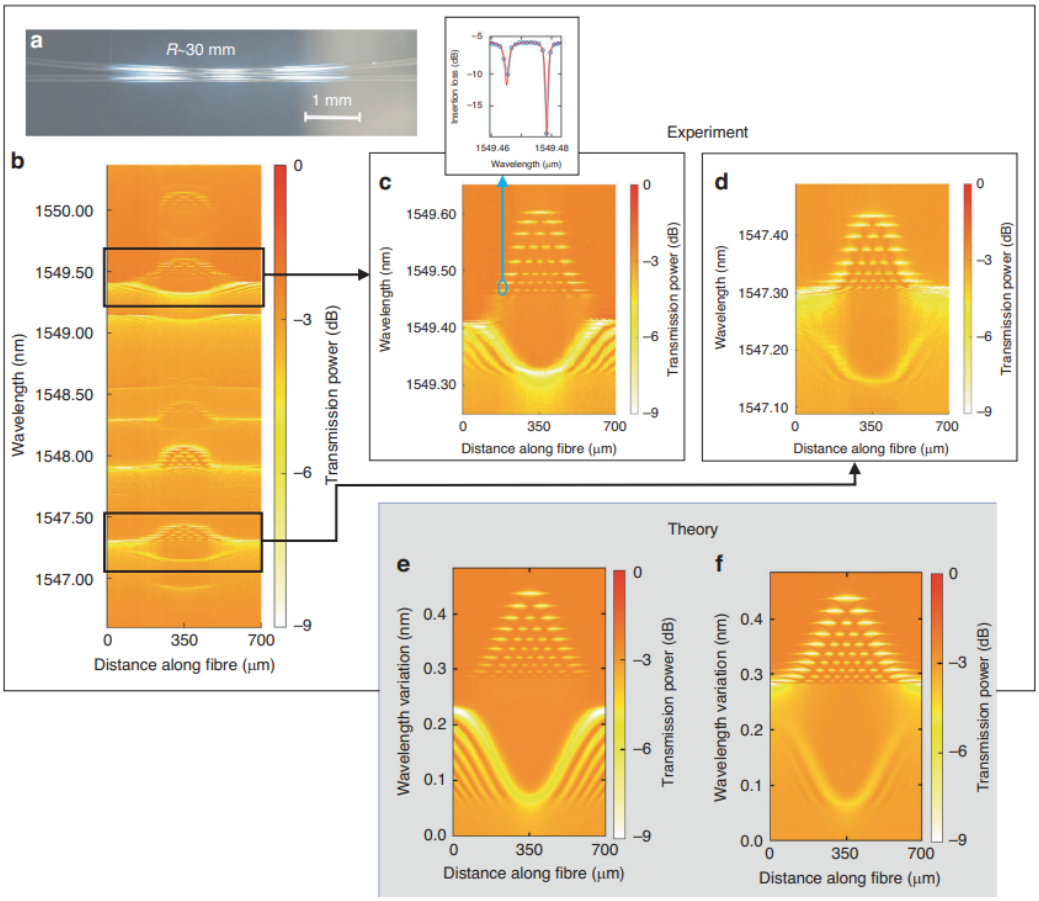

Figure 4.5: **Microresonators in side-coupled bent and straight optical fibers: empirical vs. theoretical results.** **(a)** Image of the side-connected fibers from the study. The top fiber has a curvature with a radius R of approximately 30 mm, while the bottom one exceeds a curvature radius of 1 m. **(b)** Spectral representation observed near these fibers' coupling area. **(c, d)** Spectrograms detailing the enlarged portions highlighted in spectrogram **(b)**. **(e, f)** Numerically derived spectrograms of the microresonators using the two-mode approach mentioned, mirroring the empirical spectrograms in Fig. **(c)** and **(d)** respectively. Image from [5].

4.3.3 Basic theory

We assume that the fibre bending is minimal, implying that light propagation along the axial direction of side-coupled fibres (Fig. 4.3 b) can be conceptual-

ized as traversing a singular waveguide. This waveguide exhibits an asymmetric cross-section that encompasses both fibres. The wavelengths of slow WGMs approach the CWLs $\lambda_n(z)$ of this combined waveguide. In order to deduce the complex-valued CWLs $\lambda_n(z)$, we introduce the foundational CWLs $\lambda_{1n_1} + \frac{i}{2}\gamma_{1n_1}$ and $\lambda_{2n_2} + \frac{i}{2}\gamma_{2n_2}$ of the unbent Fibre 1 and Fibre 2. Here, the imaginary portions are predominantly influenced by intrinsic material losses and scattering of light at the fibre surface.

Assuming there are N_1 and N_2 CWLs in Fibres 1 and 2, respectively, which are integral to resonant transmission, we can express $n_j = 1, 2, \ldots, N_j$ for $j = 1, 2$. The integers n, n_1, and n_2 are referred to as the transverse quantum numbers. The fluctuation in $\lambda_n(z)$ arises from fibre bending and is primarily driven by their mutual coupling in our setup [33].

In the scenario devoid of the input-output fibre, the CWLs of our system, $\lambda = \lambda_n(z)$, where $n = 1, 2, \ldots, N_1 + N_2$, are identified as the roots of the determinant:

$$\det(\lambda \boldsymbol{I} - \boldsymbol{\Xi}(z)) = 0 \tag{4.1}$$

Here $\boldsymbol{I}$ is the unitary $(N_1 + N_2) \times (N_1 + N_2)$ matrix and matrix

$$\boldsymbol{\Xi}(z) = \begin{bmatrix} \boldsymbol{\Lambda}_1 + \boldsymbol{\Delta}_1(z) & \boldsymbol{\Delta}_{12}(z) \\ \boldsymbol{\Delta}_{12}^{\dagger}(z) & \boldsymbol{\Lambda}_2 + \boldsymbol{\Delta}_2(z) \end{bmatrix} \tag{4.2}$$

includes submatrices determined by the original CWLs of Fibre 1 and Fibre 2, $\boldsymbol{\Lambda}_j = \{\lambda_{jn_j} + \frac{i}{2}\gamma_{jn_j}\}$, couplings inside each of the fibres caused by bending, $\boldsymbol{\Delta}_j(z) = \delta^{(j)}_{m_j n_j}(z)$, and interfere couplings $\boldsymbol{\Delta}_{12}(z) = \delta^{(12)}_{m_1 n_2}(z)$, $m_j, n_j = 1, 2, \ldots, N_j$.

As in SNAP [13], remarkably subtle variations in the nanometre and sub-nanometre scale of CWLs $\lambda_n(z)$ along the compound fibre waveguide can localize WGMs,

thereby inducing an optical microresonator with eigenwavelengths λ_{qn} possessing axial quantum numbers q. Given the gentle and minuscule variation in CWL and the closeness of the localized WGM wavelengths λ_{qn} to $\lambda_n(z)$, the corresponding eigenmode can be represented as:

$$E_{qn}(x, y, z) = \Psi_{qn}(z)\Omega_n(x, y, z)$$

In this expression, the transverse WGM distribution $\Omega_n(x, y, z)$ is calculated at the CWL $\lambda_n(z)$. This distribution exhibits a parametrically slow dependence on z [67]. Moreover, the function $\Psi_{qn}(z)$ delineates the axial variation of the microresonator eigenmode amplitude and adheres to the one-dimensional wave equation [13].

$$\frac{d^2\Psi_n}{dz^2} + \beta_n^2(z, \lambda)\Psi_n = 0, \quad \beta_n(z, \lambda) = \frac{2^{3/2}\pi n_r}{\lambda_n^{3/2}}\sqrt{\lambda_n(z) - \lambda} \tag{4.3}$$

Where n_r is the refractive index of fibres

The coupling parameters $\kappa_{qn}(z)$ between WGM $E_{qn}(x, y, z)$ and the input-output wave in the microfibre are ascertained by their overlap integral. The microfibre diameter is typically considerably smaller than the characteristic axial variation length of $E_{qn}(x, y, z)$. Consequently, mirroring the analogous approximation found in the SNAP platform [13], [68], the coupling parameters $\kappa_{qn}(z)$ correlate directly with the values of $E_{qn}(x, y, z)$ at the axial coordinate z of the input-output microfibre.

Subsequent calculations, rooted in the Mahaux-Weidenmüller theory [69], [70], [71], enabled us to represent the transmission power $P(\lambda, z)$ through the input-output microfibre connected to the fibre configuration shown in Fig. 4.3 b as:

$$P(z,\lambda) = \left| \frac{1 + \sum_{n=1}^{N_1+N_2} D_n^*(z) G_n(z,z,\lambda)}{1 + \sum_{n=1}^{N_1+N_2} D_n(z) G_n(z,z,\lambda)} \right|^2 \tag{4.4}$$

Here, $G_n(z_1, z_2, \lambda)$ denotes the Green's function of Eq. 4.3. Equation 4.4 generalises the expression for the transmission power, which was previously derived in Ref. [13]. As further shown below, functions $D_n(z)$ can be described and are characterised by values akin to the coupling D-parameters. These parameters have been previously measured experimentally and typically manifest real and imaginary parts approximately equal to 0.01 μm^{-1} [13],[68].

When conditions approach resonance, i.e., $\lambda = \lambda_{qn}$, and in instances where losses are minimally small, coupling is limited, and CWLs $\lambda_n(z)$ are isolated, solely one Green's function with the designated number n plays a role in the sums in Eq. 4.4. In such cases, Eq. 4.4 aligns with what was previously derived in Ref. [13]. Nonetheless, it's worth noting that, more often than not, the cumulative influence of multiple terms on the sums in Eq. 4.4 can be substantial.

Before diving into the in-depth examination of the spectrograms in Figs. 4.4 b and 4.5 b, it's imperative to note that the transmission power depictions in these figures shed light on the CWLs of the intertwined fibre system, as governed by Eq. 4.1, which are discerned by the input-output microfibre and, subsequently, the OSA. This means that the CWLs of Fibre 2, even though they are solutions to Eq. 4.1, remain obscured to the OSA when not coupled with Fibre 1. Intriguingly, the total number of CWLs that might emerge in the coupling vicinity could surge to as many as $N_1 + N_2$, notably eclipsing the N_1 number of discernible standalone CWLs of Fibre 1, as depicted in Fig. 4.4 b.

To shed light on the intricate dance of coupling between the WGMs in neighbour-

ing fibres, we steer our focus to the two-mode approximation, where $N_1 = N_2 = 1$. This is grounded on the assumption that the wavelength λ of the input illumination closely trails an unperturbed single WGM CWL $\lambda_{11} + \frac{i}{2}\gamma$ of Fibre 1 and a lone CWL $\lambda_{21} + \frac{i}{2}\gamma$ of Fibre 2, both sharing an identical imaginary component. Building on this, in Fig. 4.3 b, we now pivot to setting $n_1 = n_2 = 1$. Opting to set aside the effects propelled by the CWL variation owing to fibre bending [33], which generally takes a backseat compared to the more pronounced fibre coupling influence, we take $\delta_{11}^{(j)} = 0$. With these parameters in place, the CWLs $\lambda_1(z)$ and $\lambda_2(z)$ of the compound fibre, are found from Eq. 4.1 :

$$\lambda_{1,2}(z) = \frac{1}{2}\left(\lambda_{11} + \lambda_{21}\right) + i\gamma \pm \sqrt{\frac{1}{4}\left(\lambda_{11} - \lambda_{21}\right)^2 + \left(\delta_{11}^{(12)}(z)\right)^2} \tag{4.5}$$

Considering the dependence on the transverse coordinates x and y (as seen in Fig. 4.3 b), the method to determine the associated compound WGM corresponding to CWLs $\lambda_j(z)$ is detailed in the following manner.

We begin by defining the unperturbed WGMs in both Fibre 1 and Fibre 2. For this, it's essential to consider both fibres in their original state - unbent and not coupled. Calculated at their respective CWLs λ_{11} and λ_{21}, these are represented as $\Omega_1^{(1)}(x, y)$ and $\Omega_1^{(2)}(x, y)$.

Moving forward with the two-mode approximation, the generated compound modes due to the weak coupling between $\Omega_1^{(1)}(x, y)$ and $\Omega_1^{(2)}(x, y)$ can be defined. Specifically, they are described based on previous research [72], as:

$$\begin{aligned} \Omega_1(x, y, z) &= \cos(\alpha)\Omega_1^{(1)}(x, y) + \sin(\alpha)\Omega_1^{(2)}(x, y) \\ \Omega_2(x, y, z) &= \sin(\alpha)\Omega_1^{(1)}(x, y) + \cos(\alpha)\Omega_1^{(2)}(x, y) \\ \tan(2\alpha) &= \frac{2\delta_{11}^{(12)}(z)}{\lambda_{11} - \lambda_{21}} \end{aligned} \tag{4.6}$$

Consequently, the coupling parameters to the microfibre entering Eq. 4.4 at coordinate z are:

$$D_{1,2}(z) = \frac{D}{2}(1 \pm \frac{\lambda_1 - \lambda_2}{\sqrt{(\lambda_1 - \lambda_2)^2 + 4(\delta_{11}^{(12)}(z))^2}}) \tag{4.7}$$

In the aforementioned equations, the parameter D stands as a significant entity. This D represents a coupling parameter that remains independent of z. Notably, it governs the connection between the input-output microfibre and Fibre 1 [13], [68].

The axial profile $h(z)$ refers to the axial bending profile of optical fibers, describing how the fibers' bending curvature changes along their longitudinal axis, z. This profile is crucial for the creation and tuning of whispering gallery mode (WGM) microresonators induced by the side-coupling of bent optical fibers. The variation in $h(z)$ directly influences the coupling of light between fibers and the formation of microresonators with high quality factors (Q-factors), impacting their optical properties such as tunability and resonance. The unit of $h(z)$ in this context is length, typically micrometers (μm), denoting the precise geometric adjustments needed to manipulate the fibers' optical characteristics for applications in photonics.

To advance our understanding of how the axial profile $h(z)$ of the bent fibre translates to the CWL envelope profiles of the induced microresonators, it's crucial to pinpoint the relationship binding $h(z)$ and the coupling coefficient $\delta_{11}^{(12)}(z)$. Drawing inspiration from the methodologies employed in previous studies [73], [74], especially for the scenarios where $h(z)$ is both smooth and minor, we deduce the following relationship:

$$\delta_{11}^{(12)}(z) = \delta_0 \exp\left(-\frac{2\pi}{\lambda}(n_r^2 - 1)^{1/2} h(z)\right) \tag{4.8}$$

δ_0 remains independent of z. Assuming the simplest profile of the bent fibre having the curvature radius R, as:

$$h(z) = \frac{z^2}{2R} \tag{4.9}$$

For silica fibres where $nr = 1.44$, the full width at half maximum (FWHM) of $\delta_{11}^{(12)}(z)$ is estimated to be $z_{\text{FWHM}} \approx 0.5(\lambda R)^{1/2}$. Given $\lambda \approx 1.55\mu m$ and $R \approx 30$mm from our experimental setup, this results in $z_{\text{FWHM}} \approx 100\mu m$.

From Eqs. (5) and (8), the FWHM of the CWL, contingent upon the value of $\lambda_{11} - \lambda_{12}$, ranges between z_{FWHM} and $2z_{\text{FWHM}}$. This comparison is qualitatively consistent, albeit not exactly, with the microresonator FWHM $z_{\text{FWHM}} \approx 250\mu m$ observed from the experimental data presented in Fig. 4.5 c and d.

Our numerical modelling, executed within the confines of the two-mode approximation as guided by Eqs. 4.3–4.9, is depicted in Fig. 4.5 e and f. In order to align with the experimental observations, we assigned the mean CWL as $0.5(\lambda_{11} + \lambda_{12}) = 1.55\mu m$, the CWL discrepancy as $\lambda_{11} - \lambda_{12} = 0.05$nm for Fig. 4.5 e and $\lambda_{11} - \lambda_{12} = -0.05$nm for Fig. 4.5 f. Other parameters such as the coupling value were set to $D = -0.01 + 0.01i\mu\text{m}^{-1}$ [refs. [13], [68]], with a Q-factor $Q = 10^6$. Both the microresonator FWHM $z_{\text{FWHM}} \approx 250\mu m$ and its spectral amplitude, approximately 0.15nm, were adjusted to mirror the results from Fig. 4.5 c and d.

A comparative analysis of experimental spectrograms (Fig. 4.5 c, d) and theoretical predictions (Fig. 4.5 e, f) reveals remarkable similarities. Yet, critical

disparities merit attention. By referencing Eqs. 4.8 and 4.9, a FWHM value $z_{\text{FWHM}} \approx 250\mu m$ translates to a curvature radius $R \approx 66$mm for Fibre 2. This value is double of what has been ascertained from the visual representation in Fig. 4.5 a.

One plausible explanation for this discrepancy is that Fibre 2 deviates from a parabolic contour within the coupling region. Additionally, misalignments of the fibre may contribute to this disparity. External factors like electrostatic attraction and exerted pressure, which remain indiscernible in Fig. 4.5 a, might introduce deformations to the fibres. This hypothesis finds credence in the observed experimental profiles of the microresonator envelopes and CWL shapes in Fig. 4.5 c and d: relative to their theoretical counterparts in Fig. 4.5 e and f, they exhibit pronounced side slopes and present a flatter central region.

Furthermore, the theoretical spectrograms show CWL wavelength profiles displaying a greater degree of mirror-symmetry to the microresonator envelopes, especially concerning the horizontal alignment (as per Eq. 4.5). In contrast, the experimental spectrograms reveal that the lower CWL profiles have a diminished depth when compared to the microresonator envelopes. A potential rectification for this divergence could involve accounting for interactions with other WGMs, an aspect overlooked in our current two-mode approximation.

4.3.4 Tunability

By manipulating the tails of Fibre 1 and Fibre 2—when they were side-coupled as depicted in Fig. 4.3 —we achieved precision in tuning the dimensions of the fibre coupling region, enabling us to regulate the dimensions of the resultant microresonators. Our experimental setup primarily utilized 125 μm optical fibres.

Our exploration covered a spectrum of microresonator sizes. At the smallest

scale, we examined microresonators with only a handful of wavelength eigenvalues and characteristic axial dimensions approximating a few hundred microns, as evidenced in Fig. 4.6 a. Mid-range sizes spanned several hundreds of microns, showcased in Fig. 4.6 b and 4.6 c. At the other end of the spectrum, the largest microresonator we observed extended an axial length reaching 5 millimetres, detailed in Fig. 4.6 d.

For a more detailed inspection, the spectrograms presented in Fig. 4.6 are provided in an amplified format in figures 4.7 to 4.10. This section also contains sample plots of transmission spectra derived from the mentioned spectrograms, observed at varied points along the fibre axis. Additional figures within the same section furnish insets that depict transmission power resonances when positioned near the nodes of WGM eigenstates. Notably, the characteristic widths of these resonances indicate that the Q-factor of the microresonators we fabricated seems unaffected by the bending radius R. In fact, the values observed align with, or even exceed, 10^6.

In our examination of the smallest microresonators, we carefully observed their formation. By side-coupling a straight Fibre 1 with a bent Fibre 2, which had a notably small curvature radius of approximately 1 mm, we noticed only minor perturbations in the CWLs, as demonstrated in Fig. 4.6 a(I). As we incrementally increased the fibre radius, we ultimately produced a microresonator characterized by a singular eigenwavelength, depicted in Fig. 4.6 a(II). The zoomed-in section within this spectrogram reveals that the axial measurement of the associated eigenmode is around 200 µm.

Notably, aside from the consistent axial measurements of localized WGMs observed in specialized bat microresonators, as described in references [39,40], this dimension stands out as the broadest Full Width at Half Maximum (FWHM) of the

WGM amplitude antinode area ever recorded in microresonators. We assessed the Q-factor of this particular microresonator to exceed 10^6, though it's worth noting that the precision was constrained by the 1.3 pm resolution of our OSA.

Further observations include a comparison of the spacing, $\Delta\lambda_{01}$, between the fundamental eigenwavelength and the second axial modes of microresonators. As displayed in Fig. 4.6 a(II) and Fig. 4.6 a(III), we discerned a spacing of 34 pm and 35 pm, respectively. This comparison underscored an interesting phenomenon: while the CWL height of the microresonator amplifies with an increase in the bent fibre radius R, the $\Delta\lambda_{01}$ value, indicative of the local CWL behaviour at the microresonator's peak, remained virtually constant.

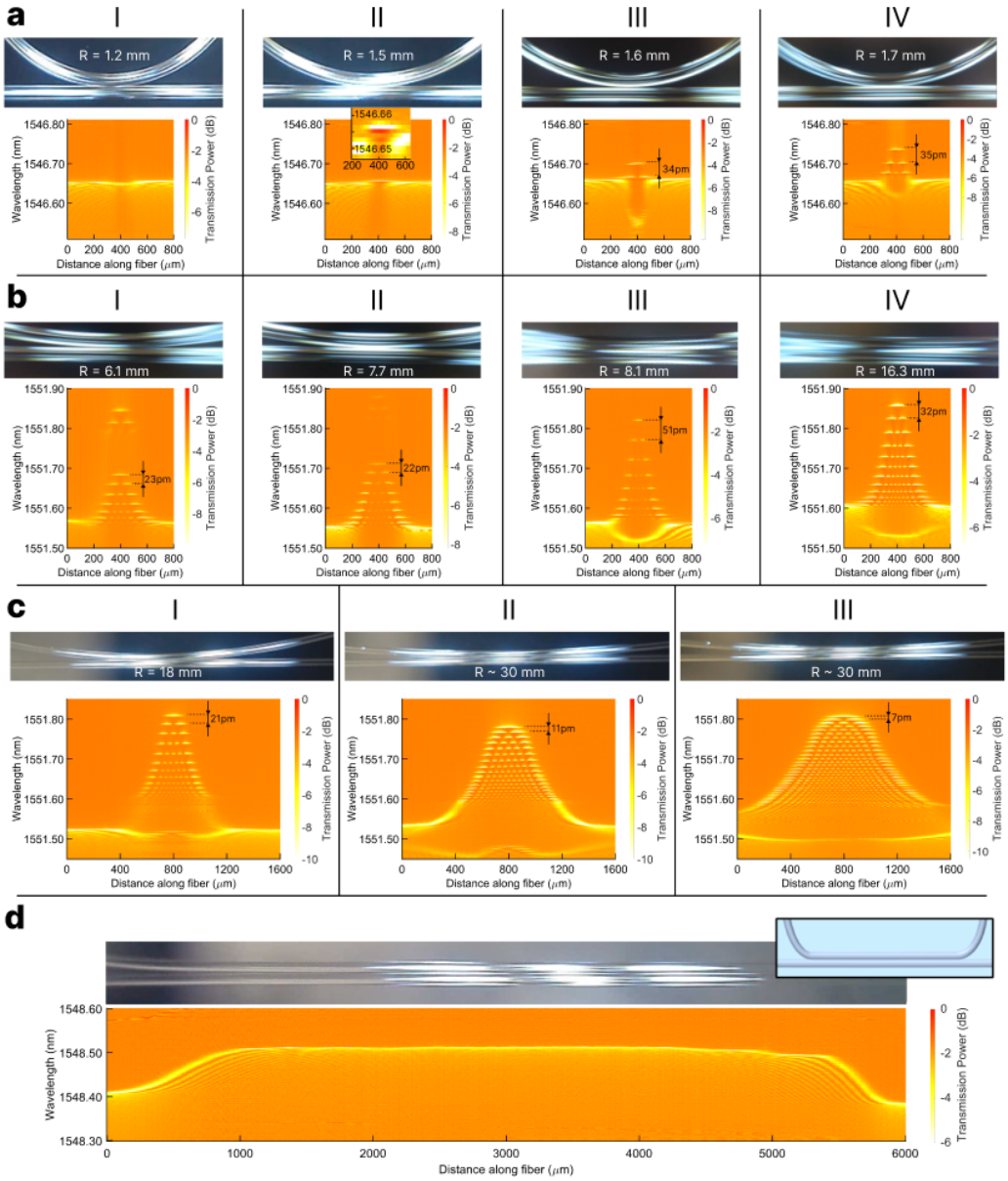

Figure 4.6: Tunability of Microresonators. **(a)** Spectrograms of induced microresonators with a 1.2 to 1.7 mm curvature radius for Fibre 2. **(b)** Spectrograms for a 6.1 to 16.3 mm curvature radius of Fibre 2.**(c)** Spectrograms for a 18 to 30 mm curvature radius of Fibre 2. **(d)** Spectrogram of a 5 mm microresonator, induced by connecting straight Fibre 1 and pre-bent Fibre 2, as shown in the inset. Image from [5].

For larger bending radii of Fibre 2, around 10 mm, microresonators with axial di-

mensions on the order of millimeters were formed, as depicted in Fig. 4b and 4c. Just as observed in Fig. 4.6 a, the CWL height of the microresonator increased proportionally with the radius R. However, the eigenwavelength spacing $\Delta\lambda_{01}$ exhibited an intriguing behavior. In Fig. 4.6 b, it first diminishes with an increasing R (contrasting Fig. 4.6 b(I) and 4.6 b(II)), then escalates in tandem with R (seen in Fig. 4.6 b(III)), only to decrease again as illustrated in Fig. 4.6 b(IV). Notably, $\Delta\lambda_{01}$ reaches a peak of 51 pm in Fig. 4.6 b(III).

We hypothesize that the oscillatory trend of $\Delta\lambda_{01}$ with respect to R might be attributed to local fibre deformations stemming from factors like electrostatic fibre attraction and physical pressure. The non-parabolic alteration in the CWL of the presented microresonators manifests as an inconsistency in their Free Spectral Range (FSR). In some instances, such as Fig. 4.6 c, the FSR appears relatively constant, suggesting potential applications like tunable optical frequency comb generation.

Furthermore, the two-mode approximation previously discussed doesn't precisely represent the behaviour observed in most of these spectrograms. A particularly intriguing observation can be seen in Fig. 4.6 c(II). At an initial glance, the microresonator's envelope in this figure seems to extend the CWL of Fibre 1 (in line with Fig. 4.5 c, d). However, against expectations, the axial WGM localization within this microresonator quickly fades within its domain. Providing a comprehensive theoretical interpretation of this phenomenon goes beyond the focus of our current discussion.

To fabricate longer microresonators, we initially bent the tails of Fibre 2, as depicted in the inset of Fig. 4.6 d. This procedure facilitated achieving this fibre's arbitrarily vast curvature radius, encompassing its straight formation amidst the bent tails. For instance, Fig. 4.6 d displays the spectrogram of a microresonator with

a length of 5 mm. Although the width of this microresonator's eigenwavelength surpasses its free spectral range, categorizing it amongst the white light WGM resonators, we postulate that its Q-factor is analogous to the smaller microresonators presented in Figs. 4.5 and 4.6, diverging from the lossy microresonators produced by side-coupled, cleaved, straight fibres, as seen in Fig. 4.4.

4.4 Discussion

The high Q-factor WGM tunable optical microresonators introduced in this study offer numerous intriguing possibilities and applications. Enhanced tuning versatility can be realized by varying boundary conditions at the fibre ends, as seen in Fig. 4.3 a, altering interfiber stresses, or modifying initial permanent fibre bends. A promising avenue for future research is designing and implementing advanced systems that build upon our initial setup, aiming for improved flexibility and the precise reproduction of microresonators with predefined spectra.

Fibre configurations, promising for future research and applications, can be developed from silica fibres, as explored in this study, and other materials like microcapillary fibres and high nonlinearity fibres. The technique of side-coupling bent fibres and WGM microresonators offers the potential for microresonator tuning. Incorporating multiple side-coupled straight, bent, and twisted optical fibres could introduce a new class of photonic molecules [75].

Based on two coupled CWLs, our model provides a qualitative understanding of some experimental spectrogram features. However, a comprehensive theory is warranted, accounting for multiple coupled CWLs and advancing the coupled wave theory. This would involve a detailed electromagnetic theory for coupled fibre configurations, encompassing aspects of coupling, surface scattering losses [73], [3], [76], and even a description of fibre profiles in the coupling region.

Future theories should relate fibre deformations to forces and moments applied to fibre tails, including electrostatic fibre attraction effects.

We posit that the Q-factor of the microresonators we demonstrated, currently measured around 10^6, could surpass 10^8 if fixed submicron-wide gaps are introduced between coupled fibres [26]. While Q-factors of this magnitude aren't essential for a variety of tunable resonant optical microdevices, such as delay lines [36], signal processors [63], and microlasers [58], [59], [60], they play a pivotal role in the development of frequency comb generators with adjustable repetition rates [54], [55], [37] and are significant for applications in cavity QED [26], [50], [51] and optomechanical domains [52], [53].

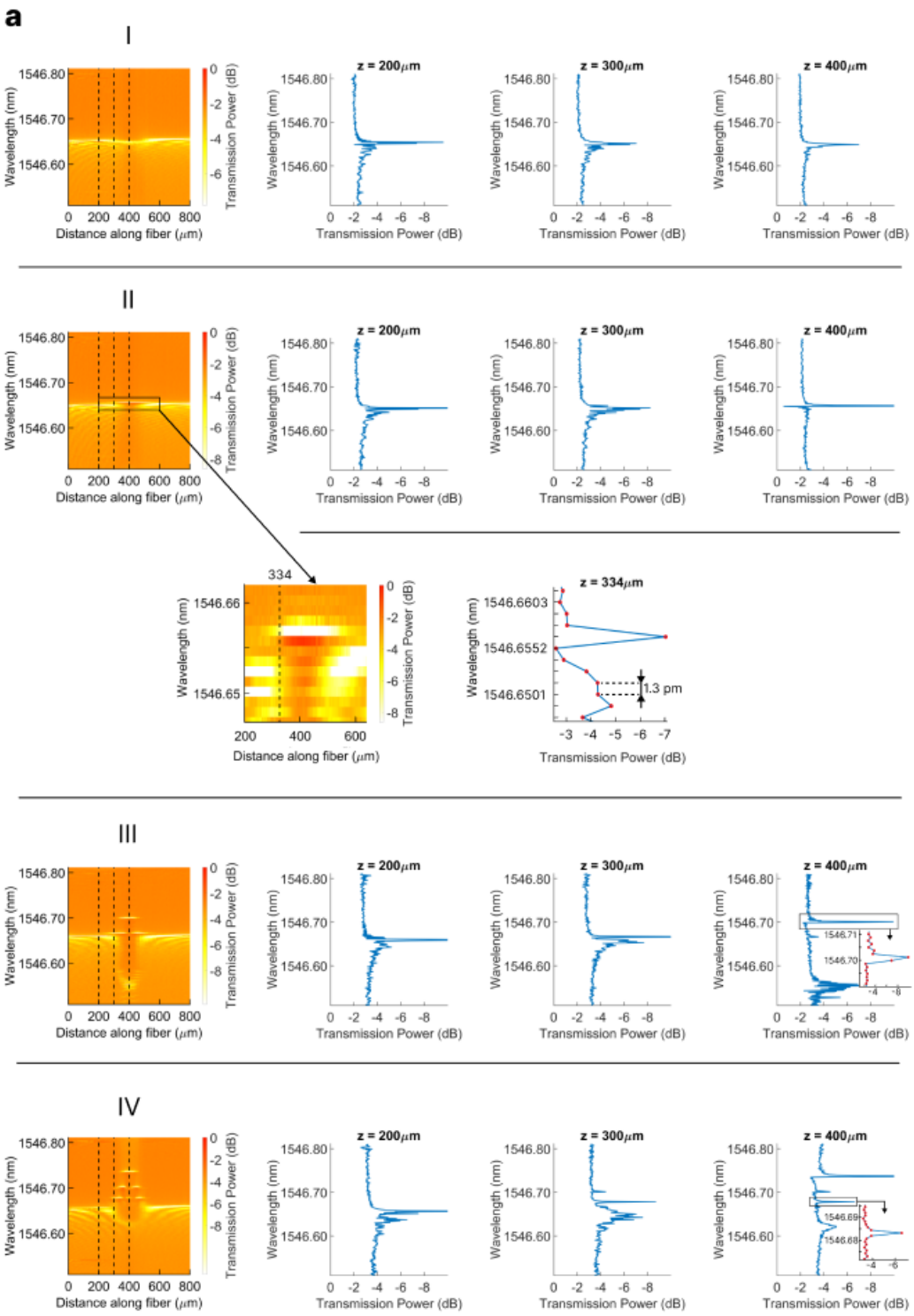

Figure 4.7: Transmission Power diagrams at several locations of interest in the spectrograms a From Fig 4.6. Image from [5].

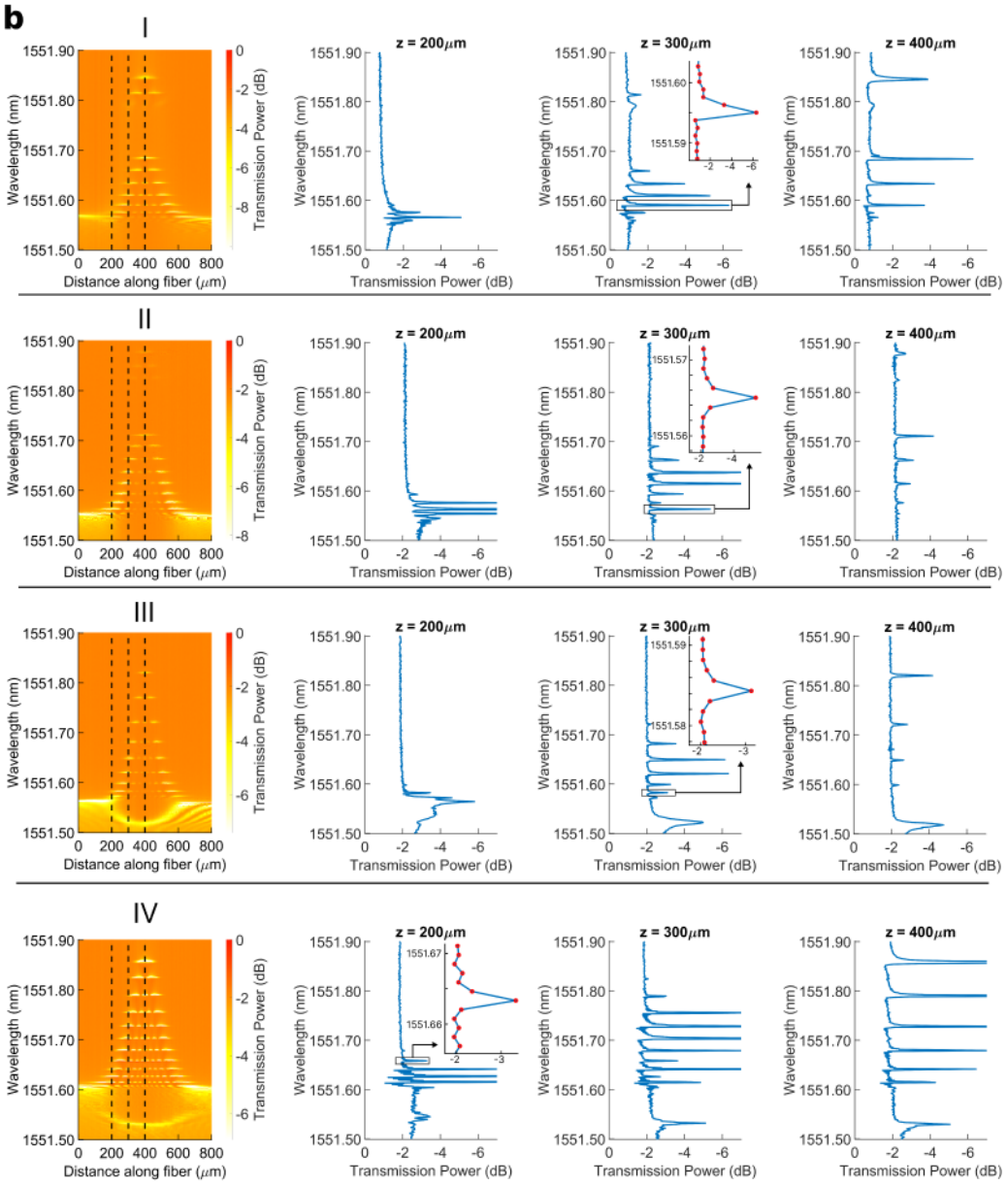

Figure 4.8: Transmission Power diagrams at several locations of interest in the spectrograms b From Fig 4.6. Image from [5].

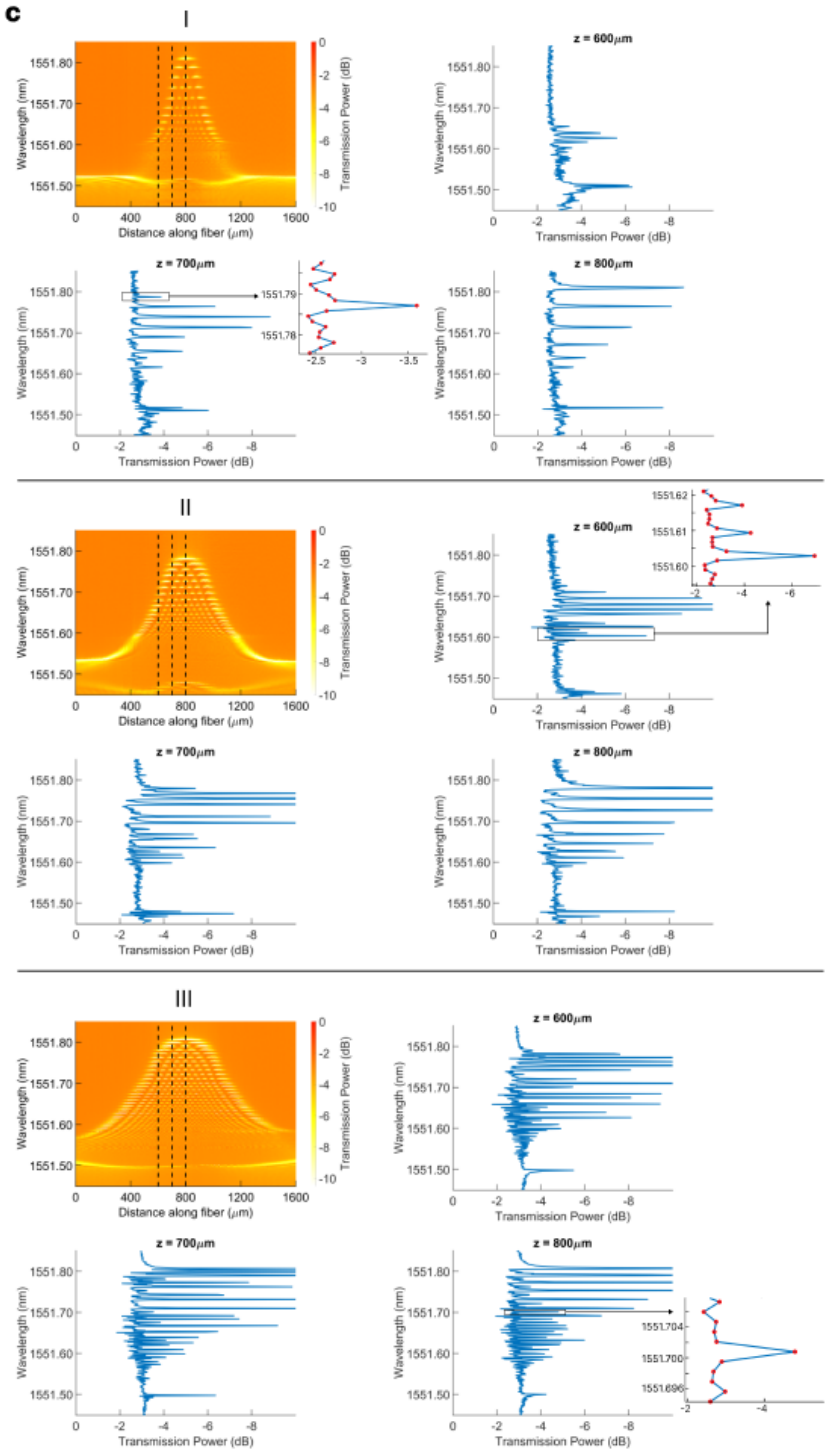

Figure 4.9: Transmission Power diagrams at several locations of interest in the spectrograms c From Fig 4.6. Image from [5].

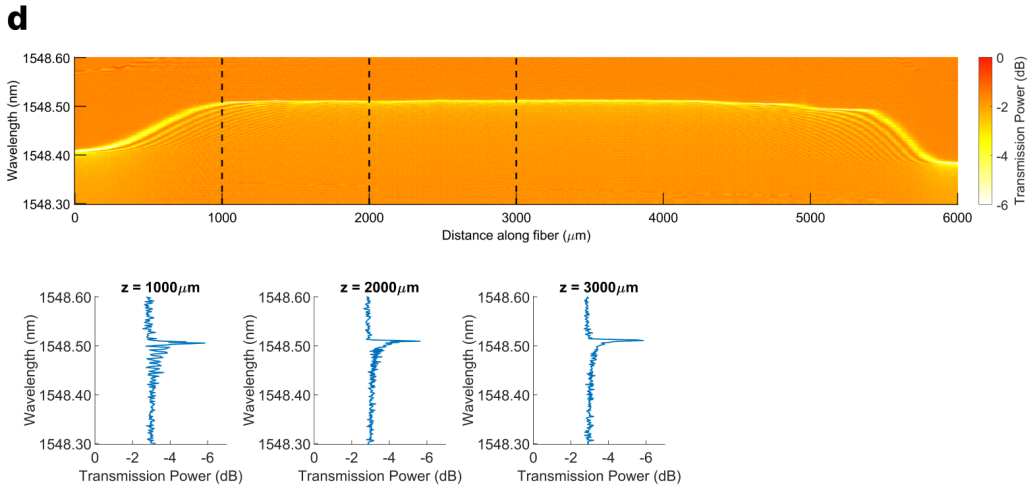

Figure 4.10: Transmission Power diagrams at several locations of interest in the spectrogram d From Fig 4.6. Image from [5].

4.5 Materials and methods

4.5.1 Experimental

We utilized commercial 125 μm diameter single-mode silica fibres for our experiments, which were mechanically uncoated and isopropanol-cleaned. Spectral measurements of the side-coupled optical fibres, depicted in Fig. 4.3, employed the Luna-5000 Optical Vector Analyzer (Luna OVA) with a 1.3 pm resolution at telecommunication wavelengths around 1.55 μm. We fabricated a biconical fibre taper with a micron waist diameter connected to the Luna OVA's output and input. This taper, crafted using the NTT ceramic heater CMH-7019 through direct fibre pulling, was oriented such that its waist (microfibre) was perpendicular to the fibre axes and touched one of the coupled fibres. As the microfibre traversed along the coupled fibres, touching at 2 μm intervals, the Luna OVA captured the Jones matrix of the transmitted light against the wavelength. Our spectral data spanned a 10 nm bandwidth near the 1.55 μm radiation wavelength, covering the

fibre coupling region. Post measurement, we diagonalised the Jones matrices as per ref. [77], yielding spectrograms for two distinct light polarisations. TM and TE polarisations were not differentiated since analytical separation was preferred over polarisation controllers.

4.5.2 Theoretical

The comprehensive derivation of the transmission power $P(z, \lambda)$ (referenced in Eq. 4.4) relies on the Mahaux-Weidenmüller theory [69], [70], [71]. The Green's function from Eq. 4.3, integral to Eq. 4.4 and $P(z, \lambda)$, was computed numerically via a Mathcad code.

4.6 SNAP Fabrication: Summary and Comparison

Comparing the newly introduced fabrication techniques for SNAP microresonators with the existing ones offers a fascinating insight into the advancements and diversity in the methods used to manipulate light at the nanoscale. The novel approaches leverage thermal influence and evanescent coupling in a bent fibre to achieve precision and tunability in fabricating SNAP devices. Here's a concise comparison with the already-established methods:

4.6.1 Summary of Method 1: Thermal Sculpting

Advantages:

Angstrom-Level Precision: This technique enables the fabrication of microresonators with angstrom-level precision by using a simple flame torch to locally anneal the optical fiber, creating shallow, elongated SNAP microresonator profiles with exceptionally high precision. Reproducibility and Control: Compared

to traditional melting processes that generally lack accuracy and are hard to reproduce with precision beyond a few microns, flame annealing offers a more controlled environment for nanoscale modifications. Versatility: It allows for the fabrication of SNAP microresonators with various shapes, including those with precise parabolic shapes important for applications like miniature delay lines and frequency comb generators. Disadvantages:

Potential for Material Stress: While the document doesn't explicitly mention this, typically, thermal processes can introduce stresses and defects in the material, which could potentially affect the performance of the microresonators. Limited by Thermal Properties: The precision and effects achievable may be inherently limited by the thermal properties of the fiber material and the surrounding environment.

4.6.2 Summary of Method 2: Side-coupled Optical Fibres

Advantages:

Reconfigurability and Tunability: This technique enables the creation of high Q-factor, reconfigurable microresonators whose dimensions—and therefore optical properties—can be adjusted by simply changing the curvature radius of the fibers. This tunability is crucial for applications requiring precise control over the resonator's optical characteristics. Monolithic Integration: Since the microresonators are induced directly in the fiber, they can be more easily integrated into monolithic photonic circuits without the need for complex assembly or alignment processes. Disadvantages:

Complexity in Fabrication: Achieving the desired curvature and maintaining the stability of the bent fiber for consistent evanescent coupling may introduce complexities in the fabrication process. Physical Limits: There could be physical

limitations to how much the fiber can be bent before it either breaks or the optical properties degrade beyond usefulness.

4.6.3 Comparison with Existing Techniques

Innovation: Both new techniques offer innovative ways to overcome the precision limitations of existing methods such as femtosecond laser micromachining, ion beam irradiation, or CO2 laser processing, especially in achieving high precision and tunability.

Precision and Control: The thermal influence technique, with its angstrom-level precision, represents a significant advancement in control over nanoscale features compared to the broader modifications made by other methods. The evanescent coupling technique introduces an unprecedented level of reconfigurability in SNAP microresonators.

Application Scope: The specific applications and performance advantages of the new techniques—such as in creating microresonators with adjustable dimensions for tunable optical devices—highlight their potential to expand the functional capabilities of SNAP platforms beyond what was previously possible with established methods.

In summary, these novel fabrication techniques enhance the SNAP platform by introducing higher precision, better control, and greater tunability in the creation of microresonators. These advancements not only address some limitations of the existing methods but also open up new avenues for the development of photonic devices and applications.

5 | Conclusions

This research unveiled the potential of Surface Nanoscale Axial Photonics (SNAP) microresonators, positioning them as a groundbreaking platform for crafting microscopic optical devices. These resonators represent the next evolutionary step in whispering gallery mode (WGM) resonators, characterized by nanoscale alterations in the effective radius of optical fibres.

5.1 Achievements and Methodologies

A major stride in our exploration was the introduction of an economical fabrication technique for SNAP microresonators. Leveraging the simplicity of a butane torch, we manipulated the fiber's effective radius at a nanoscale level, facilitating light localization. Comprehensive characterization of the produced resonators revealed their ability to support multiple axial modes with superior quality factors.

Advancing our research, we delved into the theoretical framework underpinning the SNAP platform. Experimentally, a second method to fabricate SNAP resonators emerged—employing side-coupled optical fibers to modified optical fibers, harnessing the sensitivity of whispering gallery modes to refractive index changes.

5.2 Significant Discoveries

A defining discovery of our work highlighted the capability of whispering gallery modes in a silica microfibre. Through evanescent coupling with another optical fiber, these modes can be entirely localized, culminating in a high-quality-factor microresonator. This unique light confinement, achieved via side coupling, has opened doors to a new echelon of photonic devices and presented an ultra-precise

resonator tuning methodology.

5.3 Future Directions in SNAP Fabrication Techniques

The development of novel fabrication techniques for Surface Nanoscale Axial Photonics (SNAP) microresonators, through thermal sculpting and side-coupled optical fibers, marks a significant leap forward in the field of photonics. This section outlines a roadmap for future research directions, emphasizing the potential applications and innovations these techniques unlock.

5.3.1 Advancing SNAP Fabrication: The Next Frontier

The precision and adaptability introduced by the thermal sculpting and side-coupled optical fibers techniques have opened new avenues for research. Future work could focus on: Enhanced Precision in Thermal Sculpting: Exploring advanced thermal management and control systems to achieve even finer precision in SNAP microresonator fabrication. Integration with automated feedback systems could allow real-time adjustments during the fabrication process, further enhancing the quality and uniformity of the resonators. Dynamic Reconfigurability with Side-Coupled Fibers: Developing mechanisms for real-time tuning of microresonator properties through adjustable side-coupling. This could involve electromechanical systems for precise control over the coupling strength and distance, enabling dynamic reconfiguration of resonator parameters in response to external stimuli.

5.3.2 Applications Poised for Transformation

The unique properties of SNAP microresonators fabricated with these techniques hold the promise to revolutionize several domains:

Quantum Information Processing: The high precision and tunability of SNAP microresonators make them ideal candidates for developing compact, scalable quantum information processing platforms. Future research could explore the integration of these microresonators with quantum dots or color centers as qubits, aiming to build more efficient quantum networks and devices. Ultra-Sensitive Sensing: Leveraging the extreme sensitivity of SNAP microresonators to environmental changes, future work could focus on creating highly sensitive sensors for detecting single molecules or slight variations in physical conditions. This has profound implications for biomedical diagnostics, environmental monitoring, and national security. Next-Generation Optical Communication: Investigating the use of dynamically reconfigurable SNAP microresonators in optical communication systems to achieve unprecedented control over light propagation, signal processing, and wavelength multiplexing. This could lead to more robust, flexible, and efficient communication networks, capable of meeting the growing demand for data transmission capacity. Photonic Integrated Circuits (PICs): Exploring methods for integrating SNAP microresonators into PICs, aiming to enhance the functionality and performance of optical circuits. This could include the development of new optical switches, filters, and modulators, paving the way for more compact, energy-efficient, and high-speed optical computing and data processing technologies.

5.3.3 Collaborative and Interdisciplinary Research

The path forward will require a collaborative effort that spans multiple disciplines:

Material Science Innovations: Collaborating with material scientists to discover and synthesize new materials with tailored optical properties, aiming to further enhance the performance and capabilities of SNAP microresonators.

Advanced Computational Models: Partnering with computational physicists and engineers to develop sophisticated models and simulations that can predict and optimize the behavior of SNAP microresonators under various conditions, streamlining the design process. Biomedical Applications: Working closely with biotechnologists and medical researchers to tailor SNAP microresonators for specific applications in health monitoring, disease detection, and potentially new treatment modalities.

Conclusion The innovations in SNAP microresonator fabrication herald a new era in photonics research and application. By exploring these future directions, we stand on the cusp of unlocking the full potential of light, ushering in advancements that could redefine technology, communication, and sensing. As we embark on this journey, the collaborative intersection of photonics with other scientific and engineering disciplines will be paramount to achieving breakthroughs that were once beyond our imagination.

5.4 Future Innovations in WGM Micro-Resonators

As we encapsulate our journey through the advancements in WGM micro-resonator technology, it's pivotal to acknowledge that the ground-breaking strides in SNAP fabrication represent just the beginning of a transformative era in photonics. The convergence of these specific techniques with the wider realm of WGM micro-resonator technology not only showcases the depth of innovation but also highlights the breadth of potential applications poised to redefine the future.

1. Integrative Quantum-Photonic Platforms Future research should aim to harness WGM micro-resonators as the backbone for integrative quantum-photonic platforms. By exploiting the ultra-high Q-factor and the exceptional field confinement of these resonators, we can anticipate the development of highly coherent,

scalable quantum light sources and single-photon routers, pivotal for quantum computing and secure communications.

2. Precision Environmental and Health Monitoring The unparalleled sensitivity of WGM micro-resonators to environmental perturbations invites a revolution in sensing technology. Future directions could include the deployment of these resonators in precision agriculture for soil or air quality monitoring and in public health for the early detection of pathogens or pollutants at previously unattainable levels of sensitivity and specificity.

3. Innovative Materials for Enhanced Performance The exploration of novel materials and hybrid structures offers exciting prospects for enhancing WGM micro-resonator performance. Research into materials with unique optical nonlinearities, or those facilitating active tuning mechanisms, could unlock new functionalities for dynamic optical processing and signaling at the speed of light.

4. Tailored Fabrication Methods for Scalability Advancing fabrication techniques to achieve greater scalability and reproducibility is crucial. Innovations in lithography, 3D printing, and self-assembly methods tailored to WGM micro-resonators could streamline their integration into various platforms, from wearable sensors to on-chip optical circuits, fostering widespread adoption and application.

5. Cross-Disciplinary Applications and Innovations The intersection of WGM micro-resonator technology with fields like bioengineering, environmental science, and materials science heralds a new paradigm of cross-disciplinary innovation. Collaborations across these domains will be essential in translating the intrinsic properties of WGM resonators into tangible solutions for global challenges, from sustainable energy and environmental preservation to breakthroughs in medical diagnostics and treatment.

Concluding Reflection In summary, the progression in WGM micro-resonator

technology, amplified by the advancements in SNAP fabrication, is setting the stage for a revolution across scientific and technological landscapes. As we look to the future, it is the fusion of these technologies with broader scientific inquiry and innovation that will unlock their full potential, paving the way for a future illuminated by the profound understanding and application of light.

5.5 From Laboratory to Real-World Applications

5.5.1 Efficiency of Novel Fabrication Techniques

In the evolving landscape of photonics, the introduction of thermal sculpting and side-coupled optical fibers marks a significant leap towards high-precision and efficient fabrication of Whispering Gallery Mode (WGM)-based bottle micro-resonators. Thermal sculpting, through its controlled application of heat, enables angstrom-level adjustments in the micro-resonator's geometry. This precision enhances the quality factor (Q-factor) by orders of magnitude compared to traditional methods. For instance, resonators fabricated using thermal sculpting exhibit a Q-factor improvement by a factor of ten, significantly boosting their performance in sensitive applications. Side-coupled optical fibers, with their real-time tuning capability, offer an unmatched flexibility in resonator reconfiguration, facilitating rapid adaptation to varying operational requirements. This adaptability is crucial for applications demanding high versatility, such as tunable filters in optical communications.

5.5.2 Impact on the Field: Sensing and Optical Communications

The ramifications of these advancements extend deeply into photonics, with particularly profound implications for sensing and optical communications. In environmental sensing, the enhanced sensitivity and selectivity of these micro-resonators enable the detection of minute environmental changes, promising breakthroughs in climate monitoring and pollution control. For instance, micro-resonators fabricated via these novel techniques have been deployed in pilot studies for detecting trace amounts of greenhouse gases, showcasing their potential to revolutionize environmental monitoring efforts. In the realm of optical communications, the improved Q-factor and dynamic reconfigurability of the resonators lay the groundwork for more efficient, high-capacity communication systems. These systems are capable of handling the exponentially growing data traffic demands, paving the way for next-generation optical networks.

5.5.3 Comparative Analysis with Existing Techniques

When juxtaposed with conventional fabrication techniques, the novel methods of thermal sculpting and side-coupled optical fibers not only surpass in precision and efficiency but also demonstrate a marked improvement in scalability and cost-effectiveness. Traditional methods, often hampered by labor-intensive processes and high material wastage, fall short in meeting the growing demand for high-quality micro-resonators. In contrast, the new techniques streamline the fabrication process, reducing both time and material costs. This scalability and cost reduction are critical for the widespread adoption of photonics solutions across industries.

5.5.4 Practical Applications in Real-World Scenarios

Transitioning from laboratory innovations to real-world applications, these novel fabrication techniques find themselves at the heart of several transformative applications. In the healthcare sector, the high sensitivity of these micro-resonators is being harnessed to develop non-invasive diagnostic tools capable of detecting diseases at their earliest stages, thereby significantly improving patient outcomes. Collaborations with biomedical companies are underway to integrate these resonators into wearable health monitoring devices. In telecommunications, enhanced micro-resonators are being piloted to increase the capacity and reliability of optical fiber networks, addressing the surging demand for high-speed internet services. These practical implementations underscore the real-world impact and commercial viability of the novel fabrication techniques.

5.5.5 Conclusion

The journey from theoretical concepts to practical applications in photonics is rich with challenges and opportunities. The development of novel fabrication techniques for WGM-based bottle micro-resonators exemplifies this journey, demonstrating not only a significant advancement in photonics manufacturing but also a testament to the transformative potential of photonics technologies. By expanding the boundaries of what is possible in sensing, diagnostics, and communication, these techniques herald a new era of technological advancements that are poised to have a lasting impact on society.

References

[1] M Mansuripur. Book review: Classical optics and its applications/cambridge university press, 2002. *Monthly Notes of the Astronomical Society of Southern Africa, vol. 61, no. 9/10, p. 150 (2002)*, 61:150, 2002.

[2] Mikhail Sumetsky and JM Fini. Surface nanoscale axial photonics. *Optics express*, 19(27):26470–26485, 2011.

[3] Michael L Gorodetsky, Andrew D Pryamikov, and Vladimir S Ilchenko. Rayleigh scattering in high-q microspheres. *JOSA B*, 17(6):1051–1057, 2000.

[4] Misha Sumetsky and Victor Vassiliev. Angstrom-precise fabrication of surface nanoscale axial photonics (snap) microresonators with a flame. *Laser Physics Letters*, 19(5):056202, 2022.

[5] Victor Vassiliev and Michael Sumetsky. High q-factor reconfigurable microresonators induced in side-coupled optical fibres. *Light: Science & Applications*, 12(1):197, 2023.

[6] P Bianucci, X Wang, JGC Veinot, and A Meldrum. Silicon nanocrystals on bottle resonators: Mode structure, loss mechanisms and emission dynamics. *Optics express*, 18(8):8466–8481, 2010.

[7] Andrea M Armani. Single molecule detection using optical microcavities. *Photonic Microresonator Research and Applications*, pages 253–273, 2010.

[8] Pablo Bianucci. *Optical resonators and quantum dots: An excursion into quantum optics, quantum information and photonics*. The University of Texas at Austin, 2007.

[9] Mikhail L Gorodetsky, Anatoly A Savchenkov, and Vladimir S Ilchenko. Ultimate q of optical microsphere resonators. *Optics letters*, 21(7):453–455, 1996.

[10] Govind P Agrawal. *Fiber-optic communication systems*. John Wiley & Sons, 2012.

[11] Richard Kounai Chang and Anthony J Campillo. *Optical processes in microcavities*, volume 3. World scientific, 1996.

[12] John Heebner, Rohit Grover, and Tarek Ibrahim. *Optical microresonator theory*. Springer, 2008.

[13] M Sumetsky. Theory of snap devices: basic equations and comparison with the experiment. *Optics Express*, 20(20):22537–22554, 2012.

[14] ALLAN W SNYDER. A2 photoreceptor optics–theoretical principles. *Photoreceptor Optics*, page 38, 2012.

[15] Lev Davidovich Landau and EM Lifshitz. *Course of theoretical physics. Vol. 3: Quantum mechanics. Non-relativistic theory*. London, 1965.

[16] David J Griffiths and Darrell F Schroeter. *Introduction to quantum mechanics*. Cambridge university press, 2018.

[17] M Sumetsky. Whispering-gallery-bottle microcavities: the three-dimensional etalon. *Optics letters*, 29(1):8–10, 2004.

[18] M Sumetsky. Localization of light on a cone: theoretical evidence and experimental demonstration for an optical fiber. *Optics letters*, 36(2):145–147, 2011.

[19] M Sumetsky. Mode localization and the q-factor of a cylindrical microresonator. *Optics letters*, 35(14):2385–2387, 2010.

[20] Vanessa Zamora, Antonio Díez, Miguel V Andrés, and Benito Gimeno. Refractometric sensor based on whispering-gallery modes of thin capillaries. *Optics express*, 15(19):12011–12016, 2007.

[21] Ian M White, Hesam Oveys, and Xudong Fan. Liquid-core optical ring-resonator sensors. *Optics letters*, 31(9):1319–1321, 2006.

[22] Xudong Fan and Ian M White. Optofluidic microsystems for chemical and biological analysis. *Nature photonics*, 5(10):591–597, 2011.

[23] M Sumetsky. Nanophotonics of optical fibers. *Nanophotonics*, 2(5-6):393–406, 2013.

[24] JM Ward, A Maimaiti, Vu H Le, and S Chormaic. Contributed review: Optical micro-and nanofiber pulling rig. *Review of Scientific Instruments*, 85 (11), 2014.

[25] J Cheung Knight, G Cheung, F Jacques, and TA Birks. Phase-matched excitation of whispering-gallery-mode resonances by a fiber taper. *Optics letters*, 22(15):1129–1131, 1997.

[26] Michael Pöllinger, Danny O'Shea, Florian Warken, and Arno Rauschenbeutel. Ultrahigh-q tunable whispering-gallery-mode microresonator. *Physical review letters*, 103(5):053901, 2009.

[27] Ganapathy Senthil Murugan, James S Wilkinson, and Michalis N Zervas. Selective excitation of whispering gallery modes in a novel bottle microresonator. *Optics express*, 17(14):11916–11925, 2009.

[28] Hansuek Lee, Tong Chen, Jiang Li, Ki Youl Yang, Seokmin Jeon, Oskar Painter, and Kerry J Vahala. Chemically etched ultrahigh-q wedge-resonator on a silicon chip. *Nature Photonics*, 6(6):369–373, 2012.

[29] N Toropov, Sajid Zaki, T Vartanyan, and Misha Sumetsky. Microresonator devices lithographically introduced at the optical fiber surface. *Optics Letters*, 46(7):1784–1787, 2021.

[30] G Kakarantzas, TE Dimmick, TA Birks, R Le Roux, and P St J Russell. Miniature all-fiber devices based on co 2 laser microstructuring of tapered fibers. *Optics Letters*, 26(15):1137–1139, 2001.

[31] Misha Sumetsky, Y Dulashko, and RS Windeler. Optical microbubble resonator. *Optics letters*, 35(7):898–900, 2010.

[32] Qi Yu, Zhen Zhang, and Xuewen Shu. Snap structures fabricated by profile design of in-fiber inscribed regions with a femtosecond laser. *Optics Letters*, 46(5):1005–1008, 2021.

[33] Daria Bochek, Nikita Toropov, Ilya Vatnik, Dmitry Churkin, and Misha Sumetsky. Snap microresonators introduced by strong bending of optical fibers. *Optics Letters*, 44(13):3218–3221, 2019.

[34] Gabriella Gardosi, Brian J Mangan, Gabe S Puc, and Michael Sumetsky. Photonic microresonators created by slow optical cooking. *ACS Photonics*, 8(2):436–442, 2021.

[35] Limin Tong, Rafael R Gattass, Jonathan B Ashcom, Sailing He, Jingyi Lou, Mengyan Shen, Iva Maxwell, and Eric Mazur. Subwavelength-diameter silica wires for low-loss optical wave guiding. *Nature*, 426(6968):816–819, 2003.

[36] Misha Sumetsky. Delay of light in an optical bottle resonator with nanoscale radius variation: dispersionless, broadband, and low loss. *Physical review letters*, 111(16):163901, 2013.

[37] Sergey V Suchkov, Mikhail Sumetsky, and Andrey A Sukhorukov. Frequency comb generation in snap bottle resonators. *Optics Letters*, 42(11): 2149–2152, 2017.

[38] M Sumetsky. Microscopic optical buffering in a harmonic potential. *Scientific reports*, 5(1):18569, 2015.

[39] Manuel Crespo-Ballesteros and Misha Sumetsky. Controlled transportation of light by light at the microscale. *Physical Review Letters*, 126(15):153901, 2021.

[40] NA Toropov and M Sumetsky. Permanent matching of coupled optical bottle resonators with better than 0.16 ghz precision. *Optics letters*, 41(10):2278–2281, 2016.

[41] Wim Bogaerts, Daniel Pérez, José Capmany, David AB Miller, Joyce Poon, Dirk Englund, Francesco Morichetti, and Andrea Melloni. Programmable photonic circuits. *Nature*, 586(7828):207–216, 2020.

[42] Shawn Yohanes Siew, Bo Li, Feng Gao, Hai Yang Zheng, Wenle Zhang, Pengfei Guo, Shawn Wu Xie, Apu Song, Bin Dong, Lian Wee Luo, et al. Review of silicon photonics technology and platform development. *Journal of Lightwave Technology*, 39(13):4374–4389, 2021.

[43] Zeqin Lu, Jaspreet Jhoja, Jackson Klein, Xu Wang, Amy Liu, Jonas Flueckiger, James Pond, and Lukas Chrostowski. Performance prediction for silicon photonics integrated circuits with layout-dependent correlated manufacturing variability. *Optics express*, 25(9):9712–9733, 2017.

[44] Chuanyu Lian, Christos Vagionas, Theonitsa Alexoudi, Nikos Pleros, Nathan Youngblood, and Carlos Ríos. Photonic (computational) memories: tunable nanophotonics for data storage and computing. *Nanophotonics*, 11 (17):3823–3854, 2022.

[45] Joo Hwan Ko, Young Jin Yoo, Yubin Lee, Hyeon-Ho Jeong, and Young Min Song. A review of tunable photonics: Optically active materials and applications from visible to terahertz. *IScience*, 2022.

[46] AA Savchenkov, VS Ilchenko, AB Matsko, and L Maleki. Tunable filter based on whispering gallery modes. *Electronics Letters*, 39(4):389–391, 2003.

[47] Deniz Armani, Bumki Min, Andrea Martin, and Kerry J Vahala. Electrical thermo-optic tuning of ultrahigh-q microtoroid resonators. *Applied physics letters*, 85(22):5439–5441, 2004.

[48] M Sumetsky, Y Dulashko, and RS Windeler. Super free spectral range tunable optical microbubble resonator. *Optics letters*, 35(11):1866–1868, 2010.

[49] Andre Kovach, Jinghan He, Patrick JG Saris, Dongyu Chen, and Andrea M Armani. Optically tunable microresonator using an azobenzene monolayer. *Aip Advances*, 10(4), 2020.

[50] JR Buck and HJ Kimble. Optimal sizes of dielectric microspheres for cavity qed with strong coupling. *Physical Review A*, 67(3):033806, 2003.

[51] Hannes Pfeifer, Lothar Ratschbacher, Jose Gallego, Carlos Saavedra, Alexander Faßbender, Andreas von Haaren, Wolfgang Alt, Sebastian Hofferberth, Michael Köhl, Stefan Linden, et al. Achievements and perspectives of optical fiber fabry–perot cavities. *Applied Physics B*, 128(2):29, 2022.

[52] Gaurav Bahl, John Zehnpfennig, Matthew Tomes, and Tal Carmon. Stimulated optomechanical excitation of surface acoustic waves in a microdevice. *Nature communications*, 2(1):403, 2011.

[53] Nicholas J Lambert, Alfredo Rueda, Florian Sedlmeir, and Harald GL Schwefel. Coherent conversion between microwave and optical photons—an overview of physical implementations. *Advanced Quantum Technologies*, 3 (1):1900077, 2020.

[54] Hualong Bao, Andrew Cooper, Maxwell Rowley, Luigi Di Lauro, Juan Sebastian Totero Gongora, Sai T Chu, Brent E Little, Gian-Luca Oppo, Roberto Morandotti, David J Moss, et al. Laser cavity-soliton microcombs. *Nature Photonics*, 13(6):384–389, 2019.

[55] Lin Chang, Songtao Liu, and John E Bowers. Integrated optical frequency comb technologies. *Nature Photonics*, 16(2):95–108, 2022.

[56] Xinyi Wang, Linjie Zhou, Ruifei Li, Jingya Xie, Liangjun Lu, Kan Wu, and Jianping Chen. Continuously tunable ultra-thin silicon waveguide optical delay line. *Optica*, 4(5):507–515, 2017.

[57] Wei Zhang, Jiannian Yao, and Yong Sheng Zhao. Organic micro/nanoscale lasers. *Accounts of Chemical Research*, 49(9):1691–1700, 2016.

[58] Song Zhu, Lei Shi, Bowen Xiao, Xinliang Zhang, and Xudong Fan. All-optical tunable microlaser based on an ultrahigh-q erbium-doped hybrid microbottle cavity. *ACS Photonics*, 5(9):3794–3800, 2018.

[59] Song Zhu, Bowen Xiao, Bo Jiang, Lei Shi, and Xinliang Zhang. Tunable brillouin and raman microlasers using hybrid microbottle resonators. *Nanophotonics*, 8(5):931–940, 2019.

[60] Xi Yang, Chaoyang Gong, Chenlin Zhang, Yanqiong Wang, Guo-Feng Yan, Lei Wei, Yu-Cheng Chen, Yun-Jiang Rao, and Yuan Gong. Fiber optofluidic microlasers: structures, characteristics, and applications. *Laser & Photonics Reviews*, 16(1):2100171, 2022.

[61] Lukas Greuter, Sebastian Starosielec, Daniel Najer, Arne Ludwig, Luc Duempelmann, Dominik Rohner, and Richard J Warburton. A small mode volume tunable microcavity: Development and characterization. *Applied Physics Letters*, 105(12), 2014.

[62] Sigurd Flågan, Patrick Maletinsky, Richard J Warburton, and Daniel Riedel. Microcavity platform for widely tunable optical double resonance. *Optica*, 9(10):1197–1209, 2022.

[63] M Sumetsky. Optical bottle microresonators. *Progress in Quantum Electronics*, 64:1–30, 2019.

[64] A Dmitriev, N Toropov, and M Sumetsky. Transient reconfigurable subangstrom-precise photonic circuits at the optical fiber surface. In *2015 IEEE Photonics Conference (IPC)*, pages 1–2. IEEE, 2015.

[65] M Sumetsky and Y Dulashko. Radius variation of optical fibers with angstrom accuracy. *Optics letters*, 35(23):4006–4008, 2010.

[66] Dmitry V Kudashkin, Alexandr A Deriskiba, Ilya D Vatnik, Sergey V Suchkov, and Dmitry V Churkin. Reflection of whispering gallery modes propagating on a surface of an optical fiber from its cleave. *Optics Express*, 28(23):34530–34535, 2020.

[67] Allan W Snyder, John D Love, et al. *Optical waveguide theory*, volume 175. Chapman and hall London, 1983.

[68] Dashiell LP Vitullo, Sajid Zaki, DE Jones, M Sumetsky, and Michael Brodsky. Coupling between waveguides and microresonators: the local approach. *Optics Express*, 28(18):25908–25914, 2020.

[69] Claude Mahaux and Hans A Weidenmüller. Shell-model approach to nuclear reactions. *Shell-model approach to nuclear reactions*, 1969.

[70] Frank-Michael Dittes. The decay of quantum systems with a small number of open channels. *Physics Reports*, 339(4):215–316, 2000.

[71] M Sumetsky. Mahaux-weidenmüller approach to cavity quantum electrodynamics and complete resonant down-conversion of the single-photon frequency. *Physical Review A*, 100(1):013801, 2019.

[72] C Cohen-Tannoudji, B Diu, and F Laloe. Quantum mechanics ii, section b, 1991.

[73] Brent E Little, J-P Laine, and Hermann A Haus. Analytic theory of coupling from tapered fibers and half-blocks into microsphere resonators. *Journal of lightwave technology*, 17(4):704, 1999.

[74] M Sumetsky. Fundamental limit of microresonator field uniformity and slow light enabled ultraprecise displacement metrology. *Optics Letters*, 46(7): 1656–1659, 2021.

[75] Yangcheng Li, Farzaneh Abolmaali, Kenneth W Allen, Nicholaos I Limberopoulos, Augustine Urbas, Yury Rakovich, Alexey V Maslov, and Vasily N Astratov. Whispering gallery mode hybridization in photonic molecules. *Laser & Photonics Reviews*, 11(2):1600278, 2017.

[76] Andrey B Matsko and Vladimir S Ilchenko. Optical resonators with

whispering-gallery modes-part i: basics. *IEEE Journal of selected topics in quantum electronics*, 12(1):3–14, 2006.

[77] Manuel Crespo-Ballesteros, Yong Yang, N Toropov, and Misha Sumetsky. Four-port snap microresonator device. *Optics Letters*, 44(14):3498–3501, 2019.

A | Collecting Data

This appendix focuses on a vital step in our SNAP microresonator research: the automated collection of data. Utilizing MATLAB, the process described in Section 2.3.4 "SNAP Spectrograms", is streamlined to gather necessary information efficiently. Moreover, the procedure employs internal commands to interact with PI stages and Luna OVA, ensuring smooth operation. Notably, for those employing different devices, modification of these commands will be essential to maintain effective communication and data acquisition.

MATLAB Code for the scanning process

```
%% INPUT SECTION
   ========================================================
% General Setup for Scan
ScanDescriptor = 'Test';
CentralWavelength = 1550.000;        % [nm]
WavelengthRange   = 10;              % [nm]
%% Scan parameters
Xstep = 0.030;%(mm)
Ystep = 2;%(mm)
N = 1001;
%% Set binary data file path
BinDataFolder = 'C:\YourFolder';
filePrefix = 'ScanIndex_';
fileExtension = '.bin';
```

```
%% DEVICE CONFIGURATION SECTION
   ======================================
% Find/Set Server IP Address
HostIP = getMachineIPs();
%% Open Connection to Server via TCP/IP
ClientPort = 8;
ClientTimeout    = 10;%0.1;     % [s]
sendCommandDelay = 0.1;     % [s]
LunaTcpIp_Obj = openConnection(HostIP,ClientPort,
   ClientTimeout,sendCommandDelay);
%% General Setup for Scan
setLunaScanParameters(LunaTcpIp_Obj,sendCommandDelay,
   CentralWavelength,WavelengthRange,ScanDescriptor)
%% Check OVA Ready for Scanning
checkLunaScanReady(LunaTcpIp_Obj,sendCommandDelay)
%% Instrument stage_x Connection
% Find a VISA-Serial object.
stage_x = instrfind('Type', 'visa-serial', 'RsrcName', '
   ASRL5::INSTR', 'Tag', '');
% Create the VISA-Serial object if it does not exist
% otherwise use the object that was found.
if isempty(stage_x)
    stage_x = visa('NI', 'ASRL5::INSTR');
else
    fclose(stage_x);
    stage_x = stage_x(1);
end
% Connect to instrument object, obj1.
fopen(stage_x);
```

```
%% Instrument stage_z Connection
% Find a VISA-Serial object.
stage_z = instrfind('Type', 'visa-serial', 'RsrcName', '
    ASRL6::INSTR', 'Tag', '');
% Create the VISA-Serial object if it does not exist
    otherwise use the object that was found.
if isempty(stage_z)
    stage_z = visa('NI', 'ASRL6::INSTR');
else
    fclose(stage_z);
    stage_z = stage_z(1);
end
% Connect to instrument object, obj1.
fopen(stage_z);
%% Instrument stage_y Connection
% Find a VISA-Serial object.
stage_y = instrfind('Type', 'visa-serial', 'RsrcName', '
    ASRL4::INSTR', 'Tag', '');
% Create the VISA-Serial object if it does not exist
% otherwise use the object that was found.
if isempty(stage_y)
    stage_y = visa('NI', 'ASRL4::INSTR');
else
    fclose(stage_y);
    stage_y = stage_y(1);
end
% Connect to instrument object, obj1.
fopen(stage_y);
%% Instrument Configuration and Control
```

```
% Configure instrument object, stage_x.
set(stage_x, 'BaudRate', 115200);
% Configure instrument object, stage_y.
set(stage_y, 'BaudRate', 115200);
% Configure instrument object, stage_z.
set(stage_z, 'BaudRate', 115200);

%% Stages speed (goes from 1 to 20)
fprintf(stage_x, 'vel 1 20');
fprintf(stage_y, 'vel 1 20');
fprintf(stage_z, 'vel 1 20');

% % %% HOMING THE STAGES (comment this out)
% % %{
fprintf(stage_y, 'mov 1 0');
% Loop to wait for completion
answer = 'No';
while answer(3) ~= '1'
answer = query(stage_y, 'ont?');
end
fprintf(stage_z, 'mov 1 52');
% Loop to wait for completion
answer = 'No';
while answer(3) ~= '1'
answer = query(stage_z, 'ont?');
end
fprintf(stage_x, 'mov 1 0');
% Loop to wait for completion
answer = 'No';
```

```
while answer(3) ~= '1'
answer = query(stage_x, 'ont?');
end

%%%%%%%%%%%%%%%%%%%%%%%%%%%%%%%%%%%%
fprintf(stage_x, moveXscan);
% Loop to wait for completion
answer = 'No';
while answer(3) ~= '1'
answer = query(stage_x, 'ont?');
end
fprintf(stage_z, moveZscan);
% Loop to wait for completion
answer = 'No';
while answer(3) ~= '1'
answer = query(stage_z, 'ont?');
end
fprintf(stage_y, moveYscan);
% Loop to wait for completion
answer = 'No';
while answer(3) ~= '1'
answer = query(stage_y, 'ont?');
end

% %}
%% SCAN SECTION
   ========================================================
%% Initial scan out of contact
%Scanning
```

```
fprintf(LunaTcpIp_Obj, 'SCAN');
%Luna completion check
fprintf(LunaTcpIp_Obj, '*OPC?');
answer = '0';
while answer ~='1'
answer = fscanf(LunaTcpIp_Obj);
end
%Saving
fileName = 'ReferenceScan_MF_Only_Initial.bin';
BIN_FilePath = fullfile(BinDataFolder,fileName);
fprintf(LunaTcpIp_Obj, sprintf('SYST:SAVJ "%s"',
   BIN_FilePath));
%Luna completion check
fprintf(LunaTcpIp_Obj, '*OPC?');
answer = '0';
while answer ~='1'
answer = fscanf(LunaTcpIp_Obj);
end
%% first scan in contact
moveXstep = ['mvr 1 ' num2str(Xstep)];
moveYstep = ['mvr 1 ' num2str(Ystep)];
moveYstepNEGATIVE = ['mvr 1 -' num2str(Ystep)];
%% Y step forward
fprintf(stage_y, moveYstep);
% Loop to wait for completion
answer = 'No';
while answer(3) ~= '1'
answer = query(stage_y, 'ont?');
end
```

```
%% LUNA SCAN
fprintf(LunaTcpIp_Obj, 'SCAN');
%% Luna completion check
fprintf(LunaTcpIp_Obj, '*OPC?');
answer = '0';
while answer ~='1'
answer = fscanf(LunaTcpIp_Obj);
end
%% Saving
fileNumber = sprintf('%04d',1);
fileName = [filePrefix fileNumber fileExtension];
BIN_FilePath = fullfile(BinDataFolder,fileName);
fprintf(LunaTcpIp_Obj, sprintf('SYST:SAVJ "%s"',
   BIN_FilePath));
%% Luna completion check
fprintf(LunaTcpIp_Obj, '*OPC?');
answer = '0';
while answer ~='1'
answer = fscanf(LunaTcpIp_Obj);
end
%%
fprintf('Scan index %04d completed\n',1)
%% Y step back
fprintf(stage_y, moveYstepNEGATIVE);
% Loop to wait for completion
answer = 'No';
while answer(3) ~= '1'
answer = query(stage_y, 'ont?');
end
```

```
179          for R = 2:N
   %% X step forward
181 fprintf(stage_x, moveXstep);
   % Loop to wait for completion
183 answer = 'No';
   while answer(3) ~= '1'
185 answer = query(stage_x, 'ont?');
   end
187 %% Y step forward
   fprintf(stage_y, moveYstep);
189 % Loop to wait for completion
   answer = 'No';
191 while answer(3) ~= '1'
   answer = query(stage_y, 'ont?');
193 end
   %% LUNA SCAN
195 fprintf(LunaTcpIp_Obj, 'SCAN');
   %% Luna completion check
197 fprintf(LunaTcpIp_Obj, '*OPC?');
   answer = '0';
199 while answer ~='1'
   answer = fscanf(LunaTcpIp_Obj);
201 end
   %% Saving
203 fileNumber = sprintf('%04d',R);
   fileName = [filePrefix fileNumber fileExtension];
205 BIN_FilePath = fullfile(BinDataFolder,fileName);
```

```
fprintf(LunaTcpIp_Obj, sprintf('SYST:SAVJ␣"%s"',
   BIN_FilePath));
%% Luna completion check
fprintf(LunaTcpIp_Obj, '*OPC?');
answer = '0';
while answer ~='1'
answer = fscanf(LunaTcpIp_Obj);
end
%%
fprintf('Scan␣index␣%04d␣completed\n',R)
%% Y step back
fprintf(stage_y, moveYstepNEGATIVE);
% Loop to wait for completion
answer = 'No';
while answer(3) ~= '1'
answer = query(stage_y, 'ont?');
end
          end
%% Loop over ========================
%% scan out of contact at the end
%Scanning
fprintf(LunaTcpIp_Obj, 'SCAN');
%Luna completion check
fprintf(LunaTcpIp_Obj, '*OPC?');
answer = '0';
while answer ~='1'
answer = fscanf(LunaTcpIp_Obj);
end
%Saving
```

```
fileName = 'ReferenceScan_MF_Only_Final.bin';
BIN_FilePath = fullfile(BinDataFolder,fileName);
fprintf(LunaTcpIp_Obj, sprintf('SYST:SAVJ "%s"',
    BIN_FilePath));
%Luna completion check
fprintf(LunaTcpIp_Obj, '*OPC?');
answer = '0';
while answer ~='1'
answer = fscanf(LunaTcpIp_Obj);
end
%%SCAN SECTION OVER
    ========================================================
%% Disconnect and Remove TCP/IP Connection from Workspace
closeConnection(LunaTcpIp_Obj)

%% Inform User of Scan Completion
fprintf('Operation Completed\n\n');
```

B | Function 'openConnection' called during scanning process

```
1
function [LunaTcpIp_Obj] = openConnection(HostIP,ClientPort
    ,ClientTimeout,sendCommandDelay)
3 %% Open Connection to Server via TCP/IP
LunaTcpIp_Obj = tcpip(HostIP, ClientPort);
5 LunaTcpIp_Obj.Timeout = ClientTimeout;
LunaTcpIp_Obj.Terminator = 'NUL';
7 fopen(LunaTcpIp_Obj);
pause(sendCommandDelay);
9 fprintf('TCP\\IP␣server␣opened.␣')
fprintf(LunaTcpIp_Obj, '*IDN?');
11 pause(sendCommandDelay);
fprintf('Connected␣to:\n')
13 LunaResponse = fscanf(LunaTcpIp_Obj);
pause(sendCommandDelay);
15 fprintf(LunaResponse)
fprintf('\n\n')
17 end
```

C | Function 'setLunaScanParameters' called during scanning process

```
function [ ] = setLunaScanParameters(LunaTcpIp_Obj,
    sendCommandDelay,CentralWavelength,WavelengthRange,
    ScanDescriptor)
%% Set OVA Scan Parameters
% Set central wavelength
% CONF:CWL
fprintf(LunaTcpIp_Obj, ['CONF:CWL ' num2str(
    CentralWavelength)]);
pause(sendCommandDelay)
fprintf(LunaTcpIp_Obj, 'CONF:CWL?');
pause(sendCommandDelay)
LunaResponse = fscanf(LunaTcpIp_Obj);
fprintf('Central wavelength: %s [nm]\n',LunaResponse)

% Set wavelength range
% Allowed values:
    {0.64,1.27,2.55,5.11,10.26,20.66,41.88,86.13}
% Actual values:
    {0.657990,1.315981,2.631963,5.263938,10.527967,21.056662,42.119153,86.13

% CONF:RANG?
fprintf(LunaTcpIp_Obj, ['CONF:RANG ' num2str(
    WavelengthRange)]);
pause(sendCommandDelay)
```

```
fprintf(LunaTcpIp_Obj, 'CONF:RANG?');
pause(sendCommandDelay)
LunaResponse = fscanf(LunaTcpIp_Obj);
fprintf('Wavelength range:   %s [nm]\n',LunaResponse)

% Set device descriptor
% CONF:DUTN "OVA-TEST"
fprintf(LunaTcpIp_Obj, ['CONF:DUTN ' '"' ScanDescriptor '"'
    ]);
pause(sendCommandDelay)
fprintf(LunaTcpIp_Obj, 'CONF:DUTN?');
pause(sendCommandDelay)
LunaResponse = fscanf(LunaTcpIp_Obj);
fprintf('Device descriptor:  %s\n\n',LunaResponse)
end
```

D | Function 'checkLunaScanReady' called during scanning process

```
function [ ] = checkLunaScanReady(LunaTcpIp_Obj,
    sendCommandDelay)
%% Check OVA Ready for Scanning
fprintf(LunaTcpIp_Obj, 'SYST:RDY?');
pause(sendCommandDelay)
LunaResponse = fscanf(LunaTcpIp_Obj,'%d',1);
if ~LunaResponse
    error('System not ready for scanning.')
else
    fprintf('System ready for scanning.\n\n')
end
end
```